STUDY OF PLASTIC DEFORMATION OF NON-COHESIVE SOILS

Marcin Bujko

STUDY OF PLASTIC DEFORMATION OF NON-COHESIVE SOILS

Wydawnictwo
Uniwersytetu Warmińsko-Mazurskiego
w Olsztynie

Editorial Staff UWM
Editor-in-Chief
Wiesława Lizińska
Science Section Editor
Marek Mróz

Reviewer
Lech Bałachowski

Executive Editor
Mariola Jezierska

Cover Design
Dariusz Walasek

Typesetting and Text Composition
Marzanna Modzelewska

ISBN 978-83-8100-407-7

Wydawnictwo UWM
ul. Jana Heweliusza 14, 10-718 Olsztyn
tel. 89 523-36-61, fax 89 523-34-38
www.uwm.edu.pl/wydawnictwo/
e-mail: wydawca@uwm.edu.pl

Ark. wyd. 10,0 ; ark. druk. 8,5
Druk: Zakład Poligraficzny UWM w Olsztynie, zam. 613

Contents

List of symbols
(in order of appearance)

G	– shear modulus
E	– deformation modulus, elasticity modulus
τ_f	– tangential stress component
γ	– shear strain
G_{max}, G_0	– maximum, initial shear modulus
G_{dyn}	– dynamic shear modulus
ρ	– bulk density
V_s	– shear wave propagation velocit
ν	– Poisson's ration
ε_s	– shear strain
ε_v	– vertical component of strain
ε_h	– horizontal component of strain
e	– void ratio
M_{dyn}	– dynamic deformation modulus
M_{stat}	– static deformation modulus
M_{oedo}	– oedometer constrained deformation modulus
M_{max}	– maximum deformation modulus
γ_{PS}	– hardening parameter related to plastic strain
q	– deviatoric stress
q_f	– ultimate deviatoric stress
q_a	– asymptotic deviatoric stress
E_{ur}	– unloading-reloading deformation modulus
E_{50}	– secant deformation modulus at 50% of the ultimate deviatoric stress
c	– cohesion
Φ	– angle of internal friction
p_c	– preconsolidation pressure
K_0^{NC}	– at-rest earth pressure coefficient for normally consolidated soils
p'	– mean effective stress
d	– sample diameter
h	– sample height
m	– sample mass
I_S	– compaction index
p	– confining pressure, cell pressure
D, D_{TS}	– damping coefficient
T	– torque
T_0	– amplitude

Θ – twist angle
f – frequency
r – reduced sample radius
H, h – sample height
I – moment of inertia; image feature intensity
ω – circular frequency
δ – phase shift angle
I_0 – mass moment of inertia
C – viscosity coefficient, viscous damping constant
K – elastic constant
G_S – specific gravity
e_{min} – mimimum void ratio
e_{max} – maximum void ratio
d_{10} – values of the particle diameter at 10% in the cumulative distribution
γ_{res} – shear strain in the residual phase
$\Delta\gamma_{noise,prox}$ – shear strain noise level of standard proximity sensors
$\Delta\gamma_{noise,hall}$ – shear strain noise level recorded by Hall sensors,
C_U – uniformity coefficient
Δd – displacement amplitude
h' – active height of the sample

Acknowledgements

This work would not have been possible without the invaluable support and guidance of Professor Piotr Srokosz. His support provided me with the opportunity to join his research team, where I discovered my passion for geotechnical laboratory work. I am deeply grateful for his mentorship and encouragement throughout this journey.

I extend my heartfelt appreciation to all my colleagues at the Faculty of Geoengineering, particularly Dr Ireneusz Dyka, for his invaluable advice and constructive criticism. His insights have greatly enriched this work, and I am truly thankful for his contributions.

I am also indebted to my parents for their steadfast belief in me. Their unwavering faith has been a constant source of inspiration and motivation. Additionally, I would like to express my deepest gratitude to my wife, Magdalena, for her boundless love, unwavering support, and infinite patience. Her presence has been my greatest strength, and I am immensely grateful for her unwavering support throughout this endeavor.

Together, their support and encouragement have played a pivotal role in shaping this work, and for that, I am eternally grateful.

Marcin Bujko

Chapter 1

Introduction

1.1. Motivation and aims of presented research

Safe and economical building design requires accurate assessment of the soil-structure interaction. Knowledge of the mechanical features of soil is fundamental for proper modelling structure behavior at various stages of loading. Over the last decades, application of advanced research techniques brought noticeable progress in the field of research on the actual mechanical characteristics of soils, especially those describing soil stiffness and deformation.

Stiffness is a main soil property and characterizes the resistance of the soil material during the change of its form. Understanding the importance of the main features characterizing the stiffness of the soil and taking into account its non-linearity have extremely significant impact on structure's displacement analysis.

Atkinson emphasizes (Atkinson 2000) on a basis on Burland's works (Burland, Cole 1972, Burland 1979) that one of the major problems in geotechnical engineering of previous decades was noticeable difference between soil stiffness determined in the laboratory and retrospectively calculated from the observation of displacements. These differences could be eliminated by taking into account non-linearity of soil stiffness. Similar observations reported Jardine (Jardine et al. 1984).

Fahey has analyzed similar problem (Fahey 1998) and focused on the analysis of deformation parameters of geotechnical structures. He emphasizes that the estimation of soil deformation subjected to foundation load in common engineering practice is characterized by low accuracy, and the main reason for this is the failure to take into account the non-linear stress--strain characteristics in actual range of deformations occurring in the soil.

The importance of applying the principles of non-linear soil stiffness in engineering practice has been also mentioned by Benz (2007). In his doctoral thesis, Benz takes into account the non-linear stress-strain characteristic and describes the occurrence of permanent shear strain during the degradation of the subsoil stiffness. Benz points out that the maximum deformation at which the soil exhibits a fully reversible behavior is a relatively small value $\gamma<1\cdot10^{-6}$. He claims the soil stiffness in this range is a fundamental feature of all geotechnical materials such as clays, silts, sands, gravels and rocks, subjected to both static and dynamic loading, for drained and undrained conditions.

In this work, according to author’s own research and analyses, author studies non-linear features of soil stiffness and reports that soil material subjected to small loads inducing small strain, experiences permanent, plastic deformation that can be observed in torsional shear tests carried out in the RC/TS apparatus.

This work is the result observations made in geotechnical laboratory in Olsztyn and is an attempt to present the reader with evidence of elasto-plastic phenomena occurring in soils in the range of small strain. Author hopes this work will provide the reader with a new perspective on this fascinating field of research.

The foundation of this publication stands the doctoral thesis, which author defended in 2021 in Bialystok University of Technology under a supervision of Professor Piotr E. Srokosz. This has been extended and supplemented with a new content resulting from the author’s new observations in the field of research on soil stiffness.

1.2. Outline

This work presents author’s methods for identifying elastoplastic deformation of the soil in the range of small strain. According to the tests carried out, it was found that soil materials under certain load conditions do not behave in accordance with the theoretical models of Maxwell, Kelvin--Voigt or Burgers. Despite the deformation in the range small strain, soil material exhibits properties of visco-elastoplastic body.

The most important results of the work include:

– defining the limitations of the standard RC/TS test methodology;
– proposing a modified procedure for recording the results of a torsional shear test;
– proposing the modernization of the the RC/TS apparatus construction;
– proposing a procedure for torsional shear test using the optical flow method.

Subsequent chapters have been created to achieve the following objectives of the work:

- presentation of the current state-of-the-art in the field of research on$\gamma<1\cdot10^{-6}$.elastoplasticity in the range of small strain;
- development of methods and procedures for the detection of permanent, plastic deformation;
- demonstrating that developed methods have practical application.

The second and third chapter has been created to achieve the first objective of the work. These chapters outline the history of small strain research development and elastoplasticity. The chapters report on selected unconventional laboratory techniques for testing soil stiffness. The HS-Small constitutive model is also introduced.

The fourth chapter reports on the thesis of the work.

The fifth chapter reports on the possibilities and limitations of the standard methodology of torsional shear test carried out in the RC/TS apparatus. The main limitation of the standard RC/TS test methodology is the assumption that a soil material is subjected to viscoelastic deformation. This assumption is reflected, for example, in the interpretation of the damping coefficient in the torsional shear (TS) test, which is defined as the ratio of the energy dissipated by the material during cyclic torsion to the potential energy accumulated in the material during elastic deformation.

The sixth and seventh chapter has been created to achieve second and third objective of the work.

In the sixth chapter, the modification of the research method of torsional shear test on soil samples is proposed. Author has introduced several changes in the device design, maintaining the full, original functionality of the device and taking into account a serious simplification in the standard TS test methodology as well as the interpretation of the obtained results.

The seventh chapter contains the description of the the application of new sensors, extending the time of measurement and controlling the load paths. It allowed to confirm the research thesis, that soil materials subjected to small loads causing shear strain in the range of small strain, is subjected to permanent, plastic deformation that can be observed during the tests carried out in the modernized device.

The eighth chapter contains description of the application of the optical flow method during torsional shear tests. The results of the SIFT analysis show that only the part of the sample adjacent to the rotor of the apparatus might react to the torque. This means that the actual value of shear strain generated in the sample may be different from the value determined as standard by the device software. In addition, the use of a modified procedure for recording the results makes it possible to observe changes in visco-elastic strain of the material and to measure permanent strain after the process of torque loading is completed.

The methods of using the torsional shear apparatus proposed in the work allow to confirm the research thesis that soil material subjected to small loads inducing shear strain in the range of small strain, experiences permanent, plastic deformation that can be observed in torsional shear tests carried out in the RC/TS apparatus.

Chapter 2

Small strain stiffness experimental evidence

2.1. Shear modulus

The subject of the work is inextricably linked to the development of geotechnical research over the last decades in terms of such concepts as small strain stiffness and elastoplasticity in constitutive soil modeling.

Most of the works related to the subject of the non-linear nature of the soil are based on the assumption of non-linear degradation of the subsoil stiffness. In the last three decades, the basic parameter characterizing soil stiffness has become the shear modulus G (modulus of shear strain). This is partly due to the ambiguity of the definition of the deformation modulus E and the methods of determining its value. In geotechnical design and modeling, it is most often dealt with the compression of the soil half-space along with its distortion. The soil failure criterion is exceeding the limit value of the tangential stress component τ_f. The phenomena observed in the subsoil are fundamentally different from those occurring in typical construction materials, so for their description the shear modulus G is a more appropriate parameter than the elasticity modulus E.

In the general case, the shear modulus is defined by relationship resulting from Hooke's Law:

$$G = \frac{\tau_{ij}}{\gamma_{ij}} \text{ for } i \neq j \tag{2.1}$$

The shear modulus defined by equation (2.1) can be also determined directly from the elementary theory of torsion of circular cylinders (Timoshenko, Goodier 1962). This theory assumes that the resultant shear stress τ at any point in the cross-section is perpendicular to the radius r and proportional to its length l, as well as to the unit twist angle θ:

$$\tau = G \cdot \theta \cdot r \tag{2.2}$$

where: $\theta = \frac{\varphi}{l} = \frac{d\varphi}{dx}$, $\quad \tau = \frac{T}{I_0}$.

The polar moment of inertia of the cylindrical sample is defined by the following formula:

$$I_0 = \frac{\pi r^4}{2} = \frac{\pi d^4}{32} \tag{2.3}$$

For a homogeneous rod (see fig. 2.1), the torsional moment can be expressed as:

$$T = G I_0 \frac{\varphi}{l} \tag{2.4}$$

The maximum angle of twist of the cylindrical sample, denoted as φ:

$$\varphi = \frac{2Tl}{\pi G r^4} \tag{2.5}$$

and the sought shear modulus is:

$$G = \frac{2Tl}{\pi r^4 \varphi} \tag{2.6}$$

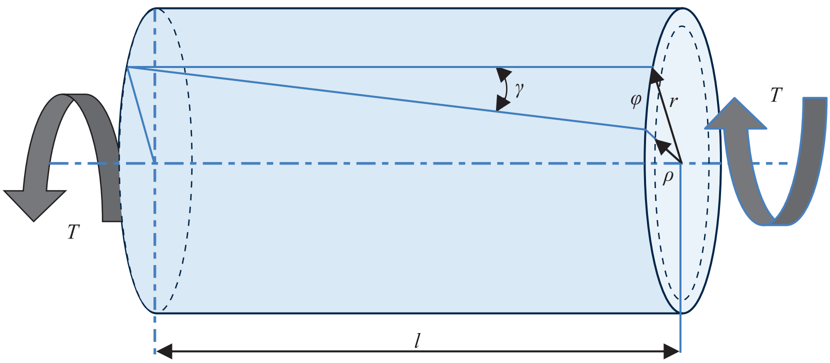

Fig. 2.1. Graphical interpretation of torsion in a homogeneous rod with a cylindrical cross-section

However, as previously stated, with the increase in stress and strain in the soil, there is a nonlinear change (degradation) in the value of the deformation modulus (Atkinson 2000).

The shear modulus expressed by equation (2.6) will therefore correspond to a certain state of deformation accompanying the resulting stress state. Thus, the value of G should be related to the shear stress τ and shear strain γ.

In the torsion model of a homogeneous cylindrical sample, the shear strain γ for a given state of deformation will depend on the position of the considered point in the sample, i.e., on the twist angle φ and the distance from the axis of the sample ρ, according to the relationship (for very small values of the twist angle φ):

$$\gamma = \frac{\varphi\rho}{l} \tag{2.7}$$

The shear modulus G defined in the above manner will be the secant modulus. Due to the ranges of considered strain in geotechnics, three main types of modules are distinguished (fig. 2.2): initial (G_{max}), secant (G_{s}), and tangent (G_{t}). It should also be added that factors influencing the module values include both the range of strain to which the module refers, as well as the stress state and its history (SROKOSZ et al. 2017).

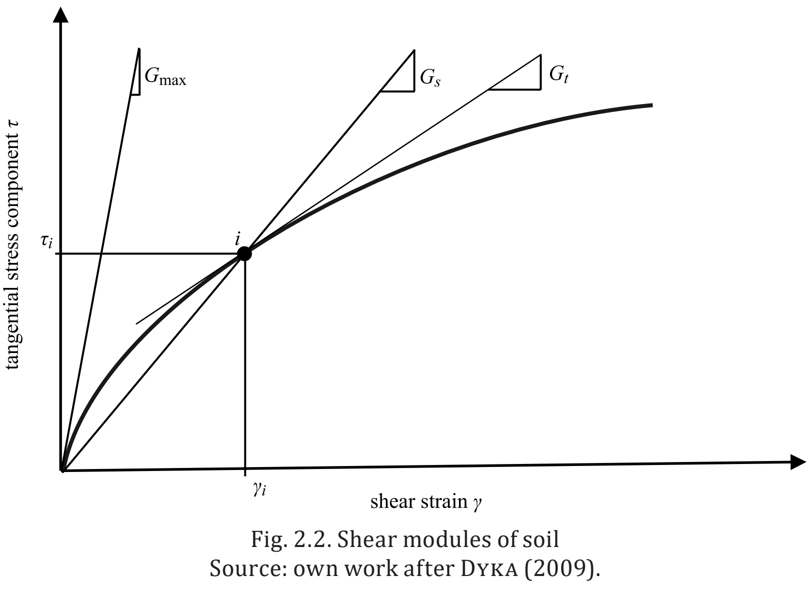

Fig. 2.2. Shear modules of soil
Source: own work after DYKA (2009).

The shear modulus G defined in the above manner is based on the assumption of isotropy of mechanical properties according to Hooke's law and the Coulomb-Mohr model. This model is commonly used to describe the stiffness of soil in the elastic range, i.e., before reaching the shear strength. One of the researchers contesting the use of such a defined shear modulus is Cudny. As Cudny stated (CUDNY 2013, CUDNY, PARTYKA 2015), modeling soil stiffness and simultaneously neglecting the influence of its anisotropy (resulting from the complexity of soil microstructure, its formation history, and loading history) can lead to discrepancies in replicating the observed behavior of soil in laboratory or in situ tests. In standard soil models, stiffness does not change with respect to stress level, the value of coefficient of earth pressure at rest, or when changing the orientation of stress axes in the adopted coordinate system. Additionally, the dependency of shear modules on stress level with a constant Poisson's ratio only affects the level of stiffness, but does not introduce changes in its directional distribution. Cudny suggests achieving elastic stiffness anisotropy induced by stress by using a hyperelastic model (Niemunis, Cudny 2000). The isotropic hyperelastic model allows for modeling the dependence of stiffness on stress level and the coefficient of static friction. Cudny highlights the justification for using Vermeer's hyperelastic model (Vermeer 1985) due to material parameters that can be easily related to standard constants in Hooke's law.

Soil stiffness degradation is most often described as a function of the relation between the current value of the G modulus and the value of the tangential stress component τ_f or shear strain γ (fig. 2.3). Experimentally obtained relations $G(\gamma)$ show a general tendency that the values of the modulus G decrease non-linearly with the increase in the value of shear strain γ. Out of the strain range $\gamma<1\cdot10^{-6}$, in which the section of the function $G(\gamma)$ is treated as constant ($G_{\max}$ level), the function monotonically decreases

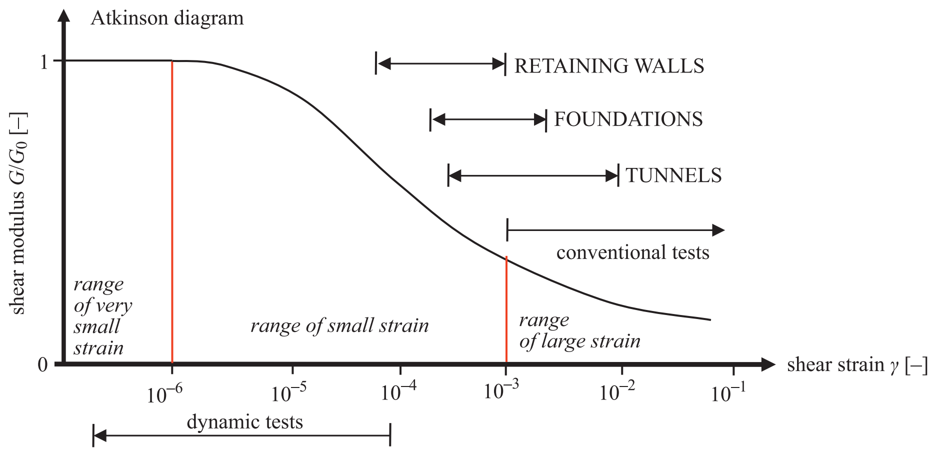

Fig. 2.3. Relation of the relative value of the shear modulus to the value of shear strain of soil. Characteristic ranges of shear strain according to Atkinson
Source: own work after Benz (2007).

with a significant, non-linear decrease in the value of G. This segment first described Hardin and Drnvevich as a hyperbolic function (Hardin, Drnevich 1972).

The soil stiffness decays non-linearly with the increase of shear strain value from $\gamma=1\cdot10^{-6}$. Conventional research methods for determining the mechanical properties of the soil using for example, a triaxial compression apparatus, enable testing in the range of large strain, i.e. from the value of $\gamma=1\cdot10^{-3}$. Thus, there is a noticeable gap in the strain range $\gamma=1\cdot10^{-6}\div1\cdot10^{-3}$, which is the range of high variability of the shear modulus. Atkinson (Atkinson et al. 1991) called it the range of small strain – the range impossible to register by conventional devices. In the same paper, Atkinson mentions that the non-linear dependence of soil stiffness on deformations in the range of small strain should be taken into account in all analyzes leading to a reliable forecast of displacements.

The legitimacy of the above statement is confirmed by the results presented in the works of e.g. Burland (1989), Mair (1993), Jardine and Symes (1995) and Tatsuoka, Shibuya and Kuwano (2001) and others (Fares et al. 2019, Lade 1977, Look 2007), in which the most common range of soil strain in the conditions of interaction with building structures is in the range $\gamma=1\cdot10^{-6}\div1\cdot10^{-2}$. This means that the scope of soil-structure interaction should be considered in the range of small strain. This statement also confirmed Wdowska and Wudzka (2006).

Since the formulation of the concept of small strain by Atkinson, the classification of strain in relation to the shear modulus has developed. Diaz-Rodrigez and Lopez-Molina in 2008 (Diaz-Rodriguez, Lopez-Molina 2008) attribute the accompanying phenomena to strain ranges. They confirm with research that small strain is the range characterized by loss of material continuity and a rapid change in stiffness. Similar conclusion based on research was formulated by Sawangsuriya in 2012 (Sawangsuriya 2012).

2.2. Unconventional laboratory research techniques

In the modeling of engineering issues, in terms of high variability of the G modulus value, it is important to determine the expected degradation of the shear modulus value as the strain increases. However, implementation of soil tests in the field of small strain, using conventional laboratory equipment is impossible. At the same time, most building structures are designed in interaction with the subsoil in the range of small strain. Modern measurement methods, applying new solutions to determine the value of deformation modules in terms of their non-linear variability i.e. γ=1·10^{-6}÷1·10^{-3} have become highly required.

Among Polish researchers, one of the precursors and popularizers of determining soil stiffness in the range of small strain is Mirosław Lipiński from SGGW – Warsaw University of Life Sciences. Lipiński promoted legitimacy of taking the G_{max} module as the determinant of the soil reaction to cyclic load (Lipiński 2000) and assigned strain ranges to the previously used laboratory techniques (Lipiński 2012) (fig. 2.4).

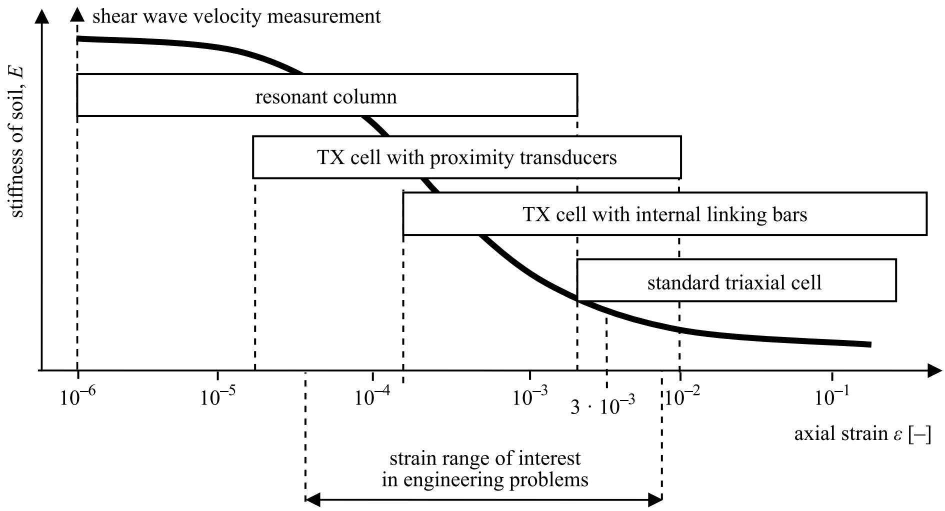

Fig. 2.4. Capability of various laboratory apparatuses for soil stiffness determination
Source: after Lipiński (2012).

Lipiński emphasized (Lipiński, Wdowska 2015) that for problems determined by the fulfillment of the conditions of the serviceability limit state, range of strain usually does not exceed 1·10^{-2} and the most pronounced non-linearity of stiffness changes correspond to shear strain γ<3·10^{-3}. As a consequence the range of small strain seems crucial from the engineering point of view.

Lipiński listed laboratory techniques suitable for assessing stiffness in the range of small strain. These are: a resonant column, a laboratory set of piezoelectric elements for measuring the velocity of shearing and longitudinal waves, a cyclic triaxial compression apparatus and triaxial compression apparatus with local measurement of sample deformation. Author described the possibilities and limitations of the above-mentioned research techniques.

On the example of the modernization of the triaxial compression apparatus, he presented the possibilities of increasing the accuracy in determining soil stiffness. He designed and applied an intra-chamber sample deformation measurement system using proximity sensors. Based on his laboratory work, provided several comments and recommendations regarding the correctness of measurements with piezoelectric bender elements and methods of interpretation obtained from the study of the shear wave velocity.

Lipiński also pointed out that the appropriateness of the laboratory tests for the determination of stress-strain characteristics depends on well--controlled boundary conditions. Knowledge of the state of stress and strain and also control of drainage conditions enable the identification of factors affecting the behavior of the subsoil and the quantification of their impact on the reaction of the subsoil under various loading conditions (Lipiński, Wdowska 2015).

Waldemar Świdziński from IBW PAN (Institute of Hydroengineering of the Polish Academy of Sciences) parallelly has been researching the issue of correct estimation of soil stiffness in terms of small strain. In his research work he uses bender elements – piezoelectric sensors installed in the bases of the triaxial compression apparatus, enabling sending and receiving a signal, mechanical wave propagating throughout the soil sample (fig. 2.5). Świdziński presented the results of research related to the measurement of shear wave velocity in sands (Świdziński, Mierczyński 2010). Author analyzed various types of transmitting signal shapes in terms of the reliability of the measurement results.

Świdziński emphasized that a strongly asymmetric sinusoidal wave allows for a relatively simple interpretation of the receiving signal and determination of the actual time of wave transition through the soil sample. It also showed that the wave velocity in dry sand is much greater than in saturated sand, and that the wave velocity is greater the greater the density of the sand. The stiffness of the soil in terms of small strain is therefore dependent on these soil characteristics.

Świdziński emphasized the advantages of this laboratory test: the non--destructive nature of the method used and the user convenience. At the same time, it draws attention on the problems related to the

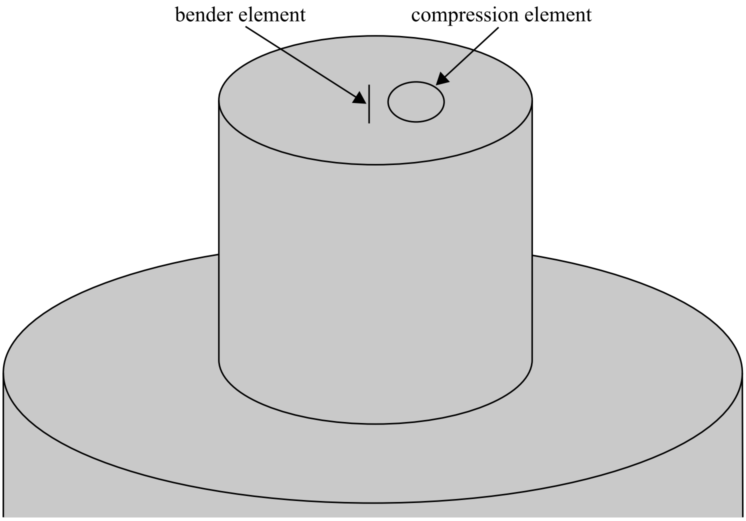

Fig. 2.5. View of Bender Element and Compression Element, piezoelements used in IBW PAN
Source: after Świdziński, Mierczyński (2010).

interpretation of the results in terms of the precise determination of the time of propagation of a given wave throughout a soil sample, as well as problems related to the influence of the anisotropy of the medium on the velocity of wave propagation.

Research in the triaxial compression apparatus with the use of piezoelectric elements was also carried out by Marcin Witowski. In his doctoral thesis (Witowski 2021), he assessed the stiffness of fly ash samples in terms of small strain. For this purpose, he used an additional set of sensors for local deformation measurement.

2.3. Resonant column and torsional shear apparatus

Modern laboratory methods enable soil testing in the range of small strain and allow for a better insight into the complex nature of the soil. One of the devices that enables a multi-faceted analysis of the mechanical properties of the soil in the field of small strain is the resonant column (RC).

The methodology of resonant column test is based on the use of dependence of natural frequency and the elastic shear wave propagation velocity. The research method is also based on the relation between the dynamic shear modulus *G* and resonance frequency of the tested soil sample (fig. 2.6):

$$G_0 = G_{\max} = G_{\mathrm{dyn}} = \rho \cdot V_S^2 \tag{2.8}$$

where:

$G_{\max}$ – maximum shear modulus,
G_0 – initial shear modulus,
G_{dyn} – dynamic shear modulus,
ρ – bulk density,
V_s – shear wave propagation velocity.

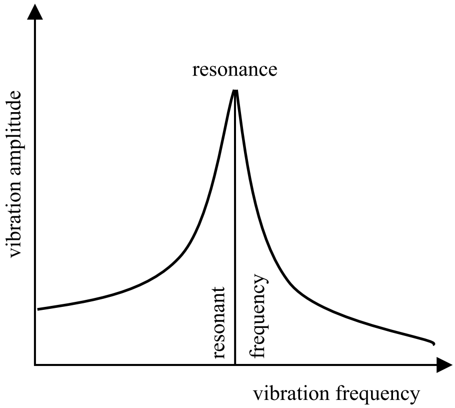

Fig. 2.6. The principle of determining the resonant frequency in a resonant column test
Source: after Srokosz et al. (2017).

During the RC test, the electromagnetic rotor of the resonant column loads the soil sample with a harmonic torque. The shear wave velocity value sought corresponds to frequency of rotor vibrations equal to the moment of recording the highest amplitude (resonant frequency). The relationship (2.9) of the circular frequency ω with the wave velocity *Vs*, takes into account the value the mass moment of inertia I_0 of the rotor of the device and the moment of inertia I of sample:

$$\frac{I}{I_0} = \frac{\omega L}{V_S} \tan\left(\frac{\omega L}{V_S}\right) \tag{2.9}$$

where:

L – height of tested cylindrical soil sample.

Lipiński emphasized that the resonant column is the so-called dynamic test (Lipiński, Wdowska 2015). The amplitude and frequency of the load allow testing to a maximum strain value of not more than $3 \cdot 10^{-3}$ (fig. 2.4).

This range fully corresponds to the requirements of typical problems occurring in common engineering practice. In terms of functionality, related to the useful range of observed deformations, the resonant column test is a suitable method.

Research using a resonant column has been conducted since the 1930s, when initially the main purpose of this research method was the analysis of properties of soil and rocks subjected to harmonic vibrations, representing seismic loading.

The first devices were created in Japan thanks to Iida (fig. 2.7), who developed the theory related to resonance research in the 1930s. At the time, author was doing research on fine-grained soil samples not yet subjected to isotropic compression. The method was first published in 1936 with the co-authorship of Ishimota (Ishimoto, Iida 1936).

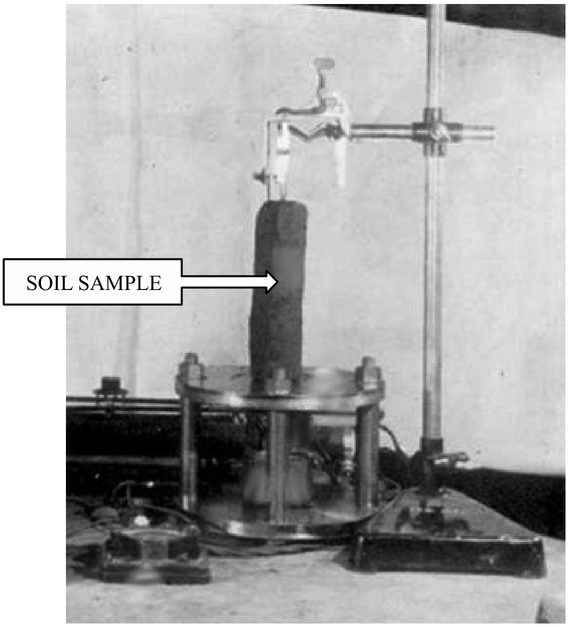

Fig. 2.7. A prototype of a resonant column
Source: after Ishimoto, Iida (1936).

Another device, which is the prototype of today's RC devices, is an American construction designed in 1938 by Birch and Bancroft, which was used to determine the torsional vibration velocity of rock samples (Birch, Bancroft 1938).

Since the 90s of the last century, there has been increased interest in research in the resonant column and the extension of the application of its results to the description of issues related to the interaction of monotonic and static loads. Therefore there was an intensification of work on the improvement of various apparatus designs, based on the principle of operation of the resonant column. Particularly intensive and effective work was carried out by the team centered around Professor Stokoe. The work was focused primarily on increasing the versatility of the device, which, using the same driving element, would enable simultaneous testing of a soil sample in different variants of loading with a torque. This applies to the anisotropic load of the sample fixed in the base, in the range of small strain (Allen, Stokoe 1982, Ni 1987, Kim, Stokoe 1995).

Subsequent modifications of the apparatus focused on extending its functionality by testing cyclic, torsional shear. A major contribution in this field was made by Drnevich, who helped to standardize the test procedure (Drnevich 1978, Drnevich et al. 1978) by developing a mathematical model that is important for both apparatus functions: the RC resonant column and the TS torsional shear apparatus. This innovative construction work resulted to create a dual-function RC/TS apparatus (fig. 2.8).

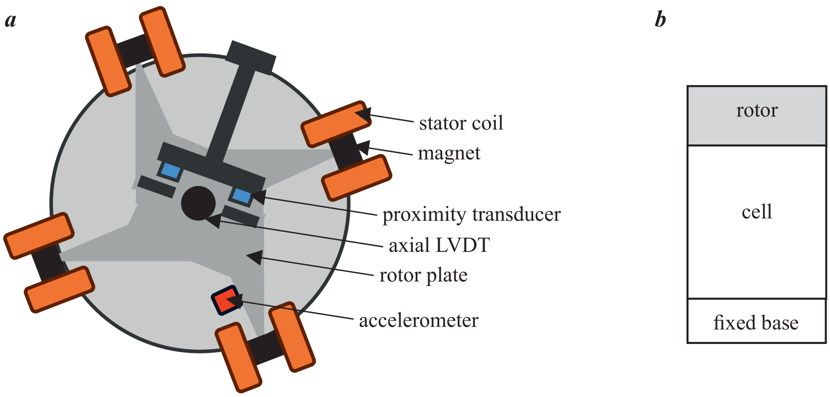

Fig. 2.8. RC/TS apparatus at the University of Austin, USA: *a* – top view of the rotor, *b* – rotor location of fixed-free RC/TS
Source: own work after Stokoe et al. (2016).

Full use of all operating modes of the RC/TS device enables testing in the range from very small (10^{-6}) to large (10^{-1}) strain with significant margins of mutual overlap. The main difference between RC and TS mode is the frequency range and amplitude of the load. In TS mode, soil material tests might be performed by controlling the range of load or displacement and a frequency of closed torsion cycles. Soil samples can be tested under isotropic loading conditions.

The interpretation procedure of the measurement results recorded in this apparatus is based on the model of a cylindrical rod with one degree of freedom (fig. 2.9). The rod is subjected to torsional vibrations.

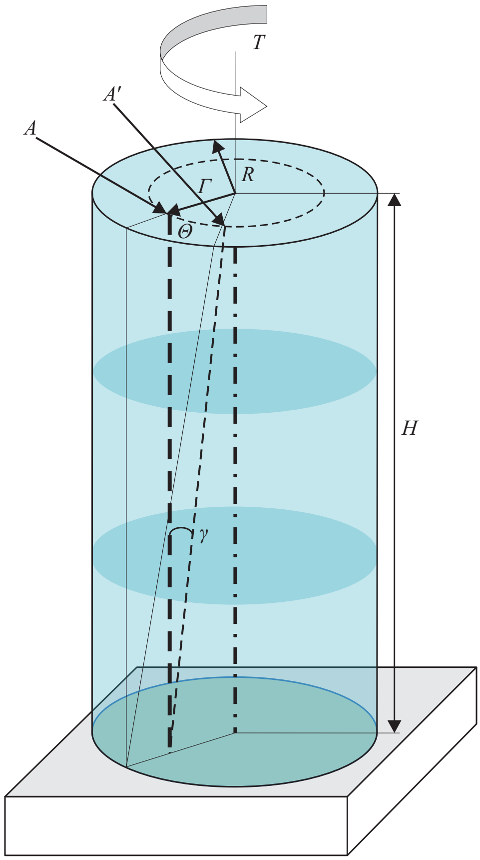

Fig. 2.9. RC/TS model for results interpretation: T – torque, H – sample height, R – sample radius, r – reference radius, A and A' calculation point before and after displacement
Source: after Dyka and Srokosz (2012).

The soil sample is placed in a cell on a pedestal equipped with a porous stone. In the cell the soil sample is subjected to isotropic compression. An electromagnetic drive system is attached, through the top cap, to the upper surface of the sample and generates torsional harmonic vibrations. The apparatus can carry out a controlled process of saturation and isotropic consolidation. The view of the apparatus is presented in figure 2.10.

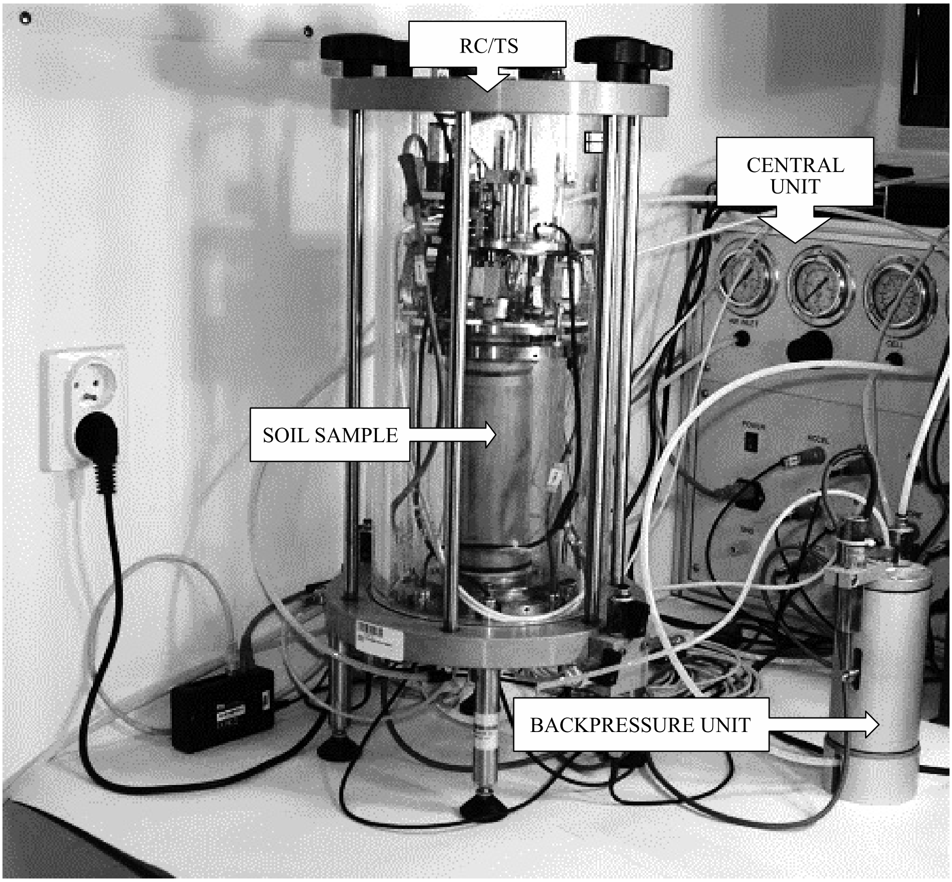

Fig. 2.10. RC/TS apparatus (WF8500 model)
Source: after Srokosz et al. (2017).

Testing in a resonant column is considered now as highly reliable, practical and relatively convenient in terms of interpretation of the measurement results (see: Mayne et al. 2009, Cabalar 2010, Chong, Kim 2017, Hoyos et al. 2015, Madhusudhan, Senetakis 2016, Senetakis et al. 2015, Senetakis, Payan 2018, Shin 2018).

2.4. Selected applications of resonant column in basic research

The resonant column has been used for years to study the basic parameters of soil stiffness in the range of small strain. This chapter presents examples of basic and applied research selected by the author.

One example is determining the value of Poisson's ratio. This parameter is very often used in elastic and elastoplastic analysis, but it is very rarely determined in laboratory studies. Lipiński and Wdowska presented a method of obtaining the dependence of the Poisson's ratio as a function of shear strain (Lipiński, Wdowska 2015), on the basis of the results of tests in a resonant column and a cyclic triaxial compression apparatus.

Authors carried out laboratory tests on high-placticity clay samples from the foundation subsoil of the second line of Warsaw subway (fig. 2.11). Poisson's ratio (ν) was calculated from two modules obtained directly from the tests, from the following formula (2.10), derived from the theory of elasticity:

$$\nu \frac{1}{2}\frac{E}{G} - 1 \tag{2.10}$$

where:

E – deformation modulus obtained on the basis of cyclic triaxial compression test,

G – shear modulus obtained on the basis of resonant column test.

To compare E and G modules, Lipiński and Wdowska (2015) converted the strain determined from the triaxial compression tests into the shear strain (ε_S), using formula (2.11):

$$\varepsilon_s = \frac{2}{3}(\varepsilon_v - \varepsilon_h) \tag{2.11}$$

where:

ε_v – vertical component of strain,

ε_h – horizontal component of strain.

On the basis of the research, obtained value of Poisson's ratio ν is a function of strain. Results are presented in figure 2.11.

Method allows not only to observe the change in the value of this parameter, but also helps to determine the extent of strain, in which the soil behavior is elastic or hypoelastic. In presented example the limit of maximum strain within the elastic range is 0.01% and for the hypoelasticity it is 0.07%.

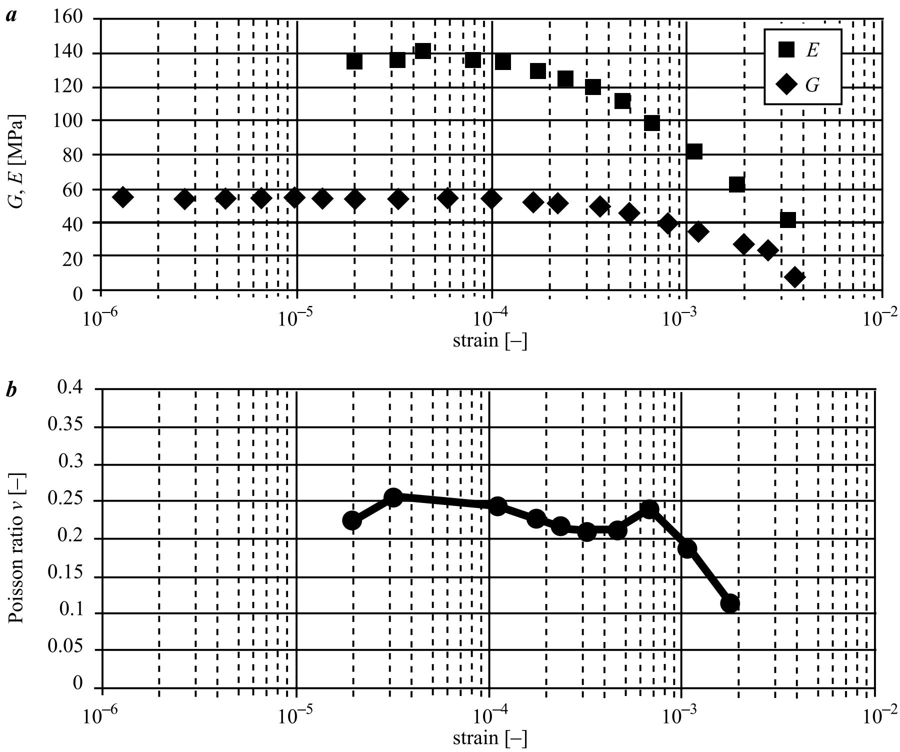

Fig. 2.11. The dependence of stiffness parameters of high-plasticity clay on the value of shear strain, obtained on the basis of the results of tests in the resonant column and a cyclic triaxial compression apparatus
Source: after Lipiński and Wdowska (2015).

Moreover, the above example shows that a comprehensive analysis of the results obtained from resonant column and cyclic triaxial compression apparatus is a source of qualitatively and quantitatively better information on soil stiffness. It proves the high potential of synergic interaction of both types of research.

Another example of the application of RC to basic research was presented by Wichtmann in his habilitation thesis from 2016 (Wichtmann 2016). The author has made approx 650 RC tests with additional longitudinal wave measurement on non-cohesive soil samples characterized by 65 different grain size distribution curves (mainly composed of quartz sands).

Tests on samples with different grain size distributions showed that:

– for constant values of the cell pressure and void ratio, the shear modulus $G_{\max}$ does not depend on the average grain diameter, but it decreases rapidly with the increase of the uniformity coefficient;

– an increase in the share of fine fractions in the tested sample results in a decrease values G_{max};
– for a specific strain amplitude γ_{max}, the function $G(\gamma_{max})/G_{max}$ decreases with the increase in the value of the uniformity coefficient;
– no relationship was found between the function value $G(\gamma_{max})/G_{max}$ and the value of the average grain diameter or the share of fine fractions.

Furthermore, The results of the RC studies allowed for the development of formulas for determining G_{max} and $G(\gamma_{max})/G_{max}$ taking into account the impact of the content of individual fractions in the grain size curve.

In another publication (Wichtmann et al. 2017) Wichtmann studied the correlations between "dynamic" (for small small strain) and "static" (for large strain) values of stiffness parameters. For this purpose, he conducted tests in a resonant column, an oedometer and a triaxial compression apparatus in drained conditions, using sand and gravel samples of 19 grain size distribution curves. Correlations between "dynamic" and "static" deformation modulus were already proposed in the form of a diagram in 1970 by Alpan (Alpan 1970). This proposal was supplemented in 2002 *Recommendation of the Soil Dynamics Committee* of the German Geotechnical Association (Deutsche Gesellschaft für Geotechnik... 2002) and the results of Benz's PhD thesis from 2007 (Benz 2007). The final correlation diagram is shown in figure 2.12.

Wichtmann (Wichtmann et al. 2017), based on the above diagram, proposed the relationship (2.12 and 2.13):

$$\frac{M_{\mathrm{dyn}}}{M_{\mathrm{stat}}} = \frac{M_{\mathrm{max.}}}{M_{\mathrm{oedo}}} \tag{2.12}$$

$$\mathrm{M}_{\mathrm{stat}} = \mathrm{M}_{\mathrm{oedo}} \tag{2.13}$$

where:

M_{dyn} – dynamic deformation modulus,
M_{stat} – static deformation modulus,
M_{oedo} – oedometer constrained modulus of elasticity,
M_{max} – maximum deformation modulus,

Knowing the value of Poisson's ratio ν, the "dynamic" shear modulus (for small strain) can be obtained from the formula:

$$G_{\mathrm{dyn}} = G_{\mathrm{max}} = M_{\mathrm{max}} \frac{1 - \nu - 2\nu^2}{2(1 - \nu)^2} \tag{2.14}$$

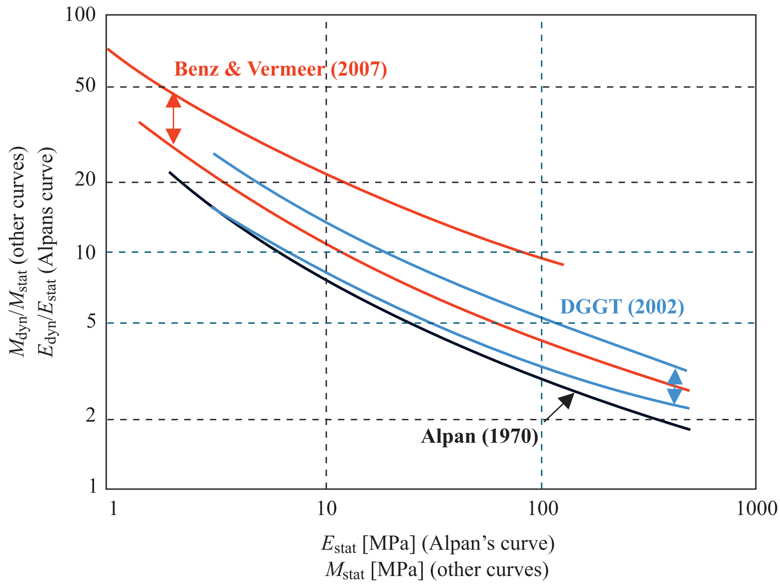

Fig. 2.12. Comparison of the M_{dyn} and M_{stat} correlation contained in the "Recommendations of the Soil Dynamics Committee" of the German Geotechnical Association (DGGT) with the original proposal of Alpan and supplemented by Benz Source: after WICHTMANN et al. (2017).

Wichtmann on a basis of research carried out on sand samples, e.g. in the resonant column, checked the correlations contained in the diagram (fig. 2.12) and confirmed that they can be used for direct estimating "dynamic" strain modulus values from "static" values.

An attempt to correlate "static" and "dynamic" modules was also made by MASSARSCH (2004), comparing shear deformations caused by given load velocities in a "dynamic" resonant column and a "static" test of direct shear of sand samples (fig. 2.13 and 2.14).

In the case of the dynamic RC test (fig. 2.13), when the vibration frequency was 8 Hz and the amplitude of shear strain was 0.0001%, the strain rate was 0.0032%/s. On the other hand, in the case of "static" measurement in the direct shear apparatus (fig. 2.14), the test lasted 1.75 h until shear strain of 2% was reached. In a consequence, the average strain rate was 0.00032%/s. The key aspect of the issue raised in the Massarsch's work is the fact that the value of the shear modulus G corresponding to strains below 0.0001% can be considered constant. This is a range of very small strain – the beginning of the degradation curve of the G module.

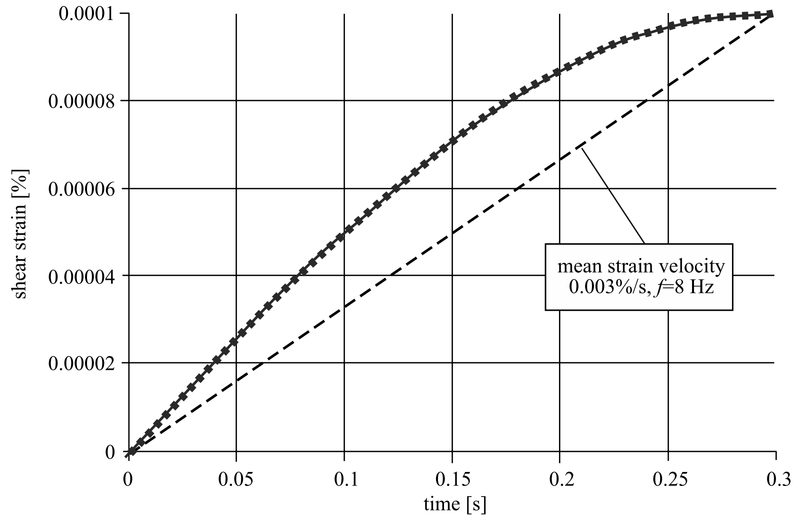

Fig. 2.13. Examples of results obtained from tests in a resonant column
Source: after Massarsch (2004).

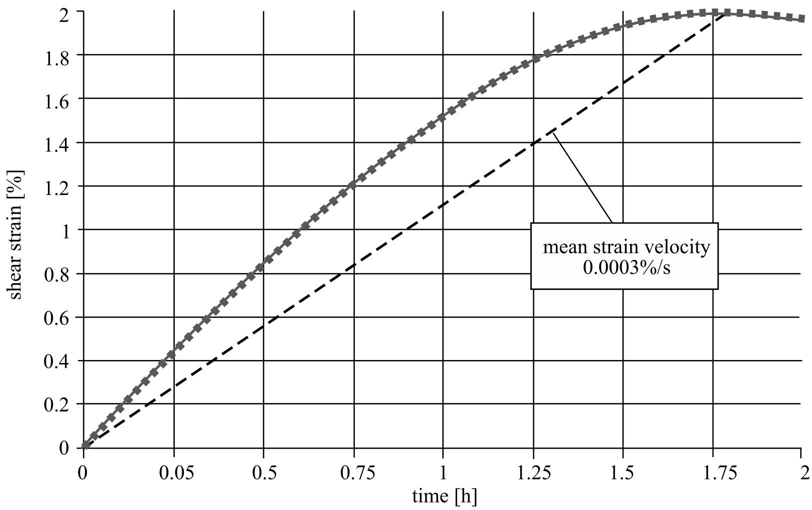

Fig. 2.14. Examples of results obtained from tests in a direct shear apparatus
Source: after Massarsch (2004).

In the case of both studies, the obtained results are complementary in terms of determining the starting point and the final stiffness degradation curve and according to Massarch, enable to obtain a complete degradation curve of the G modulus in terms of both ranges small and large strain. This is an extremely important conclusion that relates to the possibility of combining the results of static and dynamic tests in order to obtain reliable information on the mechanical properties of the soil, in particular those related to changes in its stiffness.

2.5. Selected applications of RC/TS tests in engineering practice

An example of the practical application of RC/TS tests is the design of the foundations of marine structures subjected to dynamic loads.

The foundation of the wind farm is constantly subjected to dynamic loads, which results from the specificity of the turbine operation and gusts of wind. Turbine manufacturers pay attention to the special conditions of the secondary limit state, i.e. maximum settlement and tilting of the structure, the exceeding of which may lead to high values of moments destabilizing the overall stability of the structure (Król 2013).

At the same time, according to (Król 2013 after PN-81/B-03020:1981, PN-EN 1997-1), there are no generally available and detailed guidelines regarding the design of foundations for wind power plants, in Polish standards. The author draws attention to the lack of instructions for conducting soil tests for these specific structures. Therefore, it is necessary to use the turbine manufacturer's guidelines or the results obtained from an experiment carried out under similar conditions.

In accordance with the Polish regulation of the Minister of Transport, Construction and Maritime Economy of April 27, 2012 on determining geotechnical conditions for the foundation of buildings (DZ.U. z 2012 r., poz. 463), there are distinguished objects of the third geotechnical category including: "unusual building structures, regardless of the complexity of the subsoil conditions, the construction or use of which may pose a serious danger to users". This entry applies wind farms.

Moreover, for buildings of the third geotechnical category, the scope of tests should depend on the expected degree of complexity of the subsoil conditions, as well as the specificity and nature of the building structure or the type of planned geotechnical works. Tests should specify the mechanical parameters of the soil, i.e.: internal friction angle, cohesion, high shear strength under conditions undrained and also shear modulus, obtained in laboratory or field tests. This forces the designer to look for correlation formulas outside the scope of the standards applicable in the country, in order to determine the values of the missing parameters.

Designing the foundations of wind turbines, extended analyzes related to the description of the behavior of the soil subjected to dynamic/cyclical impacts from the structure should be considered (Król 2013).

The basic mechanical properties of the soil in terms of small strain are characterized by the initial values of the modules: shear G_0 (G_{max}) and deformation E_0 (E_{max}). The above parameters can be obtained on the basis of the results of specialized field tests: SCPT (Seismic Cone Penetration Test), SDMT (Seismic Dilatometer Marchetti Test) and laboratory tests – in a resonant column (Zaremba 2013).

Summarizing the domestic conditions, the following are indicated:

- lack of clear guidelines for designing the foundations of wind farms;
- the need to take into account the non-linear subsoil behavior;
- taking into account the variable stiffness of the soil in the range of small strain;
- freedom in the selection of a research method that allows for an accurate assessment of the subsoil characteristics that leads to safe and economic solutions.

In the Arany's article (Arany et al. 2017), a simplified procedure for designing the foundations of offshore wind farms was proposed, in which it is recommended to use, among others, RC tests.

Arany pointed out that the dynamic stability of the object may be endangered by changing the natural frequency of the structure throughout the life cycle of the turbine. Under the influence of environmental loads, the phenomenon of resonance may occur. That might result in a decrease in fatigue life, failure to meet secondary limit state conditions and even catastrophic loss of stability of the overall structure. Therefore, an important aspect of the design process is the analysis of the impact of changes in soil stiffness on the natural frequency of the structure.

Figure 2.15 shows the percentage change of natural frequency in relation to the percentage change in soil stiffness. An exemplary point has been marked on the chart, in which a change in soil stiffness by 40% in relation to the initial stiffness causes a change in natural frequency by 1%. This change in frequency seemingly not significant, in practice, completely changes the adopted design assumptions of the wind turbine structure. In the work Arany et al. (2017) it was found that that the leading aspect in the design of the offshore wind turbine foundation is the accurate prediction of the behavior of the monopile loaded with a cyclic torque. For this reason,

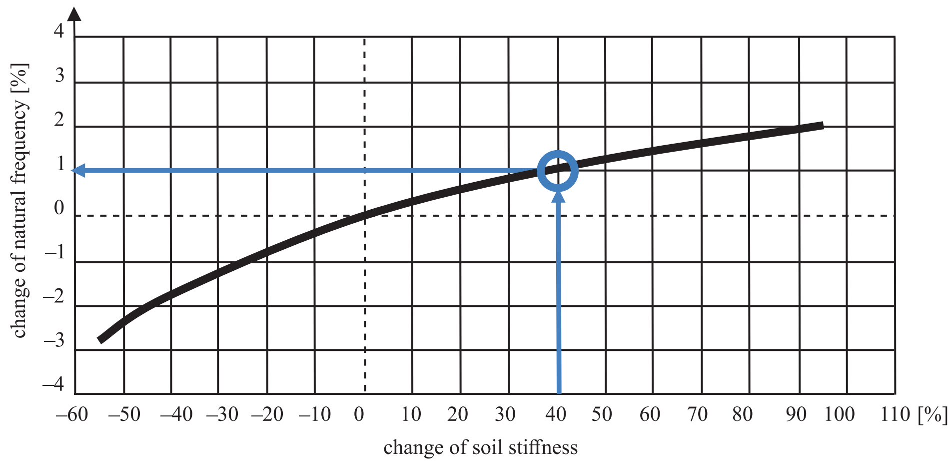

Fig. 2.15. Change of natural frequency as a function of soil stiffness change during wind turbine operation
Source: after ARANY et al. (2017).

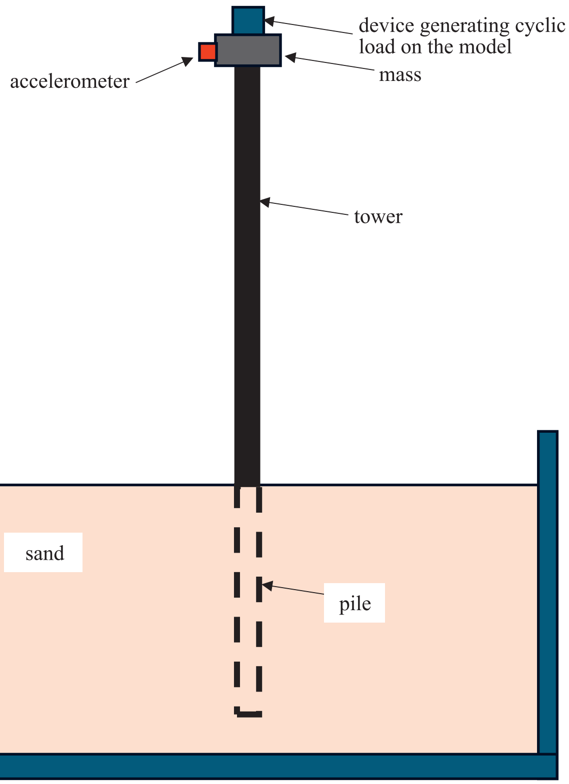

Fig. 2.16. A model of a wind turbine mounted on a monopile
Source: after YU et al. (2015).

it is recommended to conduct soil tests in a resonant column for long-term and reliable prediction of monopile behavior using, for example, the concept of threshold strain (see: Lombardi et al. 2013).

Yu presented an example of practical use of a resonant column test results, that are used to calculate the foundation of wind farms (Yu et al. 2015). Author analyzes the long-term, dynamic behavior of the monopile founded in sand and the impact of long-term, cyclical and dynamic load

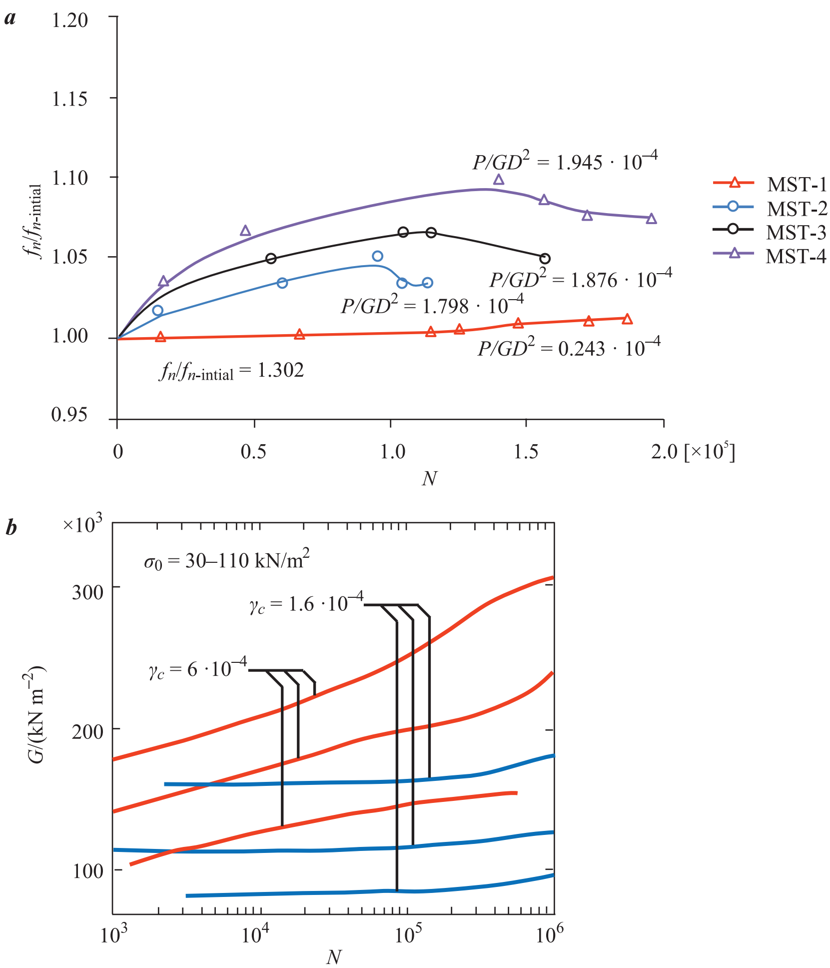

Fig. 2.17. Test results of the wind turbine model: *a* – change of the natural frequency of the structure $f_n/f_{n\text{-initial}}$ (MST-1,2,3,4 – number of sample, *P* – horizontal load, *D* – monopile diameter); *b* – change of soil shear modulus *G* at different strain levels γc under dynamic load with *N* cycles
Source: after Drnevich et al. (1967).

from the structure on the subsoil. In the research a scaled model of a wind turbine was used and set up on a monopile that was subjected to various types of cyclic and dynamic loading. The mass was suspended on top of the model (fig. 2.16). The analyzes carried out were based on the results of tests of sands in a resonant column published by Drnevich (Drnevich et al. 1967) (fig. 2.17).

Yu observed the relationship between the natural frequency of the structure and the change in soil stiffness. The results of the structure model tests showed that the natural frequency of the wind turbine increases with the number of load cycles (see fig. 2.17). It was also found that this change is dependent on the level of shear strain of the subsoil.

It was confirmed that the use of RC test results can help in accurate assessment of behavior of the soil subjected to the dynamic load of the structure. However, despite the available model test results and the advantages of RC testing, the most common practice is to use empirical correlation formulas, neglecting direct laboratory determinations. Most often, this leads to suboptimal design solutions.

Chapter 3

Elastoplastic behavior of soil

The concept of soil modeling using elastoplasticity is developing parallel to the development of research on soil stiffness in the field of small strain.

In 1970, Duncan and Chang developed a hypo-plastic constitutive model of the soil (Duncan, Chang 1970). In 1998, Schanz laid the foundations for a concept equivalent to the Duncan and Chang model (Schanz 1998). In the same year, Schanz, together with Vermeer and Bonier, modified his model by introducing a cap surface. This achievement had a significant impact in later years on the soil modeling, revising the classical constitutive models and leading to the concept known today as the Hardening Soil model.

For the issues raised in this work, a key moment in the history of the development of research on the elastoplastic description of soil behavior is Thomas Benz's 2007 PhD thesis entitled *Small-Strain stiffness of soil and its numerical consequences* (Benz 2007). Benz working with Vermeer in the Stuttgart research center supplemented the Hardening Soil (HS) model with the effect of changing the stiffness of the soil in the range of small strain. The new model was called Hardening Soil Small (fig. 3.1).

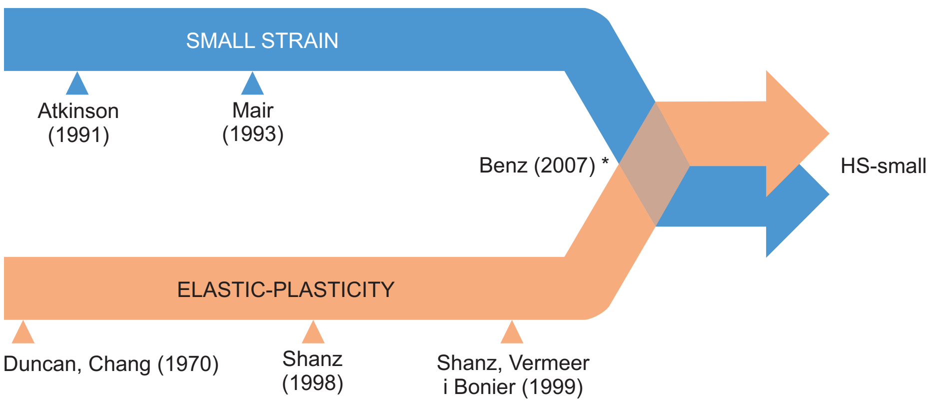

Fig. 3.1. The HS-Small model as a result of research development on small strain and elastoplasticity

The HS model and its extended version, the HS-Small, have been designed to represent the macroscopic effects of soils subjected to monotonic load paths, i.e.: dependence of stiffness on the effective stress state, plastic yielding, volume changes accompanying this phenomenon and a change in stiffness with increasing deviatoric strain amplitude, especially in the range of small strain (Truty 2008).

The model commonly used in engineering practice is Hardening Soil (HS), which has been used in numerical simulations of the following basic macroscopic phenomena occurring in loaded soils:

- reduction of the pore volume in the soil structure during the occurrence of plastic deformations related to the phenomenon of soil compaction;
- change in soil stiffness depending on the state of stress, related to the phenomenon of the increase in the value of deformation modules with the increase in the average stress;
- preservation of the load history in the soil structure related to consolidation;
- strain hardening associated with the generation of irreversible deformations when the plasticity criterion is reached;
- volumetric strain during plastic yielding called dilatancy.

An extension of the HS model is proposed in 2007 by Benz called Small-Strain Overlay Model (SSOM) (Benz 2007). This model has been implemented in the PLAXIS application, which is known to practices all over the world. It functions as HS-Small and assumes a hyperbolic approximation of the degradation function of the shear modulus value, taking into account the history of the state of strain.

The modification of the HS, carried out by Benz, additionally allows modeling in the range of small strain:

- variability of stiffness with increasing amplitude of shear strain;
- hysteretic, non-linear elastic relationship between the state of stress and strain.

In the HS-Small model, the kinematic hardening caused by a change in shear strain is described by the function:

$$f_1 = \frac{q_a}{E_{50}} \frac{q}{q_a - q} - 2\frac{q}{E_{ur}} - \gamma^{PS} = 0 \tag{3.1}$$

where:

γ_{PS} – hardening parameter related to plastic strain,

q_a – asymptotic stress state deviator.
E_{ur} – unloading-reloading modulus,
E_{50} – secant modulus at 50% of the ultimate deviatoric stress q_f.

The ultimate deviatoric stress q_f is described by the Coulomb-Mohr criterion:

$$q_f = \frac{2 \sin \phi}{1 - \sin \phi} (\sigma_3 + c \cot \phi) \tag{3.2}$$

where:
c – cohesion,
ϕ – angle of internal friction.

The function of the strength criterion with volumetric hardening is:

$$f_2 = \frac{q^2}{M^2 r^2(\Theta)} + p'^2 + p_c^2 = 0 \tag{3.3}$$

where:
M – parameter that defines the shape of the yield surface (see fig. 3.2 – cap surface) and is dependent on the at-rest earth pressure coefficient for normally consolidated soils K_0^{NC},
$r(\Theta)$ – van Eekelen function,
p_c – preconsolidation pressure.

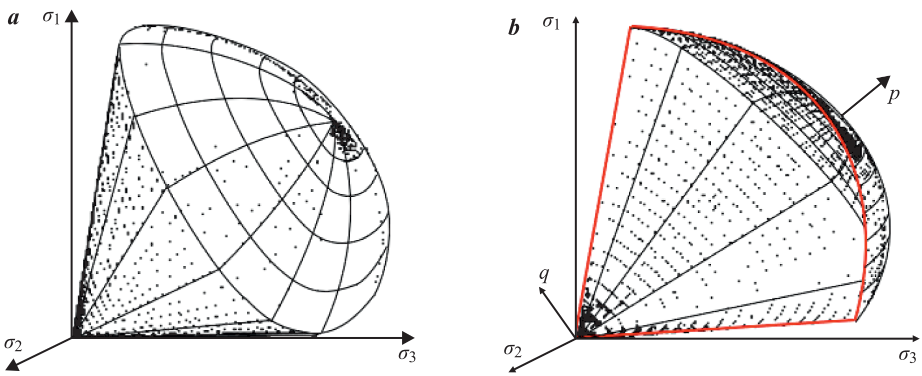

Fig. 3.2. HS-Small model for non-cohesive soils: *a* – plastic yield surface in the model, *b* – slice of surface as a result of intersection with the *p*-*q* plane; $\sigma_1, \sigma_2, \sigma_3$ – principal stresses, *p* – mean stress, *q* – deviatoric stress
Source: after BENZ (2007).

The state of stiffness in the range of small deformations is taken into account by the Hardin and Drnevich (Hardin, Drnevich 1972):

$$G = \frac{G_0}{1 + a\frac{\gamma}{\gamma_{0.7}}} \tag{3.4}$$

where:

a – fitting coefficient,

$\gamma_{0.7}$ – threshold value of shear strain corresponding to 70% of stiffness degradation,

G_0 – initial shear modulus obtained from the formula:

$$G_0 = G_0^{\mathrm{ref}}\left(\frac{p'}{p'^{\mathrm{ref}}}\right) \tag{3.5}$$

where:

p' – mean effective stress,

G_0^{ref} – reference value of shear strain,

m – a parameter describing the non-linearity of the relationship.

The shear modulus G is defined by an S-shaped function that describes the degradation of stiffness in the range of small and large strain (Uliniarz 2017).

Skels and Bondars (2016) demonstrate the legitimacy of applying advanced soil constitutive models in numerical modeling in everyday

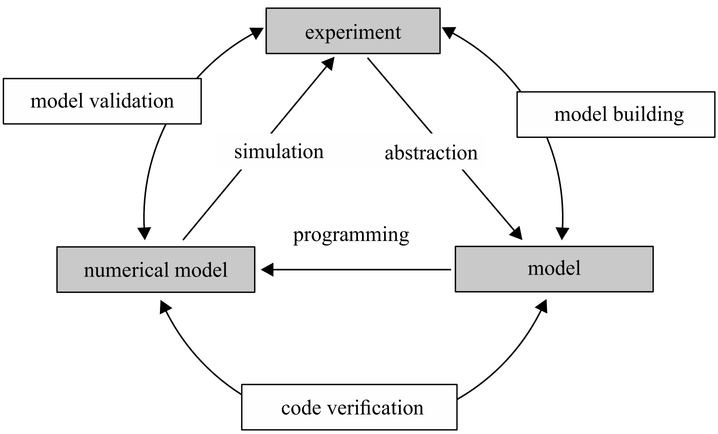

Fig. 3.3. Scheme of creating and validating a numerical model (HS-Small)
Source: after Benz (2007).

engineering practice. The publication presents design calculations for the pile foundation using the HS-Small model in PLAXIS 3D. At the same time, the concept of variable soil stiffness in terms of small strain was applied. Skels and Bondars found that using HS-Small model in multivariate numerical analyzes performed for different diameters of piles, allowed to identify the optimal solution. They emphasized the need to calibrate the HS-Small model (fig. 3.3) with the results of field tests of the pile load test. It is necessary to meet the criteria of reliability and cost-effectiveness of the structure in design practice.

Thomas Benz, in his doctoral dissertation, showed the existence of plastic degradation of stiffness in successive load cycles, causing small strain. Based on e.g. research by River and Bard (after Biarez and Hicher 1994 – see fig. 3.4) writes about the need to take into account the differences between the effects of initial and repeated loading in the constitutive model. Significantly, Benz also assumes that each cyclic load path begins with stiffness with the same initial value of the deformation modulus (see fig. 3.5).

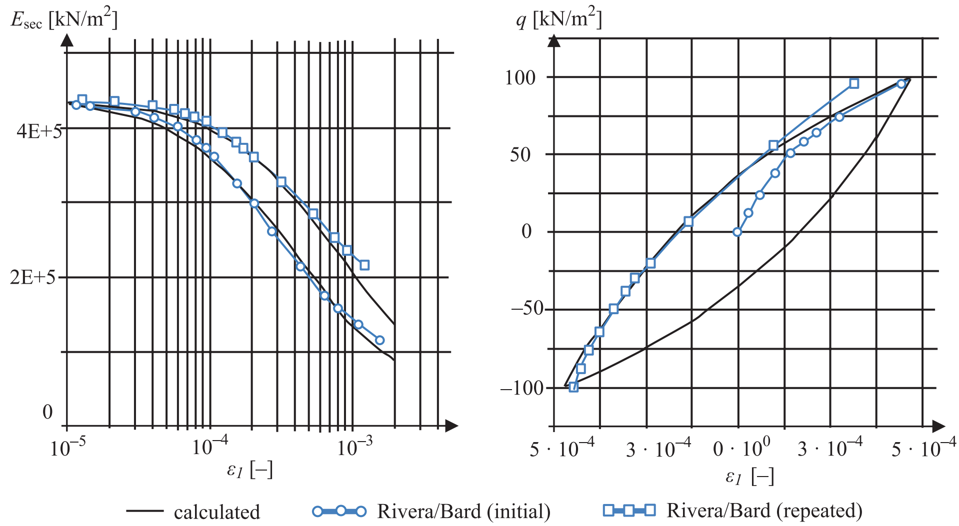

Fig. 3.4. Triaxial compression test result and simulation with the Small-Strain Overlay model: *a* – stiffness degradation in successive load cycles, *b* – hysteresis loop
Source: after Biarez and Hicher (1994).

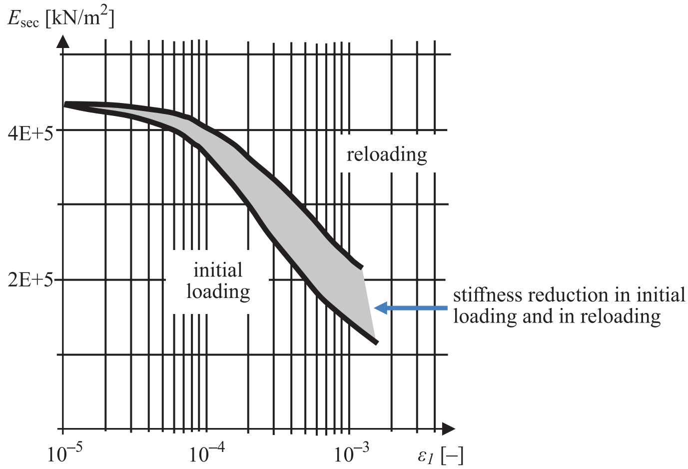

Fig. 3.5. Reduction of soil stiffness during cyclic soil loading
Source: after Benz (2007).

Cudny and Niemunis pointed out that the use of the HS-Small leads to significant errors related to the estimation of deformation values (Cudny, Niemunis 2018). Problem were analyzed on the example of monotonic soil load paths interrupted by cycles unloading and reloading, i.e. dynamic disturbances.

Chapter 4

Research thesis

On the basis of own observations and analyzes carried out, it was noticed that each change of the load direction, in subsequent cycles, causes a change in the stiffness of the soil, visible in the form of abrupt changes in the value of the initial shear modulus G and unclosed form of hysteresis loop (see example in fig. 4.1, tab. 4.1.). It was found that soil materials under certain loading conditions do not behave in accordance with the theoretical models of Maxwell, Kelvin-Voight or Burgers.

Both Maxwell and Kelvin-Voight models were created by combining the components of the models: viscous Newton and elastic Hooke in various configurations. In the Maxwell model, this connection is parallel, and in the Kelvin-Voight model, connection is serial. The Burgers model was created from a serial connection of both of these models. Therefore, all these models are based on the assumption that soil is a continuous, isotropic material and exhibits the properties of a viscoelastic body (Kisiel 1967). This assumption is the theoretical background for the standard calculation procedures implemented in the software of the RC/TS apparatus. Initially, it was the starting point for the analyzes carried out in the work. However, due to the conducted experiments, author proves that the soil reacts to the load as a visco-elastoplastic body, which is inconsistent with the standard assumption of interpretation of the TS test results. In the range of small strain, author registered the occurrence of permanent deformations.

The thesis was formulated that **soil material subjected to small loads inducing small strain, experiences permanent, plastic deformation that might be observed during torsional shear tests carried out in the RC/TS apparatus.**

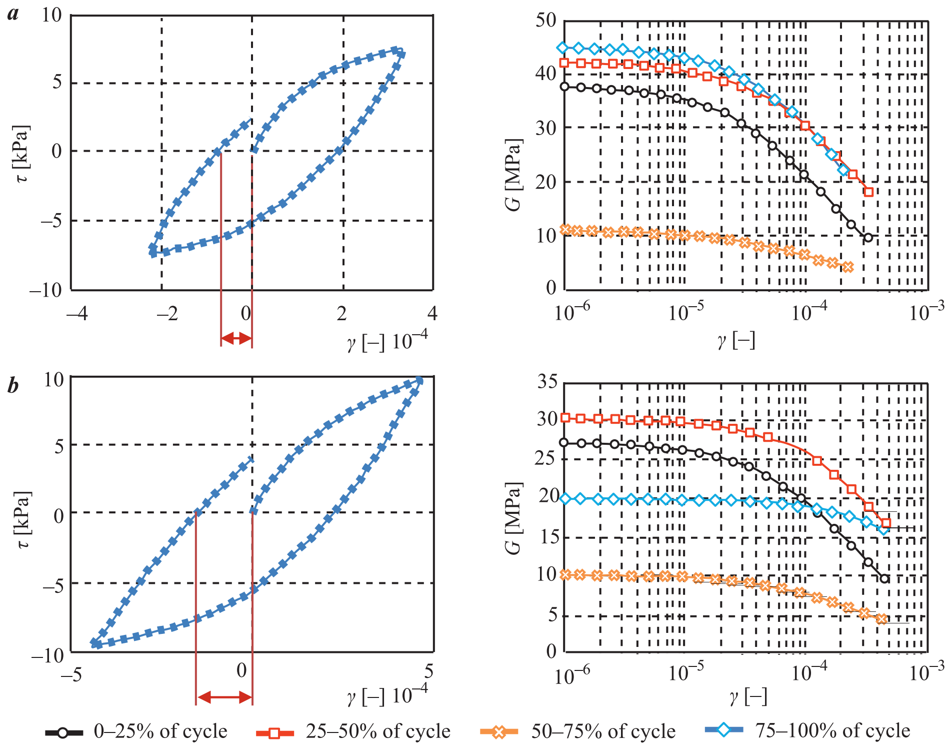

Fig. 4.1. Preliminary results of permanent deformation and degradation of soil stiffness in successive load cycles: *a* – sample TS4913, left: unclosed hysteresis loop, right: abrupt changes in the value of the initial shear modulus *G*, *b* – sample TS5558, left: unclosed hysteresis loop, right: abrupt changes in the value of the initial shear modulus *G*

Tab. 4.1. Characteristics of tested soil samples

Test	Soil	d [mm]	h [mm]	m [g]	d_{50} [mm]	e_{max} [-]	e_{min} [-]	ρ [g/cm^3]	I_S	p [kPa]
TS4913	sand	72.8	143.0	1093.1	0.33	0.71	0.36	1.836	0.94	48.6
TS5558	sand	70.0	143.0	1109.7	0.33	0.71	0.36	2.016	0.99	28.6

Explanations: d – diameter, h – height, m – mass, d_{50} – the diameter of the particles at 50% in the cumulative distribution, e – void ratio, I_S – compaction index, p – confining pressure; TSXXYY is the code name of the load path – test ID due to standard software of the RC/TS where XX and YY represent minute and second respectivelystart of the test.

Chapter 5

Standard methodology for torsional shear test

5.1. RC/TS apparatus

The RC/TS WF8500 apparatus is a device that is part of the equipment of the geotechnical laboratory of the University of Warmia and Mazury in Olsztyn. The WF8500 is a fixed-free type resonant column with the ability to operate in the TS torsional shear mode (fig. 5.1). The device is working for determining the mechanical properties of the soil related to its stiffness, including the value of the shear modulus *G* and the damping coefficient *D*.

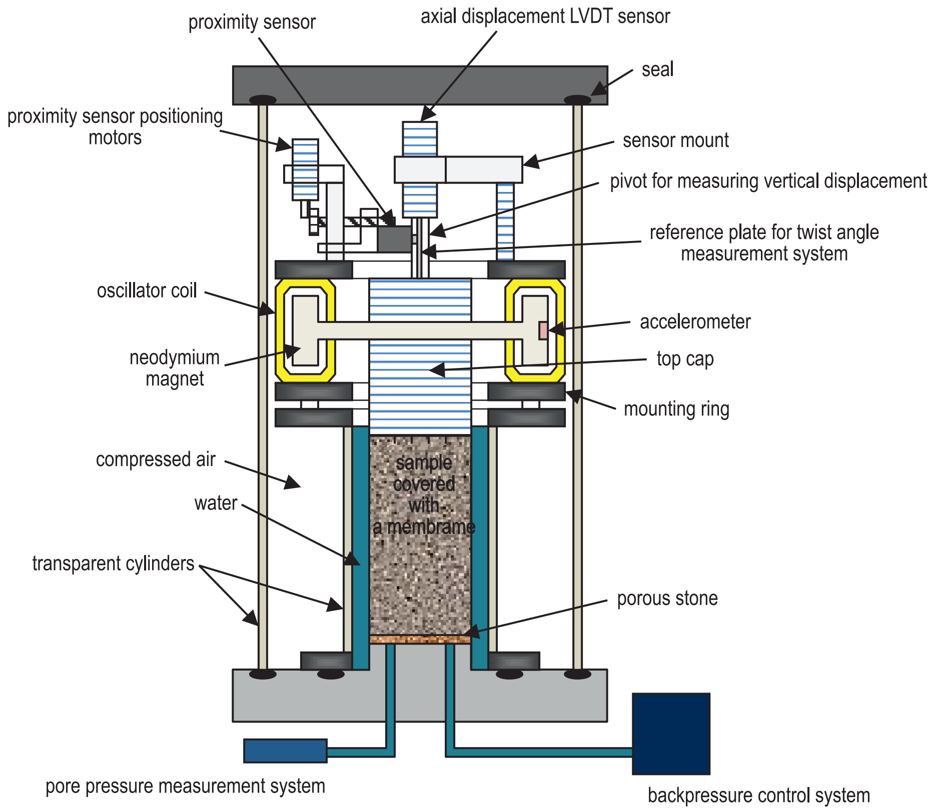

Fig. 5.1. Diagram of the RC/TS apparatus with description of subassemblies: Source: after Srokosz et al. (2018a).

A detailed description of the testing technique and interpretation of the results are included, among others, in (Srokosz et al. 2017, Dyka, Srokosz 2014). The measuring method uses the phenomenon of propagation of elastic waves in the soil material of the tested sample, caused by its cyclic twisting.

RC/TS WF8500 device operates in the frequency range of 10-300 Hz and allows to generate shear wave corresponding to the range of small and very small strain. The apparatus enables testing of a full, cylindrical soil sample with a diameter of 50 mm or 70 mm. The most important advantages of the device are:

- the ability to perform RC, TS and free vibration tests (free decay, FD) on the same sample;
- fully automated processing of results and immediate obtaining of G and D value as result;
- the possibility of smooth adjustment of the level of strain and the value of isotropic pressure at which the values of the G and D parameters are determined (this allows to determine the relationship $G(\gamma)$ and $D(\gamma)$ for different values of effective stress.

The reaction control of the tested soil sample is provided by a set of sensors (tab. 5.1).

LVDT sensors (Linear Variable Differential Transformers) are inductive displacement sensors consisting of a ferromagnetic core that moves inside coils encased in a sleeve-shaped cover. The non-contact movement of the core in relation to the sensor coils causes a differential change in the magnetic field strength, which allows for accurate measurement of the relative position of the core (Scholey et al. 1995). In the RC/TS apparatus, this sensor is used to measure the axial displacement of the sample.

Table 5.1. RC/TS WF8500 set of sensors

Sensor type	Measured feature	Symbol	Producer	Range	Operating voltage	Sensitivity* non-linearity **
LVDT, analog (original)	displacement	SP12.5	DS Europe	±12.5 mm	24 VDC	40 mV/V/mm* 0.2%**
PT, analog (original)	distance	3300XL	Bently Nevada	±5 mm	24 VDC	7.87 V/mm* 0.5%**
Hall, analog (new)	distance	A1324	Allegro Microsystems	±10 mm	5 VDC	5 mV/Gauss* 1.5%**

The advantages of the sensors include: high sensitivity (in practice, limited by the resolution of analog-to-digital converters), linear indication characteristics, resistance to temperature changes and magnetic field disturbances generated by external sources.

Limitations of LVDT sensors applications are associated with assembly problems related to the relatively large mass and size of the sensors, rigid wiring and the possibility of the core getting stuck in the cover.

PT (Proximity Transducers) are non-contact distance sensors and operate due to the phenomenon of eddy current generation in a conductor placed in parallel, at a short distance from the sensor. The movement of the conductor relative to the stationary proximity sensor generates a change in the eddy current in the conductor. As a consequence, this changes the impedance of the coil inside the sensor (Scholey et al. 1995). This change is recorded by the analog-to-digital converter.

The RC/TS WF8500 is equipped with two proximity sensors that register the distance from a steel reference frame that is attached to the top surface of the topcap (fig. 5.2 and 5.3). In the RC/TS apparatus, the measurement results from the proximity sensors are used to determine the value of the twist angle of the sample topcap. Proximity sensors correct their position in relation to the frame using a positioning system.

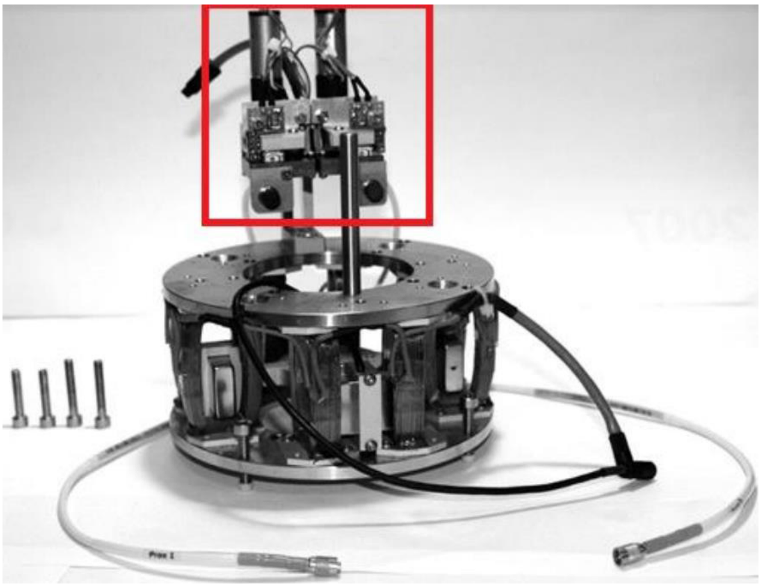

Fig. 5.2. PT mounted on rotor

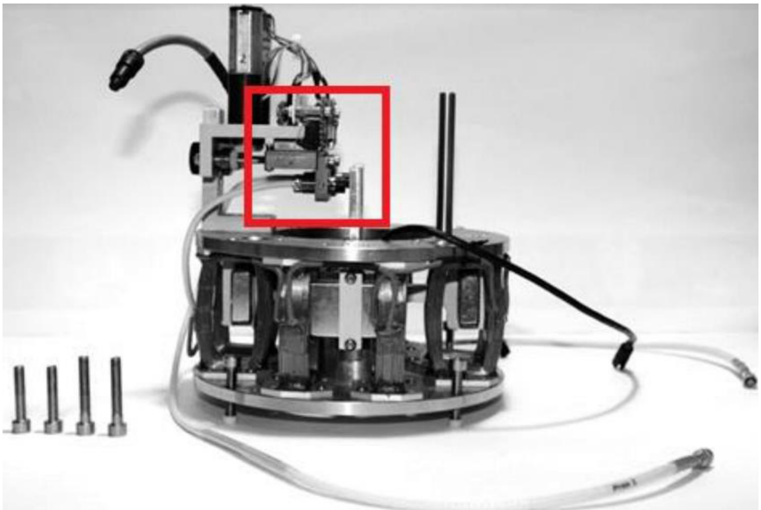

Fig. 5.3. PT, view on the reference frame

The advantage of proximity transducers is their non-contact nature, small size and weight. However, the disadvantage is sensitivity to the influence of the electromagnetic field. The self-noise range of the RC/TS measuring system with PT sensors is close to the value of recorded strain. This is the effect of interference from all components of the standard data acquisition system. For this reason, the author decided to modify the RC/TS apparatus. The improvement of the adopted measurement method meant the use of a different design solution for the data acquisition system and measuring sensors – the use of Hall sensors will be introduced in the next chapter.

Another drawback of the device, the most important from the scientific point of view, is completely closed control software. It makes it impossible to set individual load/strain paths. In order to observe the plastic-permanent part of the deformation of the tested soil, it is not possible to extend the time of recording the geometric parameters of the sample after the TS test.

Figures 5.4-5.6 show screenshots of standard sofware at final stage of test with presentation of RC, TS and FD test results. They show the course of tests of measured physical characteristics and results of automatically interpreted mechanical properties of the tested samples.

In the RC mode, the device enables dynamic generation of a torque with a frequency in the range of 0-300 Hz. The device enables measurement of the resonant frequency by generating torsional vibrations with increasing frequency: stepwise (RC mode) or continuously (RC chirp mode).

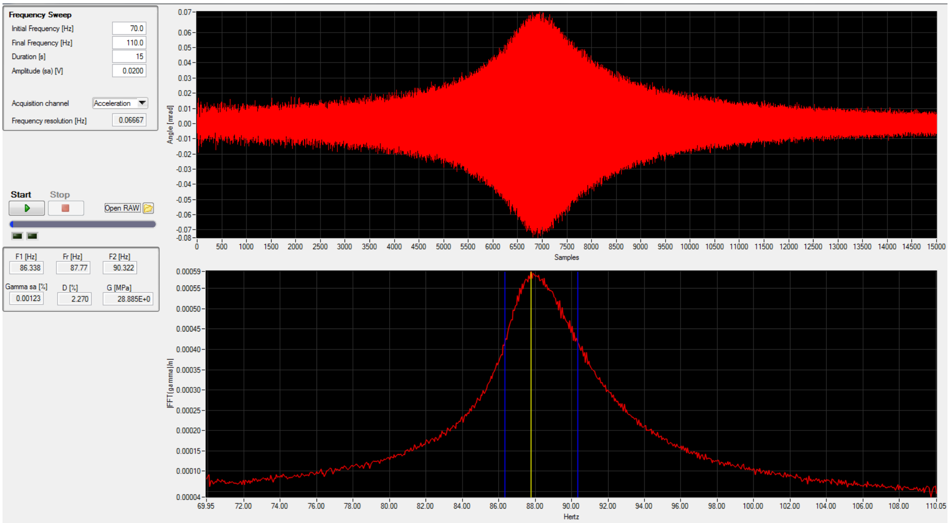

Fig. 5.4. Screenshot with RC test results

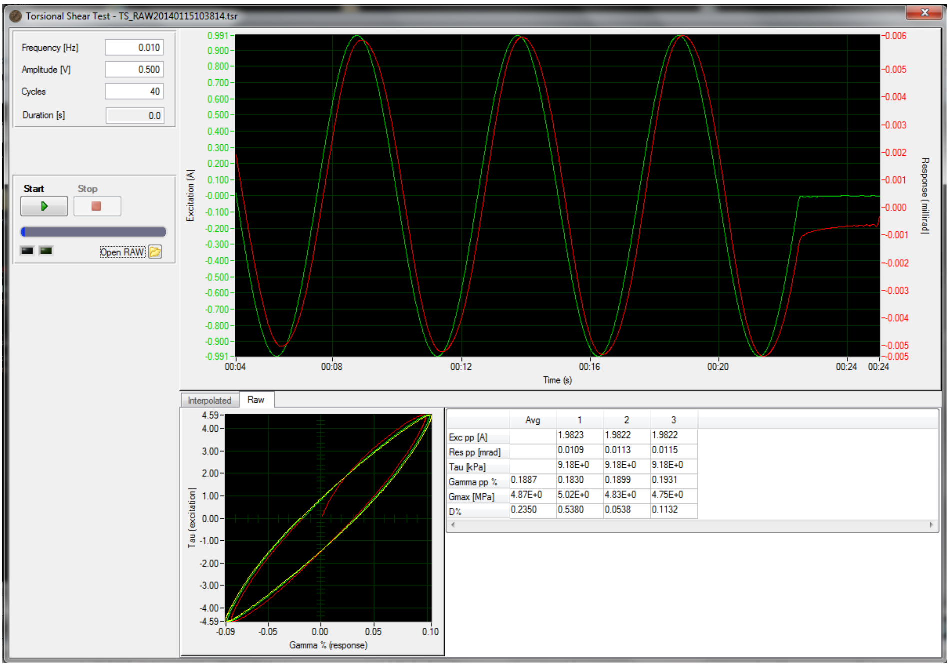

Fig. 5.5. Screenshot with TS test results

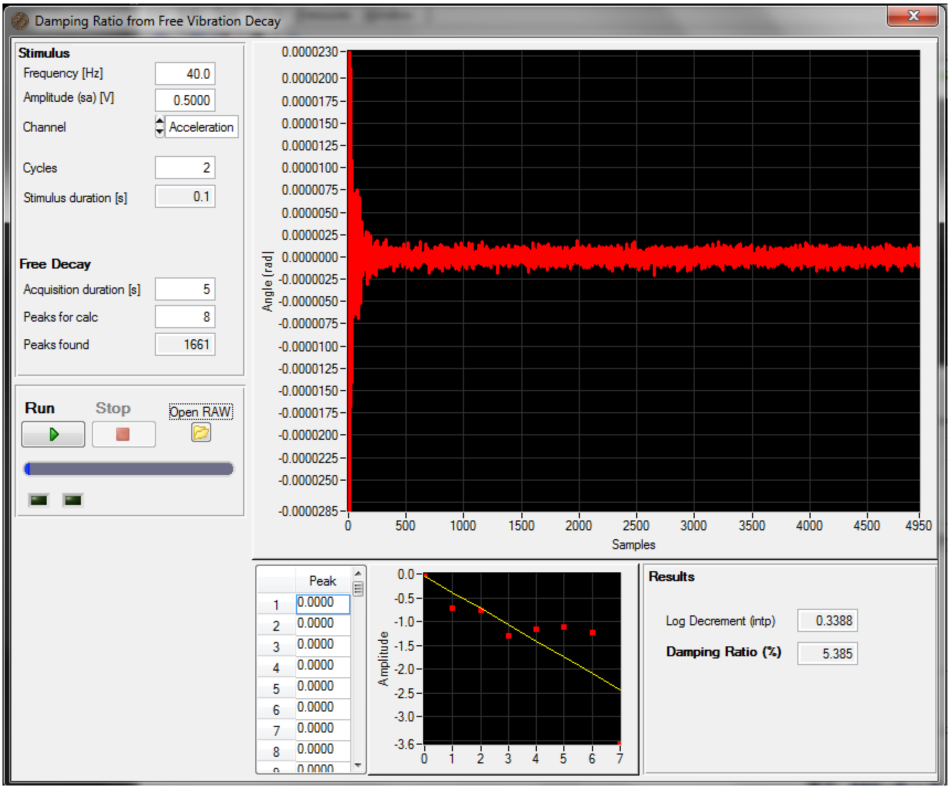

Fig. 5.6. Screenshot with FD test results

The vibration parameters necessary to be entered into the system are: the initial frequency, the final frequency, the amplitude of the electric voltage forcing the vibrations through the electrodynamic force (in the range of ±10 Volts).

In the TS mode, the load parameters are: frequency (in the range of 0-50 Hz) and amplitude (in the range of 0.01-10 Volts) and the number of cycles (3-20 cycles). the apparatus cyclically, with a constant frequency, loads a cylindrical soil sample with a harmonic torque T of constant amplitude T_0 and measures its reaction, which is the twist angle Θ. Due to the set torque frequency f less than 0.1 Hz, the load should not be considered as dynamic but cyclic, slow-changing. Controlling the torque value and the corresponding value of the sample twist angle, the software of the device determines the tangential stress component τ and corresponding shear strain γ. On this basis, the value of the shear modulus G is calculated – the calculation diagram is shown in fig. 5.7. a graphical explanation of the concept of interpretation in fig. 5.8 and 5.9.

The graph of the function of the stress tangent component $\tau(t)$ and the torsion angle $\Theta(t)$ are phase shifted by the angle δ, which proves the occurrence of damping in the sample of soil. Damping causes energy dissipation, resulting in hysteresis in the relation $\tau(\gamma)$ (fig. 5.8).

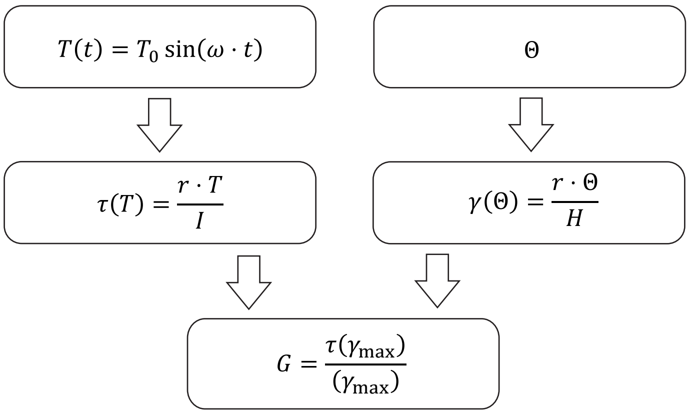

Fig. 5.7. Scheme of standard torsional shear test procedure: t – time, r – reduced sample radius, H – sample height, I – moment of inertia, ω – circular frequency, other notations are explained in the text and in figs. 5.8 and 5.9

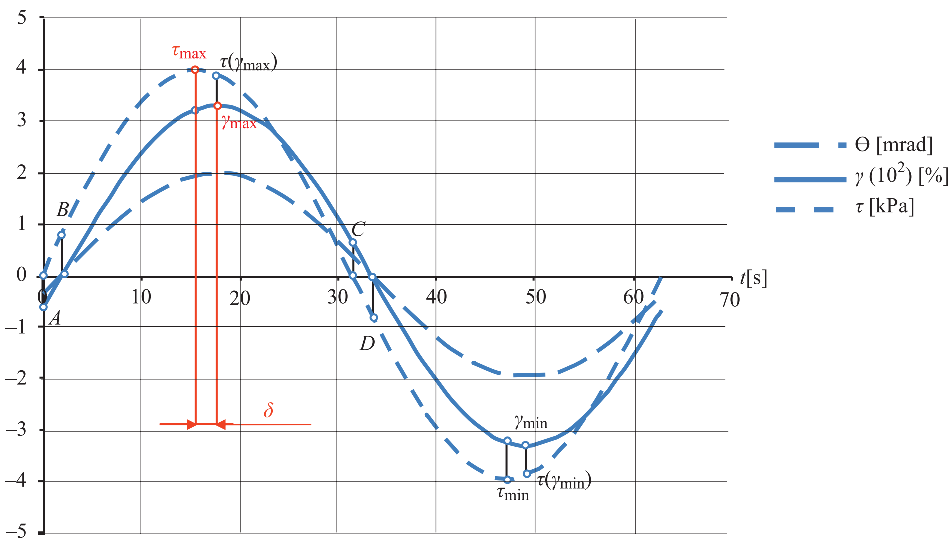

Fig. 5.8. Phase shift of the graph of the function of the tangential stress component and the twist angle of the sample

The hysteresis loop is the standard result of the torsional shear test (fig. 5.9). The interpretation of this result is based on the assumption that in the state of maximum shear strain γ_{max}, elastic energy accumulates in the material, taking the observable form of fully reversible deformations. Some of this energy is lost due to damping. The closed hysteresis loop is the result of complete recovery of the lost energy by the external work done by the rotor of the device.

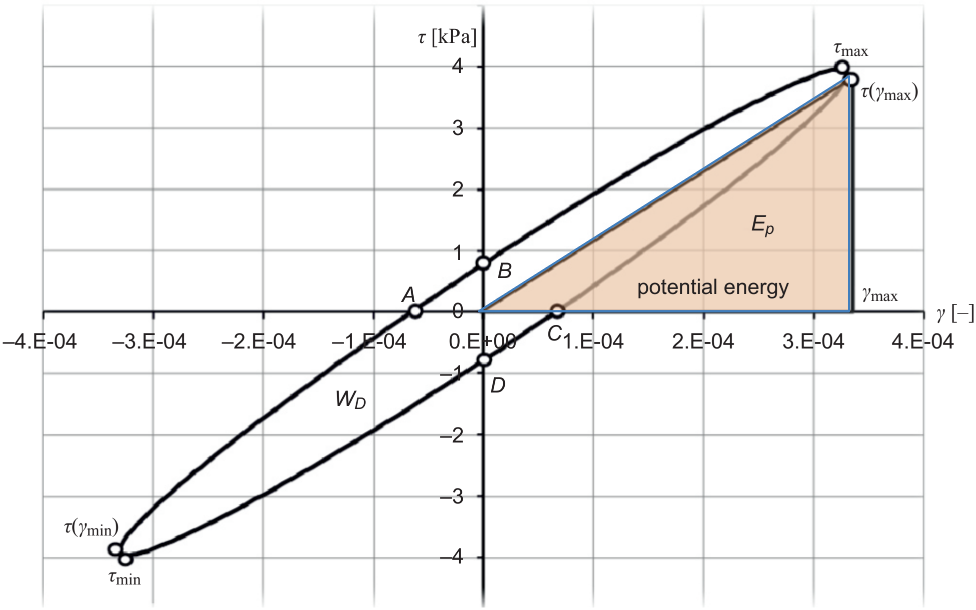

Fig. 5.9. Hysteresis loop – standard TS test result
Source: after Dyka and Srokosz (2012).

Therefore, the key aspect of this issue is the fact that the interpretation of the test results is based on the assumption that the soil medium reacts as a viscoelastic material. The phenomenon caused in the tests is described by the relationship between the torque and the elastic constant, the viscosity coefficient and the mass moment of inertia:

$$I_0 \cdot \ddot{\omega} + C \cdot \dot{\omega} + K \cdot \omega = T(\Theta) \tag{5.1}$$

where:

I_0 – mass moment of inertia [N·m·s^2/rad kg·m^2/rad],
C – viscous damping constant (in the sample) [N·m·s/rad],
K – elastic constant [N·m/rad].

5.2. Viscous damping

According to the standard methodology, damping coefficient (D_{TS}) might be obtained from formula (Srokosz et al. 2017):

$$D_{\text{TS}} = \frac{1}{2\pi}\frac{W_D}{E_P} \tag{5.2}$$

where:

W_D – the dissipated energy, energy absorbed by the material during cyclic torsion (fig. 5.9),

E_P – the potential energy accumulated in the material during elastic deformations, strain energy (fig. 5.9).

The dissipated energy during cyclic torsion of the material sample is regenerated in the system by external work done by the torque $T(t)$ acting on the torsion angle $\Theta(t)$. This energy can be defined by the equation:

$$W_D = \oint \tau d\gamma \tag{5.3}$$

According to the geometric interpretation of the damping phenomenon, as shown in figure 5.9, the value of energy W_D is represented by the hysteresis area described by the functional relationship $\tau(\gamma)$.

Both the tangential stress component and the shear strain are given as functions of time:

$$\tau = \frac{\kappa R}{J} T(t) = \tau_0 \sin(\omega t) \tag{5.4}$$

and:

$$\gamma(\mathrm{t}) = \gamma_0 \sin(\omega t) \tag{5.5}$$

Therefore, the independent variable t can be treated as a parameter, and equation (5.3) can be written as:

$$W_D = \int_{t_p=0}^{t_k=T} \tau\dot{\gamma} dt \tag{5.6}$$

where the limits of integration are defined over one full cycle of loading and unloading of the sample:

$$t_k - t_0 = \mathrm{T} - 0 = \frac{2\pi}{\omega} \tag{5.7}$$

and since it directly follows from (5.5) that:

$$\dot{\gamma}(\mathrm{t}) = \omega\gamma_0\cos(\phi - \omega t) \tag{5.8}$$

the energy W_D can be expressed as:

$$W_D = \int_0^T \tau_0\sin(\omega t)\omega\gamma_0\cos(\phi - \omega t)dt = \tau_0\omega\gamma_0\int_0^T \sin(\omega t)\cos(\phi - \omega t)dt \tag{5.9}$$

$$W_D = \tau_0\omega\gamma_0\left(\frac{t\sin(\phi)}{2} - \frac{\cos(\phi - 2\omega t)}{4\omega}\right)\Bigg|_0^T = \frac{\tau_0\gamma_0}{4}\big(2\omega t\sin(\phi) - \cos(\phi - 2\omega t)\big)\Bigg|_0^{\frac{2\pi}{\omega}} \tag{5.10}$$

$$\begin{aligned} W_D &= \frac{\tau_0\gamma_0}{4}\left(2\omega\frac{2\pi}{\omega}\sin(\phi) - \cos\left(\phi - 2\omega\frac{2\pi}{\omega}\right) - 0 + \cos(\phi - 0)\right) = \\ &= \frac{\tau_0\gamma_0}{4}\big(4\pi\sin(\phi) - \cos(\phi) + \cos(\phi)\big) = \tau_0\gamma_0\pi\sin(\phi) \end{aligned} \tag{5.11}$$

On the other hand, the potential energy E_P representing the momentary accumulation of elastic energy by the material at the maximum strain state, is defined by the triangle area with vertices at points (0.0), ($\gamma_{\max}$, 0) and ($\gamma_{\max}$, $\tau(\gamma_{\max})$). It means the area under the linear-elastic reaction curve of the tested sample material, indicated in orange in figure 5.9. This area can be expressed by the formula:

$$E_P = \frac{1}{2}\gamma_{\max}\tau(\gamma_{\max}) = \frac{1}{2}\gamma_0\tau(\gamma_0) \tag{5.12}$$

$$E_P = \frac{1}{2}\gamma_0\tau_0\sin\left(\arcsin\left(\frac{\gamma_0}{\gamma_0}\right) + \phi\right) = \frac{1}{2}\gamma_0\tau_0\sin\left(\frac{\pi}{2} + \phi\right) = \frac{1}{2}\gamma_0\tau_0\cos(\phi) \tag{5.13}$$

By incorporating (5.11) and (5.13) into (5.2), we obtain:

$$D_{\mathrm{TS}} = \frac{1}{2\pi}\frac{\tau_0\gamma_0\pi\sin(\phi)}{\frac{1}{2}\gamma_0\tau_0\cos(\phi)} = \tan(\phi) \tag{5.14}$$

Taking into account the dependency in the relations (5.15) (Srokosz et al. 2017):

$$\phi = \operatorname{arctg}\left(\frac{C\omega}{K - I_0\,\omega^2}\right) \tag{5.15}$$

the final form of the damping coefficient is obtained:

$$D_{\mathrm{TS}} = \frac{C\omega}{K - I_0\omega^2} \tag{5.16}$$

Due to the small values of the angular frequency ω of torsional shear test loading rate assumptions, the term containing the higher order of ω can be neglected, resulting in a simpler form of expression (5.17):

$$D_{\mathrm{TS}} = \frac{C\omega}{K} \tag{5.17}$$

Therefore, it is assumed that at low frequency rotor operation, the mechanical effects related with mass inertia are negligible. In a consequence, the soil material in the range of small strain, behaves like a viscoelastic body.

Alternatively, the dissipated energy can be understood as work defined by the formula (5.18) (Srokosz et al. 2017):

$$W_D = \oint M_D\, d\Theta \tag{5.18}$$

where:

$$M_D = C\dot{\Theta} \tag{5.19}$$

is the moment of internal forces causing damping and representing the work lost during torsion at the angular velocity $d\Theta/dt$ and C [N·m·s/rad] is the viscous damping constant in the sample.

If we integrate with respect to the parametric variable t, then the formula for dissipated energy will take a form dependent on the viscous damping constant (5.20):

$$W_D = \int_{t_p=0}^{t_k=T} M_D \dot{\Theta} dt = \int_0^T C\dot{\Theta}^2 dt = \int_0^T C\big(\omega\Theta_0 \cos(\phi - \omega t)\big)^2 dt =$$

$$= C\omega^2\Theta_0^2 \int_0^T \cos(\phi - \omega t)^2 dt = C\omega\Theta_0^2 \left(\frac{1}{2}\omega t - \frac{1}{2}\phi - \frac{1}{2}\cos(\phi - \omega t)\sin(\phi - \omega t)\right)\Bigg|_0^{T=\frac{2\pi}{\omega}} =$$

$$= C\omega\Theta_0^2 \left(\frac{1}{2}2\pi - \frac{1}{2}\phi - \frac{1}{2}\cos(\phi - 2\pi)\sin(\phi - 2\pi) + \frac{1}{2}\phi + \frac{1}{2}\cos(\phi)\sin(\phi)\right) =$$

$$= C\omega\Theta_0^2\pi \tag{5.20}$$

Therefore, according to the standard interpretation of TS test results, the effect of cyclically dissipated energy due to damping of soil vibrations is associated with viscosity. In this case, viscosity might be interpreted as a phenomenon described, among others, by Tatsuoka (TATSUOKA et al. 2008), i.e., loading rate effect on the stress-strain behavior.

Chapter 6

Modified methodology for torsional shear test

6.1. Interpretation of results

6.1.1. Numerical methods

The resonant column test is considered a highly reliable method for determining the dynamic and static shear modulus and the damping coefficient soils and rocks (Massarsch 2004, Lipiński 2014, Wichtmann et al. 2017). It is possible to significantly extend the scope of obtained information related to the mechanical properties of the tested soil – including the observation of permanent deformations. However, this involves using modified methods for interpreting standard test results or modifying the methodology of conducting TS tests in RC/TS apparatus.

In this section, author introduces the modified method of interpretation of TS test results. It is the idea of the application the results of simulation calculations, which are performed using applications based on backanalysis: genetic algorythms and Finite Element Method.

The basic concept of determining the non-linear relation $G(\gamma)$ consists in iterative fitting of the relation $\tau(\gamma)$ (in the form of a hysteresis loop, obtained from backanalysis simulation calculations) to the results obtained from TS tests of the soil material.

The most commonly used technique consists in carrying out a full numerical simulation of the experiment and estimating the quality of the solution based on the value of the objective function. This requires the initial assumption of the full course of the variability of $G(\gamma)$ and modifications this variability during the process of minimizing the $L(\cdot)$ function. The problem constructed in this way is very complex and may be incorrectly formulated in the Hadamard sense: no unambiguous mapping of the shape of the sought variability of material stiffness in the shape of the objective function. A direct consequence may be difficulties in converging the iterative process. As a direct consequence, it may be difficult to achieve convergence of the iterative process. This type of interpretation of test results is possible only with "manual" control, i.e. with the use of rich, a priori data on the most probable course of stiffness degradation. Despite these difficulties, the adjustment of the results of the calculations to the results of experimental research can be carried out in stages. This can be done by limiting the optimization process to find the coordinates of a selected set of previously associated points with the corresponding points in the experimental dataset (computing nodes). The analysis of subsequent points and optimization of the local course of dependence G(γ) allows for the simplification of the entire process and a significant improvement in its convergence (Srokosz et al. 2017).

6.1.2. Genetic algorythms

As mentioned in the previous chapter, the phenomenon induced in the research is described in the relationship between the torque and the elastic constant K, the viscosity coefficient C and the mass moment of inertia I_0 (5.1). Damping coefficient D value is consequently dependent on three parameters of the differential equation (6.1) describing the hysteresis loop with the following solution (Srokosz et al. 2017):

$$D_{\mathrm{TS}} = \frac{C\omega}{K - I_0\omega^2} \tag{6.1}$$

An example of using back analysis to interpret TS test results is to determine the damping coefficient D on the basis of the obtained values of three parameters (I_0, C, K) of the differential equation (6.1) describing the hysteresis loop. It is possible to carry out a numerical simulation of the TS test, using for this purpose the back analysis of the results of the actual test. Back analysis methods are based on e.g. on heuristic algorithms using artificial intelligence techniques, e.g. genetic algorithms. Genetic algorithms are a group of numerical techniques based on natural, non-deterministic information processing. Using a fundamental simplification, genetic algorithms look for a solution based on three basic information processing operations: selection, crossing and mutation. In practice, it is possible to implement a huge number of sets of operations, which are based on the processing of coded forms of parameters of the problem to be solved.

Using the heuristic calculation approach, one should look for such values of K, C and I_0 parameters that will allow to obtain a hysteresis loop, the shape of which is adjusted to the result of the torsional soil shear test.

The analysis was performed using the Matlab software. Exemplary results of back analyses carried out for a plastic silty clay sample (code name TS3219) are shown in figure 6.1. It can be seen that the values of parameters K, C and I_0 are not clearly determined by individual analysis results.

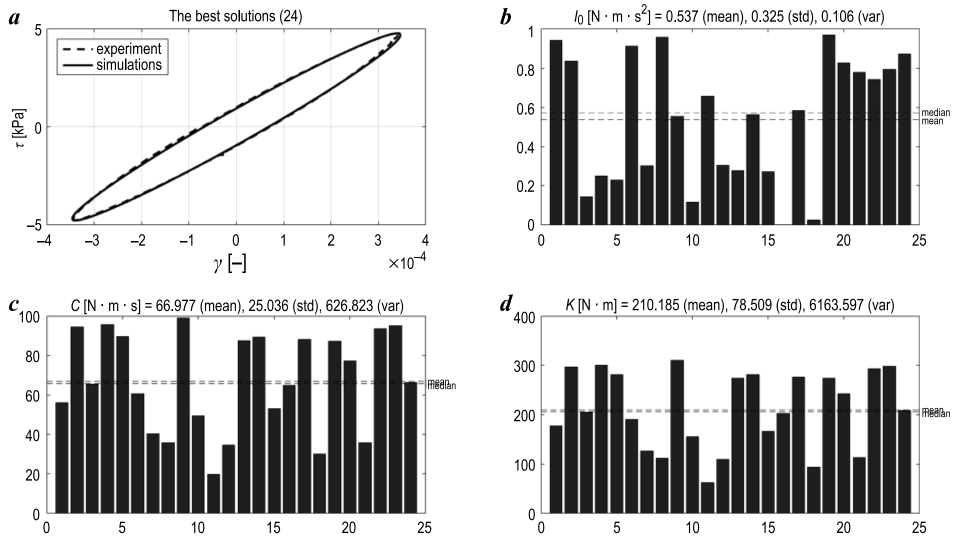

Fig. 6.1. Results of 24 repetitions of the back analysis of the TS3219 experiment:
a – hysteresis loop, *b* – I_0 mass moment of inertia value determination,
c – C viscous damping constant value determination,
d – K elastic constant determination; N – back analysis number

It should be noted that in the hysteresis loop graph (fig. 6.1) the matching of the calculation results to the experiment is exact. However, the values of I_0, C, K parameters obtained from back analyses, describing the hysteresis loops resulting from the theoretical solution, are significantly different from each other. They represent a set of local solutions – figure 6.2. There are infinitely many such solutions.

Despite such different values of I_0, C, K, it turns out that the damping coefficient D is the same for all parameters on the P plane, which is the result of fitting the charts: analytical hysteresis to experimental hysteresis. Therefore, to solve the problem, i.e. to obtain the value of the damping

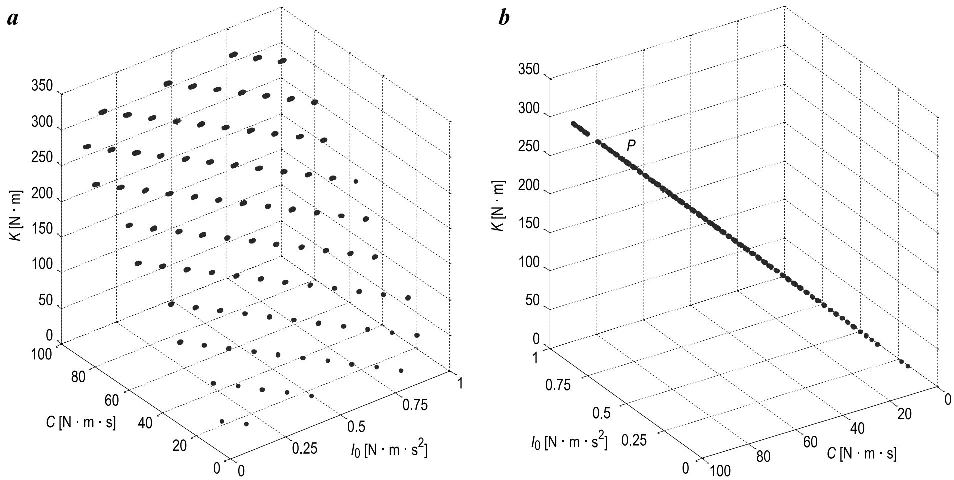

Fig. 6.2. A set of local solutions forming the solution plane (experiment TS3219) – both diagrams show different projections of the same set of points of the solution plane in the parameter space I_0, C, K: a – projection A, b – projection B

coefficient D, it is enough to identify any point with coordinates K, C and I_0 on this plane P (fig. 6.2). Such identification was provided by a genetic algorithm.

In the everyday practice of TS laboratory tests in the RC/TS apparatus, a large influence of external interference is observed. It leads to distorted results of the conducted experiments. Sources of interference are, for example,

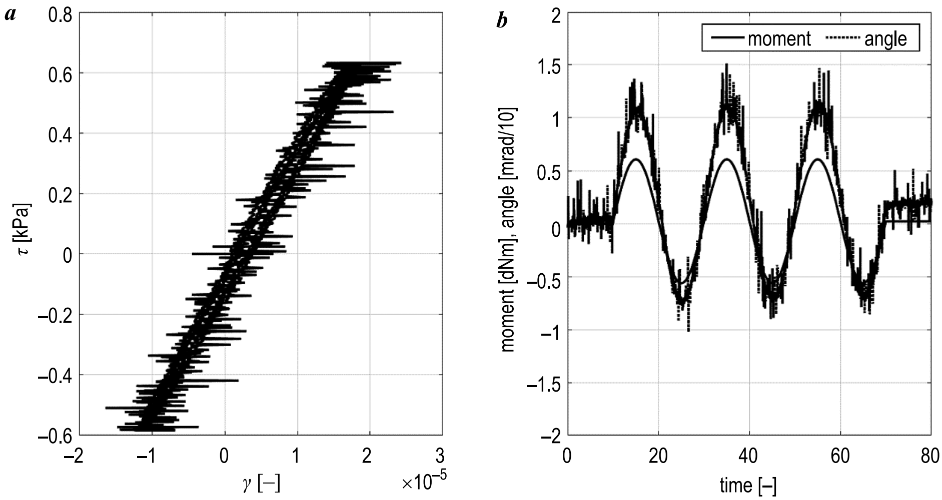

Fig. 6.3. Results of the TS5937 test distorted by noise: a – hysteresis loop, b – harmonically changing moment and angle of torsion

vibrations of the building structure, temperature changes in the laboratory room, etc. This is particularly visible during observation in the range of small strain (fig. 6.3). Experiments carried out at the limit of the resolution of the displacement sensors (i.e. $\gamma \approx 10^{-5}$) of the WF8500 are further hampered by the self-noise of the electronic components of the device.

In the case of noise-free hysteresis loops, the results of the D-values from the tests are consistent with the results obtained from the back analysis method. However, in the case of strongly disturbed data, the proposed method still guarantees obtaining unambiguous values of D and G unlike the standard method implemented in the device software.

6.1.3. Finite Element Method

The basic drawback of the standard RC/TS test methodology is the assumption that the soil material is only subjected to viscoelastic deformations.

This premise is evident in the interpretation of the damping coefficient in the TS test, which is defined as the ratio of the energy dissipated by the material during cyclic torsion to the potential energy accumulated in the material during elastic deformations (see Chapter 5, fig. 5.9).

In order to simulate the occurrence of permanent deformations accompanying soil deformations, observable in the $\gamma < 10^{-3}$ range, author created a preliminary version of the computer application and published (Srokosz et al. 2017). The application is based on the Finite Element Method and has been used for the back analysis of TS test results. Obtaining a full description of the behavior of the tested material under cyclic loading requires reconstructing the full load path, taking into account incremental changes in stiffness. In numerical calculations, the hysteresis phenomenon (Masing's rule, fig. 6.4) is simulated by implementing, in computer applications, special cases of the constitutive laws of non-linear elasticity or elastoplasticity (e.g. Benz 2007, Truty 2008, Cudny, Truty 2020, Puzrin 2012, Puzrin, Burland 1998, Potts, Zdravkovi 1999, Tyrologou et al. 2005). In the literature on the subject, one can find many interesting mathematical and numerical solutions that allow to simulate quite complicated (non-elliptical) shapes of hysteresis loops (e.g. Nogami et al. 2012, Chen et al. 2008, Chen 1975, Chen, Liu 1990, Chen, Saleeb 1994).

In order to carry out numerical calculations related to the back-analysis of the TS test results, the concept of Masing's rule modeling (fig. 6.4) was

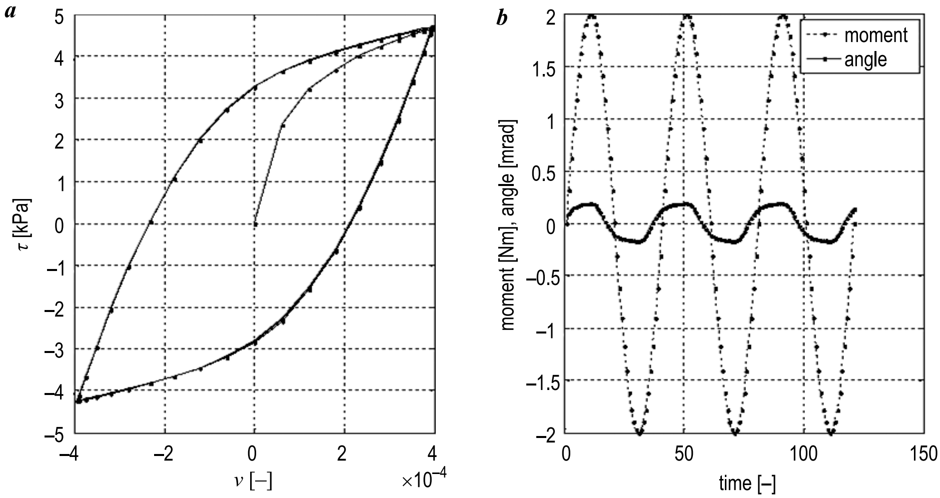

Fig. 6.4. FEM simulation of the hysteresis loop using the law of non-linear elasticity:
a – hysteresis loop, *b* – TS test loading path
Source: after SROKOSZ et al. (2017).

developed, which was programmed in C++ in the form of the TS.exe computer application. This concept vividly described Puzrin in 2012 (PUZRIN 2012). Figure 6.5 shows the internal structure of this program – calculations are performed in the form of sequentially performed procedures and functions (names are marked in italics).

Shearing generation of the numerical representation of the soil sample is carried out by applying the increments of the twist angle of its upper surface (Θ) and the time step (t) according to the formulas:

$$t = \frac{2i\pi}{n} \tag{6.2}$$

$$\Theta^{i+1} = \Theta_{\max} \sin t \tag{6.3}$$

$$\Delta\Theta^{i+1} = \Theta^{i+1} - \Theta^{i} \tag{6.4}$$

where:

t – value of time calculated from the step value i,
n – the number of steps set in the input,
$\Theta^{i,i+1}$ – twist angle respectively: previous (i) and next (i+1),
$\Theta_{\max}$ – the maximum twist angle given in the input data.

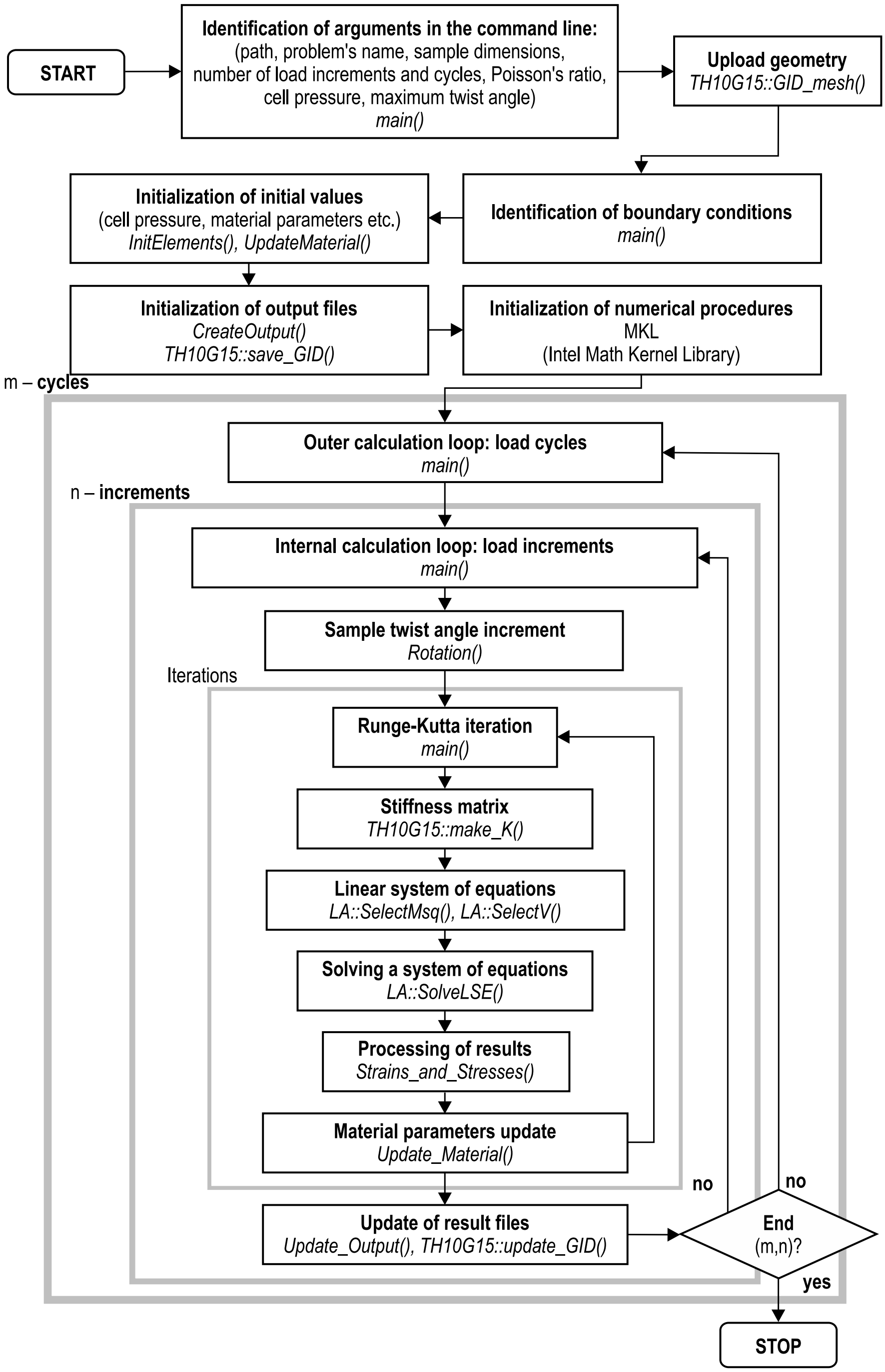

Fig. 6.5. Internal structure of the TS.exe application
Source: after Srokosz et al. (2017).

The phenomenon of stiffness degradation corresponds to a decrease in the value of the Kirchhoff modulus $G(\gamma)$, and consequently Young's modulus $E(G(\gamma),\nu)$ while maintaining a constant value of Poisson's ratio ν. Naturally, assuming a constant value of Poisson's ratio in the calculations is a simplifying assumption, but it is purposeful and necessary to ensure the unambiguity of the solution.

$$E(\gamma) = 2G(\gamma)(1 + \nu) \tag{6.5}$$

Anisotropic changes in the mechanical properties of the sample material, caused by shearing, are simulated by the resultant effect of different stiffnesses at individual Gaussian integration points located in the volume of a given finite element.

The adopted simplification for modeling unevenly degraded stiffness in the volume of the material is fully acceptable, taking into account the aspects of the target use of the obtained calculation results to solve practical problems in geotechnical engineering. In addition, it allows to take into account local changes in stiffness (independently in each element) and to observe the resultant effect throughout the system.

The proposed concept of determining the non-linear relationship $G(\gamma)$ consists in iterative matching of the relationship $\tau(\gamma)$, in the form of a hysteresis loop, obtained from FEM simulation calculations, to the results obtained from TS soil tests. The most commonly used technique is to perform a numerical simulation of the experiment and estimate the quality of the solution based on the adopted objective function, e.g.:

$$L = \sum_{n} w\left(\tau_{\gamma}^{e} - \tau_{\gamma}^{c}\right)^{2} \tag{6.6}$$

where:

τ_{γ}^{e} – measured (experimental) values τ for given values of γ,
τ_{γ}^{c} – determined (calculated) values from the theoretical/numerical model,
w – weights assigned to the analyzed points (computing nodes),
n – number of points (nodes) with the compared values of $\tau(\gamma)$.

The task constructed in this way is a complex problem and it may turn out that it is wrongly posed in the sense of Hadamard, which may directly result in difficulties in obtaining a convergent iterative process. Adaptation of the calculation results to the results of experimental research can be done in stages, limiting the optimization process to find the coordinates of a selected subset of points associated with previously corresponding points in a subset of experimental data. The analysis of successive points and optimization of the local relation $G(\gamma)$ allows to simplify the whole process and significantly improve its convergence. The proposed algorithm is shown in figure 6.6.

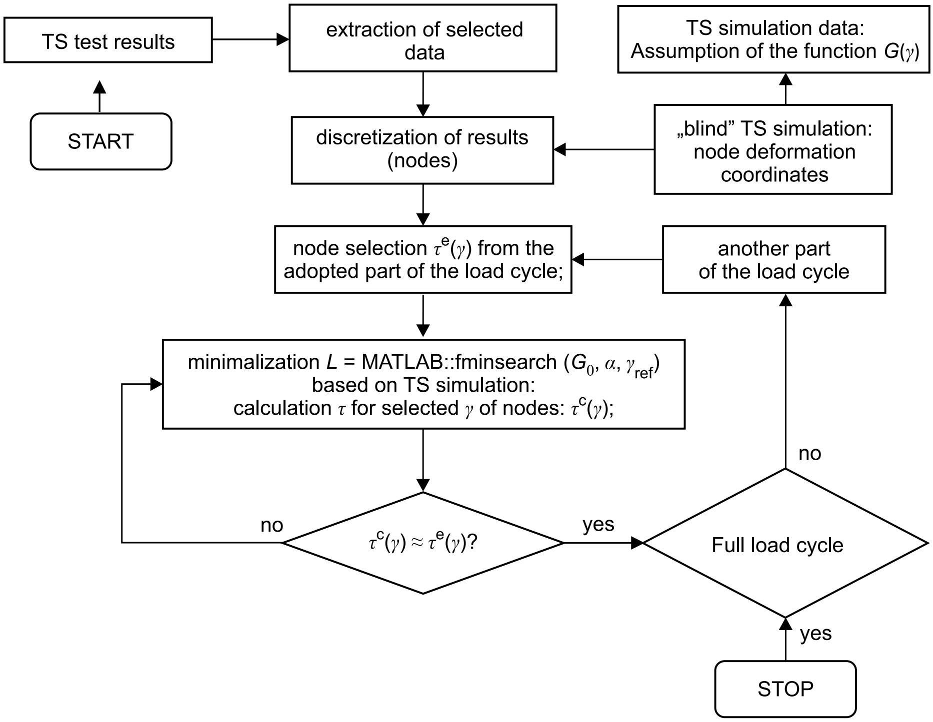

Fig. 6.6. Backanalysis algorithm for searching for the local dependence *G(γ)*
Source: after Srokosz et al. (2017).

The first stage of the algorithm is the discretization of experimental results (i.e. dependencies $\tau(\gamma)$). The points obtained from the discretization process should closely match the calculation points obtained from the numerical simulation of the TS test.

Taking into account the fact that the experimental data are already in the form of a fine-grained set of discrete $\tau(\gamma)$ values (the sampling frequency of the RC/TS apparatus is 100 Hz), the preparation of the set of computational nodes consists in the selection of those points that will be correlated with the calculation results.

Due to the assumption that the values of G depend only on one argument – shear strain γ, the set of selected points $\tau(\gamma)$ was divided into four subsets representing four stages of sample shearing, determined by different signs of strain γ and its increments $\Delta\gamma$ (fig. 6.7):

- primary torque loading: $\gamma_{AB} \in [\gamma_A = 0, \gamma_B = +\gamma_{\max}]$;
- primary unloading and secondary torque loading until $\gamma_C = 0$: $\gamma_{BC} \in [\gamma_B = +\gamma_{\max}, \gamma_C = 0]$;
- continuation of the secondary loading: $\gamma_{CD} \in [\gamma_C = 0, \gamma_D = -\gamma_{\max}]$;
- secondary unloading and torque loading starting the second cycle until $\gamma_E = 0$: $\gamma_{DE} \in [\gamma_D = -\gamma_{\max}, \gamma_E = 0]$.

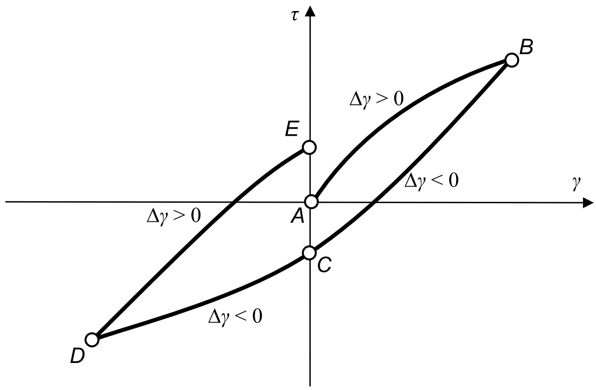

Fig. 6.7. Division of the shearing cycle of the sample material into four phases
Source: after SROKOSZ et al. (2017).

The degradation of stiffness in the separated, four stages of loading is described by independent functions $G(\gamma)$. These relations can be obtained in the form of an explicit relation assuming the general form of the function $G(\gamma)$ (NOGAMI et al. 2012):

$$G(\gamma) = G_0 \Gamma(\gamma, \alpha, \gamma_{\text{ref}}) \tag{6.7}$$

$$\Gamma(\gamma, \alpha, \gamma_{\text{ref}}) = \frac{1-\alpha}{1+\frac{\gamma}{\gamma_{\text{ref}}}} + \alpha \tag{6.8}$$

where:

G_0 – maximum value of G modulus,
γ_{ref} – reference value of shear strain,
α – a constant that can be interpreted as:

$$\alpha = \frac{G_{\min}}{G_0} \tag{6.9}$$

where:

$G_{\min}$ – the minimum value of G modulus corresponding to $G(\gamma = +\infty)$.

Assuming the variability of the shear modulus value according to formulas (6.7) and (6.8), three basic parameters were defined: G_0, α, γ_{ref}, which determine the variability of $G(\gamma)$.

In the process of minimizing the objective function, a gradient-free optimization method was used, belonging to the group of direct search methods – the Nelder-Mead algorithm (Nelder, Mead 1965). The algorithm consists in the sequential generation of simplexes defined by n+1 vertices in the case of n-argument optimization of the objective function.

In numerical analyzes using FEM, sample models were discretized using tetrahedral elements with ten nodes and fifteen Gaussian points (TH10G15, fig. 6.8). The assumed number of 980 nodes and 527 elements in numerical simulations (fig. 6.9) is not a critical value – the numerical application used in backanalyses is not sensitive to the resolution of discretization (Srokosz et al. 2017). The adopted number of 80 degrees of load (corresponding to 20 calculation points in each stage of sample shearing) is the minimum value ensuring faithful reproduction of the shape of the hysteresis loop obtained experimentally. Figure 6.9*c* shows the distribution of horizontal displacements in the maximum twist angle phase. Figure 6.9*d* shows the distribution of the γ_{xz} component of shear strains in the same test phase.

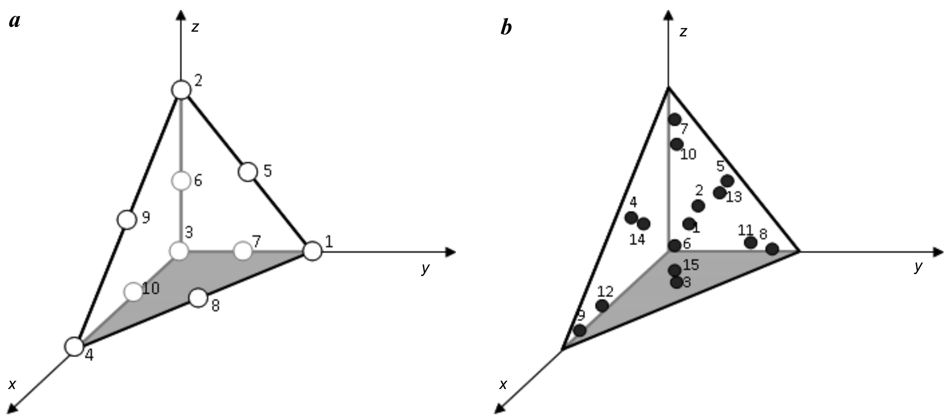

Fig. 6.8. TH10G15 element: *a* – nodes, *b* – Gauss points
Source: after Srokosz (2020).

This distribution is disproportionate to the distribution of displacements. The differences result from the variability of the shear modulus G, which was taken into account calculating the strain values.

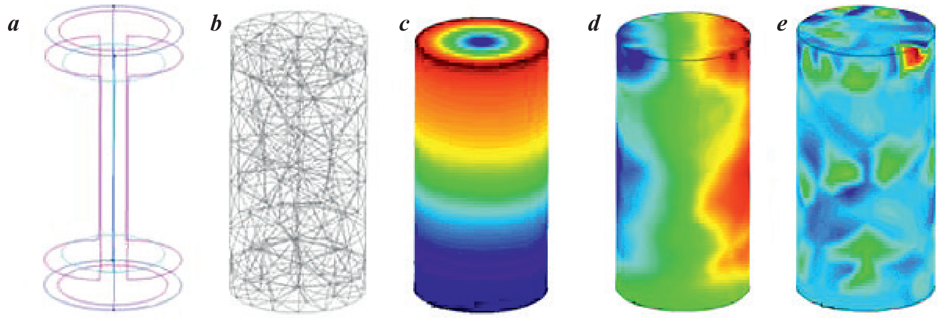

Fig. 6.9. FEM simulation of a torsional shear test: *a* – sample topology, *b* – mesh of elements, *c* – displacements, *d* – deformations, e) change in stiffness
Source: after Srokosz et al. (2017).

In order to map the results of laboratory tests with the results of simulations carried out with the FEM application, it was necessary to use step changes in the stiffness parameters of the tested sample with each change of the load direction (fig. 6.10). On the basis of author's own experiments and analyses, it was noticed that the hysteresis loop did not close properly and that each change in the load direction in subsequent cycles caused a step change in the soil stiffness, visible in the form of step changes in the value of the initial modulus G (fig. 6.10, see also fig. 4.1). Example results of the back analysis of laboratory TS tests, carried out with FEM simulations, are shown in figure 6.10.

Presented method was created for the interpretation of TS test results in the range of strain corresponding to the limit resolution of displacement sensors, i.e. in conditions of highly noisy test results. This method was not directly used to analyze the results in the further part of the work because it was based on the assumption that the soil reacts as a viscoelastic material. The author decided to modernize the measurement system in terms of e.g. implementation of new sensors, which allowed him to detect permanent deformations and confirm that the soil material exhibits the properties of a viscoelastic material.

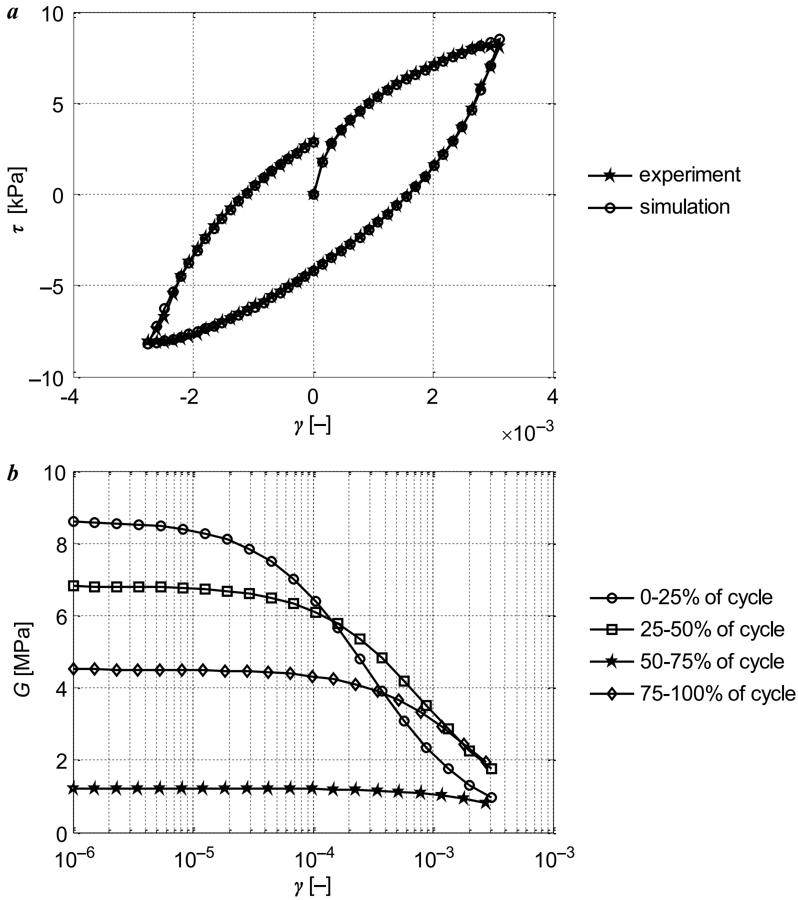

Fig. 6.10. Simulation results of the TS3057 experiment on a sample of semi solid silt: a – visualization of the fit of the $\tau(\gamma)$ function, b – the result functions $G(\gamma)$
Source: after Srokosz et al. (2017).

6.2. Prototype TS test system modification

6.2.1. Sensors

Structure of RC/TS WF8500 apparatus allows for implementation author's modifications (Bae, Bay 2009). An example is the attachment of an electromagnetic rotor that generates a torque. The rotor is encased in an aluminum frame, the base of which are two parallel rings. The bottom ring allows the rotor to be attached to the inner cylinder. The upper ring, which is the outer part of the topcap, is provided with many sockets and passages, which are partially used for the installation of the remaining elements of the device: proximity sensors, LVDT, sensor positioning motors and others (see fig. 6.11). Unused sockets allow the installation of additional measuring components. This creates an opportunity to extend the functionality of the existing equipment with new possibilities resulting from the new equipment. It is possible to install e.g. additional sensors without radical modifications, using only the original construction of the RC/TS apparatus.

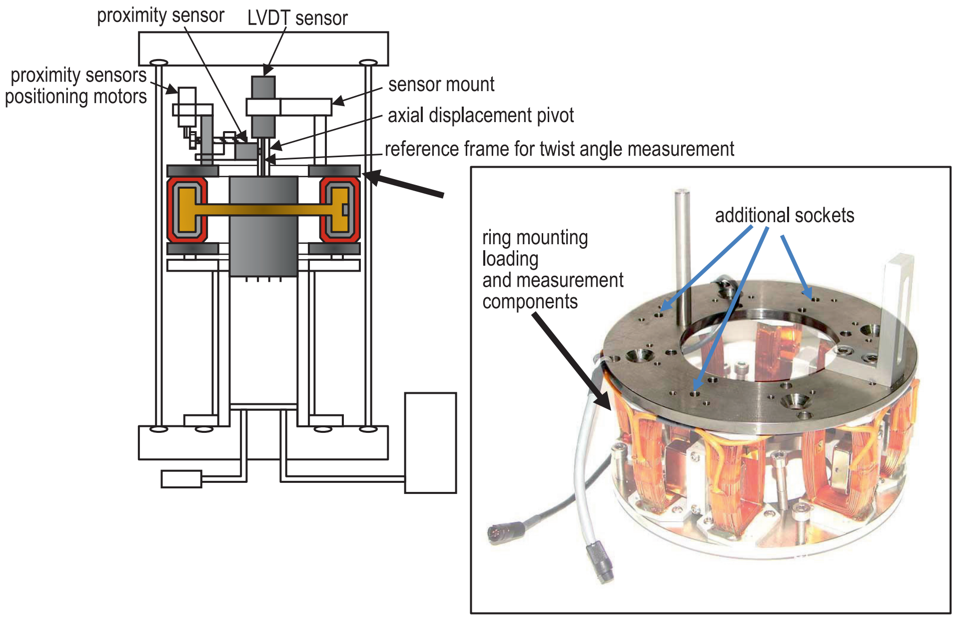

Fig. 6. 11. Rotor of the RC/TS WF8500 apparatus with detailing of the upper ring of the topcap and additional slots that allow the installation of author's modifications to the device

The hardware modification consists in the implementation of improvements in the construction of the RC/TS apparatus with the use of new types of sensors.

Modification 1. A micro-displacement transducer was attached to the outside of the topcap to more accurately measure the twist angle of the top surface of the sample base. The new measurement system included: a microcontroller, an integrated signal amplifier and an analog-to-digital converter, a Wheatstone bridge consisting of 3 precision resistors and 1 electro-resistance strain gauge installed on a steel cantilever plate (fig. 6.12).

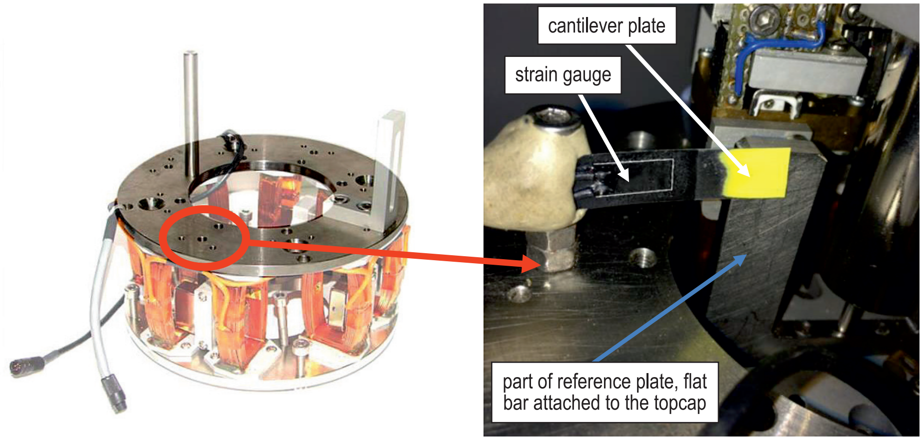

Fig. 6.12. Prototype of a micro-displacement sensor with a cantilever plate (element with a yellow tip)
Source: after BUJKO (2018).

The idea of the measurement is to precisely record the deflection of the cantilever plate caused by the twisting of the apparatus rotor (the topcap mounted on the sample).

Modification 2. The modification of the equipment also included the use of a micro-displacement transducer, consisting of one neodymium magnet between two Hall sensors (fig. 6.13). The movement of the magnet during the test causes a differential change in the magnetic field strength in which

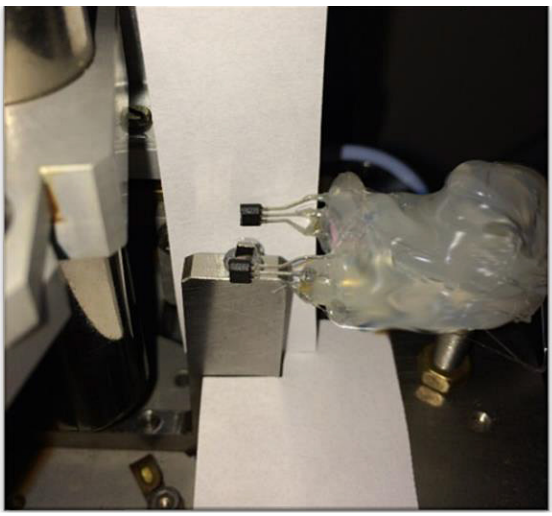

Fig. 6.13. Prototype of the Hall-type microdisplacement sensor
Source: after BUJKO (2018).

the sensors are located. This causes a differential change in the electrical voltage. Change is recorded by the data acquisition system, which converts the changes in voltage into changes in the twist angle.

6.2.2. Data acquisition system

The prototype of the data acquisition system consists of an operational amplifier integrated with a 24-bit analog-to-digital converter and a Wheatstone bridge supply voltage conditioner, AVR microcontroller and USB interface (fig. 6.14). The new data acquisition system is managed by a author's computer application, which operates in real-time testing, in parallel and independently of the standard RC/TS software.

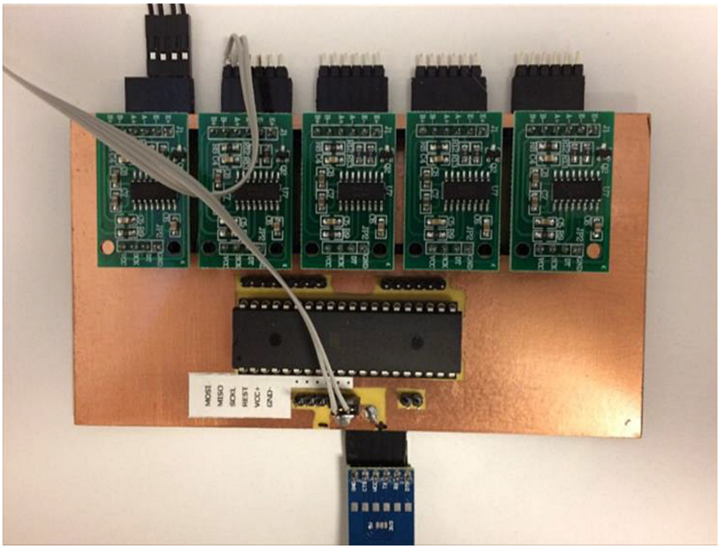

Fig. 6.14. Prototype of the data acquisition system

Each test begins with the calibration of new sensors and their synchronization with proximity sensors, which are the original equipment of the RC/TS WF8500. Figure 6.15 shows an example of the effects of synchronization of strain gauges (modification 1) and proximity sensors. As you can see, the readings from the sensors are in phase and amplitude, which allows to carry out tests with extended time of displacement registration

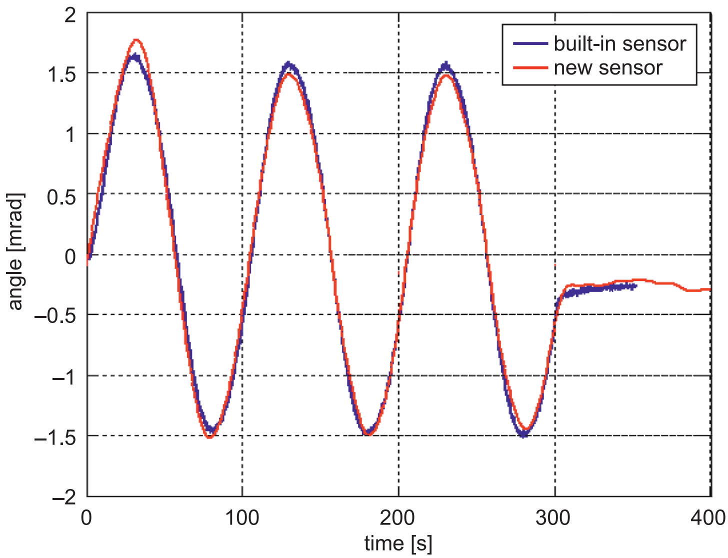

Fig. 6.15. Example of synchronization of a new strain gauge sensor (red line) with the original proximity sensors (blue line) of the RC/TS WF8500 apparatus

(measurement extrapolation). This enables a qualitative assessment of the occurrence of permanent deformations after the completion of the process of loading the tested soil.

TS tests with the use of an additional measuring system were repeated many times for different load programs. Exemplary, preliminary results of tests carried out on high-plasticity silty clay are shown in figure 6.16 (three cycles with an amplitude of 3 V and a frequency of 0.01 Hz). After unloading the sample and completing the recording by the original application of the apparatus (Dynator.exe), i.e. after 400 seconds, the measurement was continued using the new measurement system. During the next 16,000 seconds, a slight decrease in the absolute value of the sample twist angle was recorded. However, this angle stabilized at the level of strain that is different from the initial level, clearly indicating the appearance of permanent deformations.

Initial measurement showed that after unloading, the soil material does not return to the original state of deformation. However, the level of interference accompanying the measurements raises numerous ambiguities – the self-noise range of the measuring system is close to the value of the recorded permanent strain. It was necessary to further improve the adopted measurement method.

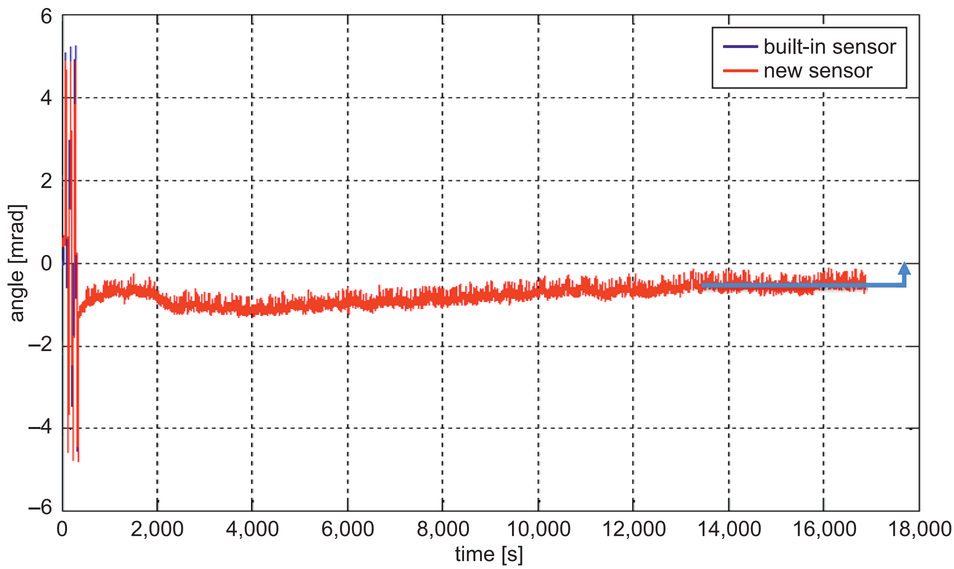

Fig. 6.16. Exemplary results of angle twist measurement after unloading a plastic silty clay sample

6.3. Final TS test system modification

The improvement of the adopted measurement method meant the use of a different design solution for the measuring sensors and the data acquisition system itself.

Modification 3. Hall sensors with an alternative design were used (fig. 6.17), allowing for a linear response to the twist angle of the device's topcap. The improved sensor system is based on the same operating principle as the prototype version fig. 6.13). The movement of the Hall sensor relative to the stationary magnet during the test causes a linear change in the magnetic field strength, which causes a proportional change in the electric voltage at the sensor output. This change is recorded by the modernized data acquisition system,which converts voltage changes into changes in the twist angle.

The standard control software of the RC/TS WF8500 allows the sample to be subjected to a harmonic torque and acquisition of basic load path data, i.e. number of cycles, amplitude and load frequency. However, Programming any load path is impossible. Therefore, it was decided to modernize the system of data acquisition and control.

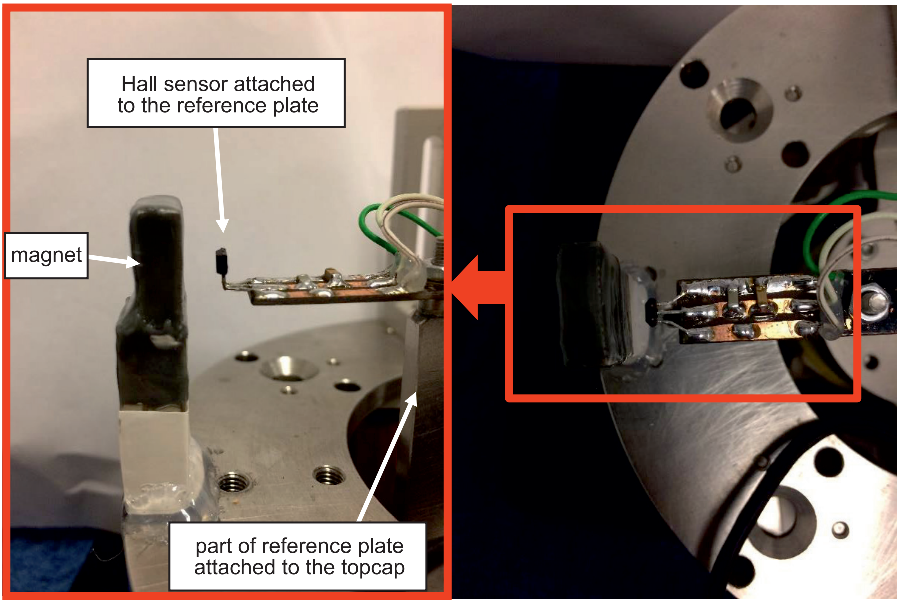

Fig. 6.17. Hall sensors – final version

Modification 4. Significant modification has been implemented to the new aquisition system. It enables setting complex load paths, maintaining the original functionality of the device.

Any load path developed in MATLAB is uploaded about a author's computer application that connects continuously via the USB interface with the controller that controls the coils of the RC/TS apparatus (fig. 6.18 and 6.19). At the same time, the magnetic field strength is measured with Hall sensors with increased accuracy (version 2 – fig. 6.17).

Supplementary tests were carried out to identify permanent deformations under specific load conditions.

The final version of the device control system (fig. 6.21) differs from the prototype version (fig. 6.20) in the sensors used. The disadvantage of sensors Hall is the sensitivity to changes in the external magnetic field. An advantage of it is non-contact, small size and weight, and high accuracy. The high quality of the measurement results obtained is not only related to the application Hall sensors. Application of analog-to-digital converters (ADC CS5532 18 bit) with higher resolution enabled the use of more effective noise reduction algorithms. Use of a higher quality DAC provides precise control of the rotor of the device.

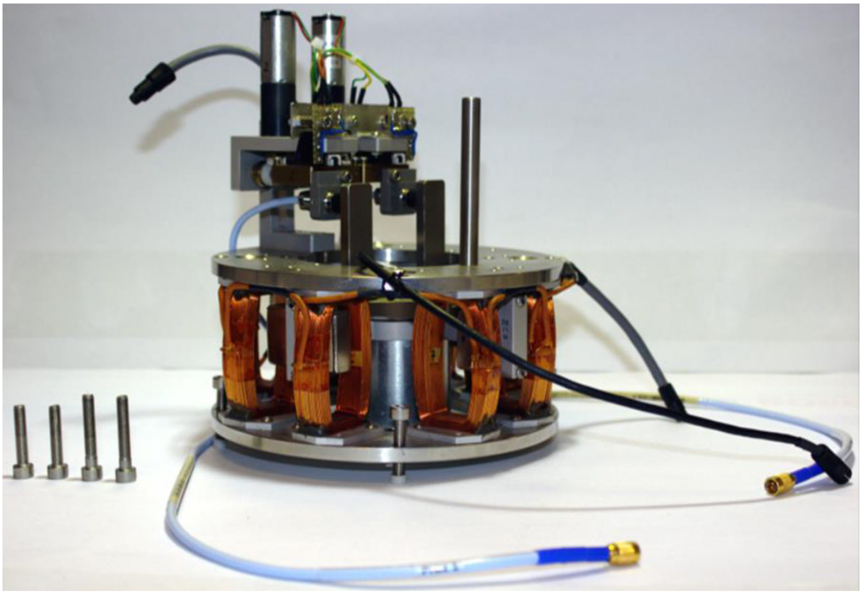

Fig. 6.18. Rotor generating a torsional load on a soil sample

Fig. 6.19. The central unit of the new device control system

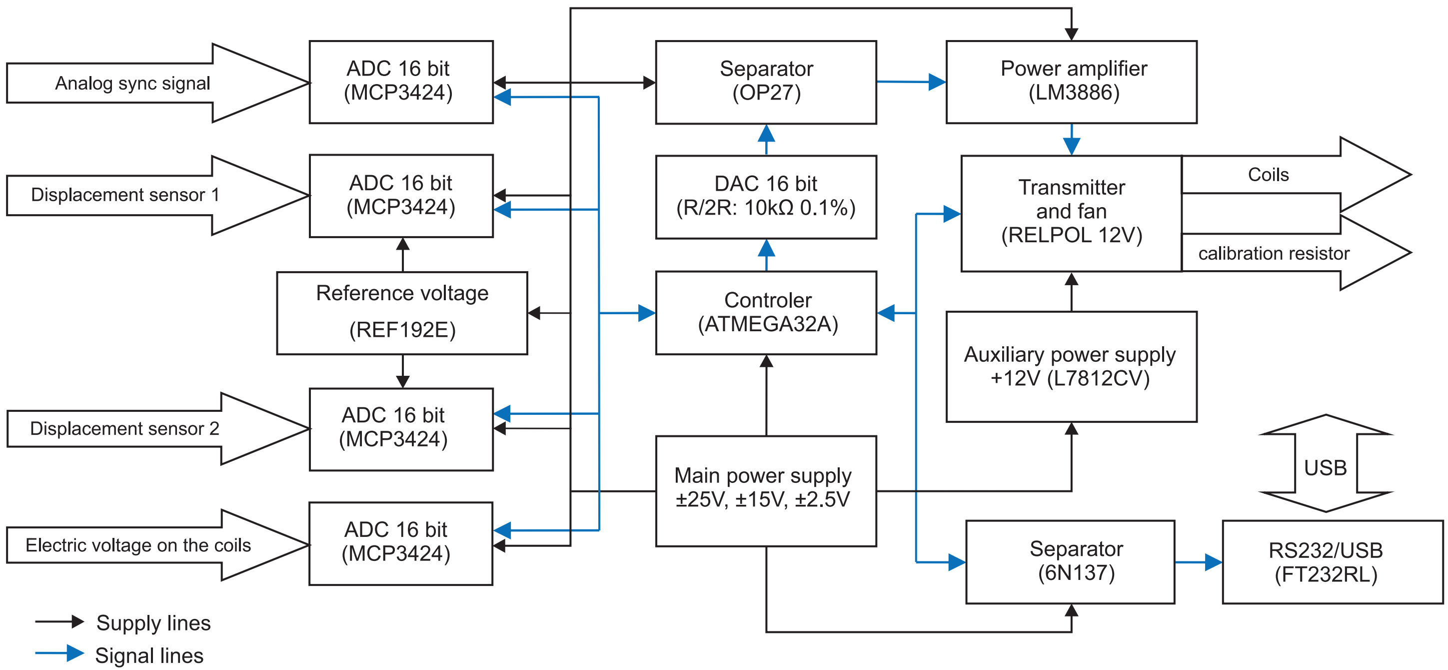

Fig. 6.20. Scheme of the data aquisition system – prototype version

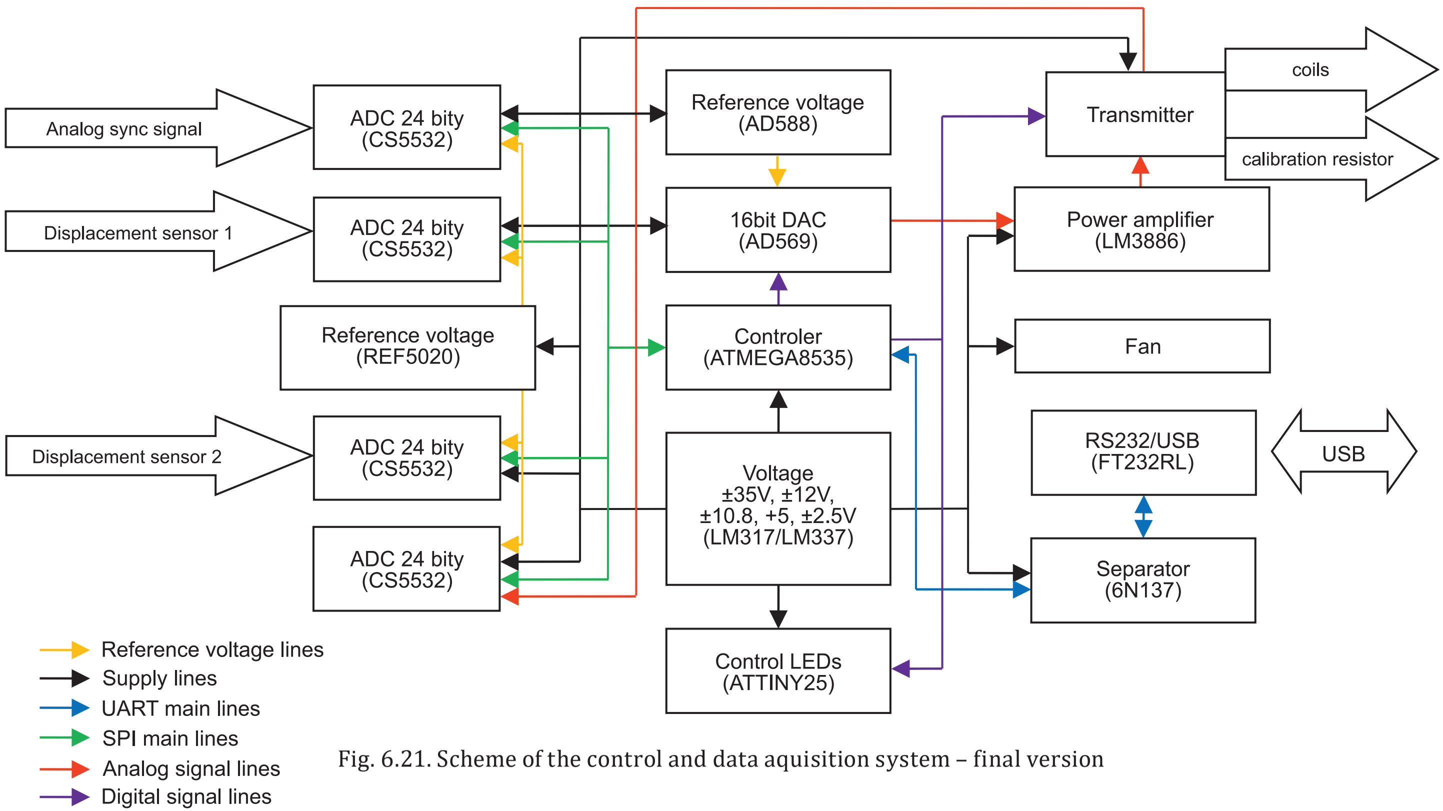

Fig. 6.21. Scheme of the control and data aquisition system – final version

Figure 6.22 shows the results of the self-noise analysis of the PT and Hall sensors in the form of graphs of measured strain over time and deviation σ values for both signals measured in relation to the trend line.

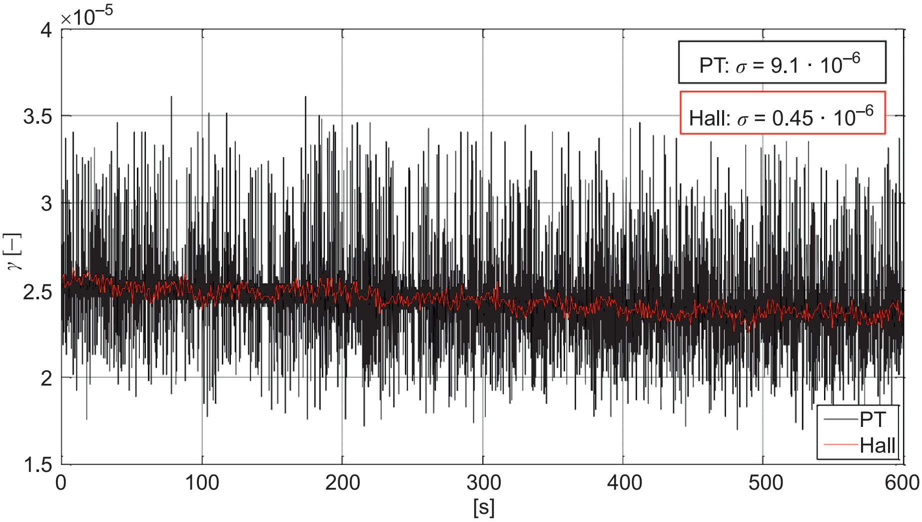

Fig. 6.22. Comparison of sensors' own noise levels
(σ – standard deviation)

Chapter 7

Observation of permanent soil deformation

7.1. Research material

Wichtmann's habilitation thesis justifies the choice of research material (Wichtmann 2016), who performed about 650 RC tests with an additional measurement of the pressure wave propagation velocity (P-wave) on non--cohesive soils with 65 different grain size curves. For the purposes of research works, 5 of them were recreated. Each grain size distribution curve is characterized by a different uniformity coefficient C_U. In the geotechnical laboratory in Olsztyn, selected research material has been already tested for many purposes. First publications appeared in 2017 and concerned the impact of the grain size distribution curve on soil stiffness (Dyka et al. 2017).

The geometrical and physical parameters of the tested non-cohesive soils are summarized in table 7.1: G_S – specific gravity, d_{50}, d_{60}, d_{10} – values of the particle diameter at 50%, 60% and 10% in the cumulative distribution, C_U – uniformity coefficient, $e_{\max}$ – maximum void ratio, $e_{\min}$ – minimum void ratio, ρ – bulk density. Grain size distributions and micrographs of sand samples are shown in figures 7.1-7.5.

Tab. 7.1. Geometrical and physical parameters of the tested non-cohesive soils

Sand	G_s [-]	d_{50} [mm]	d_{60} [mm]	d_{10} [mm]	C_U [-]	$e_{\max}$ [-]	$e_{\min}$ [-]	ρ [g/cm^3]
P1	2.65	0.33	0.35	0.22	1.6	0,55	0,39	1.76
P2	2.65	0.33	0.41	0.14	3.0	0,68	0,41	1.86
P3	2.65	0.33	0.48	0.12	4.0	0,60	0,37	1.93
P4	2.65	0.60	0.65	0.32	2.0	0,57	0,38	1.76
P5	2.65	0.60	0.80	0.20	4.0	0,70	0,41	1.94

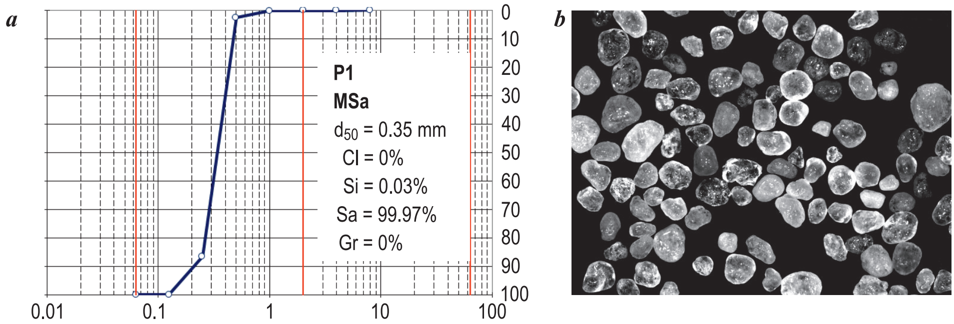

Fig. 7.1. Sand P1; tested material: *a* – grain size distribution,
b – microscopic image of tested sand's grains
Source: after DYKA et al. (2017).

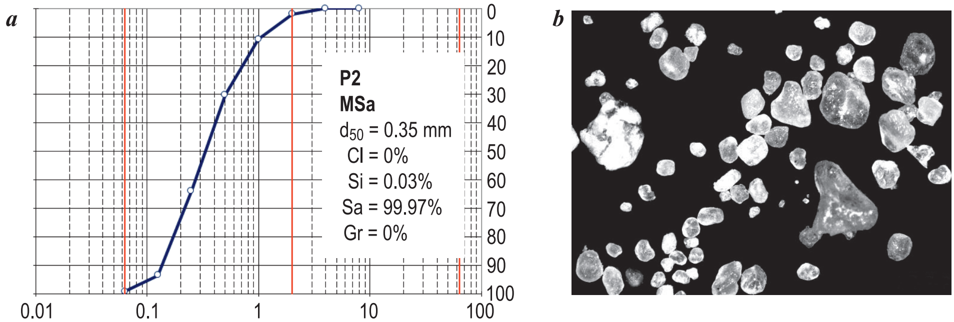

Fig. 7.2. Sand P2; tested material: *a* – grain size distribution,
b – microscopic image of tested sand's grains
Source: after DYKA et al. (2017).

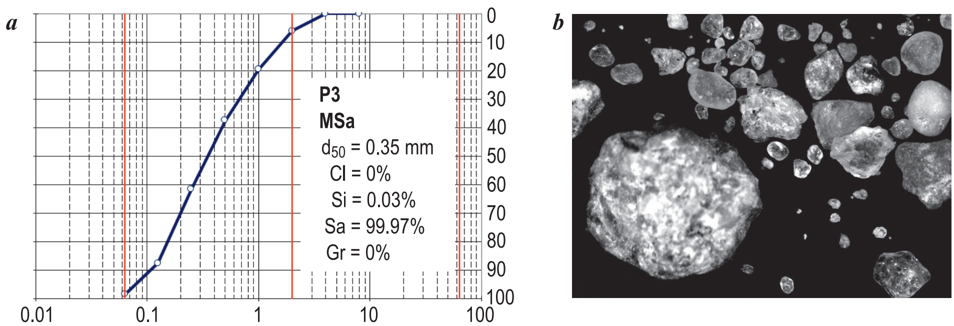

Fig. 7.3. Sand P3; tested material: *a* – grain size distribution,
b – microscopic image of tested sand's grains
Source: after DYKA et al. (2017).

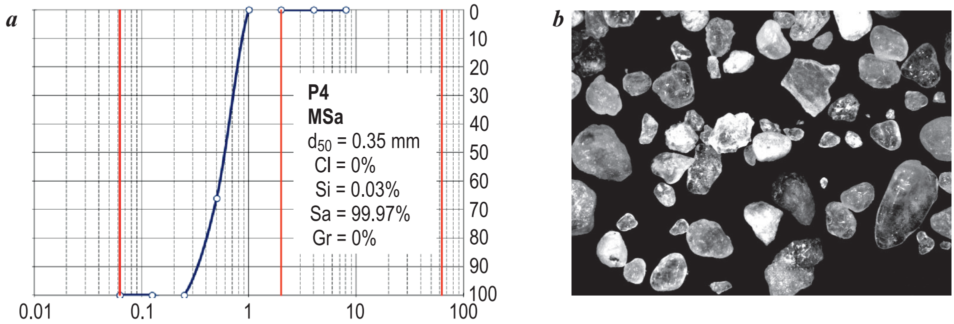

Fig. 7.4. Sand P4; tested material: *a* – grain size distribution,
b – microscopic image of tested sand's grains
Source: after DYKA et al. (2017).

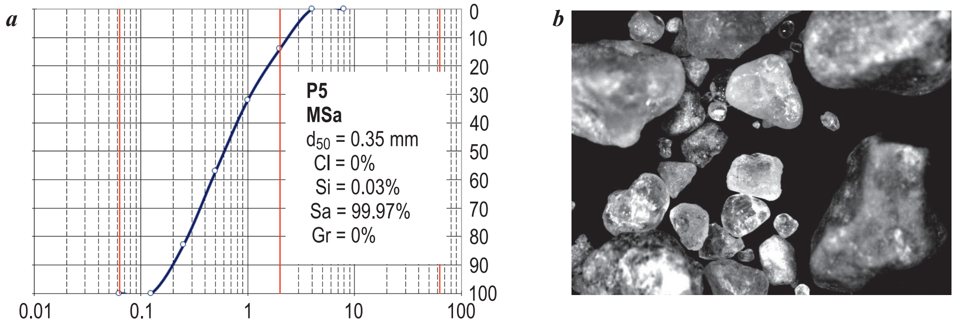

Fig. 7.5. Sand P5; tested material: *a* – grain size distribution,
b – microscopic image of tested sand's grains
Source: after DYKA et al. (2017).

Each of the sand samples with grain size distribution curves P1-P5 was prepared from previously selected soil fractions with grain diameters of 0.063–10 mm. A cylinder-shaped sample (dimensions: base diameter d=70 mm, height H=140 mm) was formed using a template with a latex membrane installed in it. The maximum dry density and the optimum moisture content of the sand were determined through the Standard Proctor Compaction Test. The specimens were prepared with the optimum moisture content (3.0–4.0%).

After each sample was installed in the RC/TS apparatus, the soil was subjected to isotropic pressure for one hour, followed by a TS test. The tests were carried out with designed, non-standard load paths (fig. 7.6), which were programmed using the author's control system of the device (fig. 6.19 and 6.21).

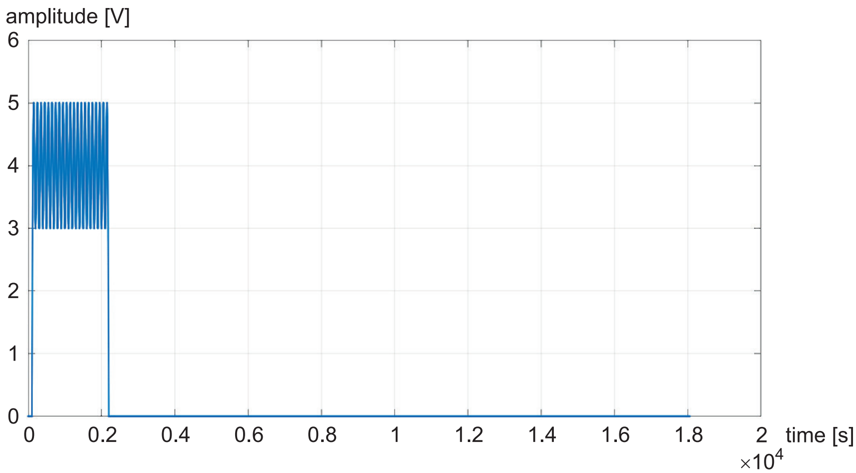

Fig. 7.6. Designed CS20 load path

7.2. Custom load paths

7.2.1. CS20 load path

TS tests with the use of an additional measuring system (modification 3 and 4 – fig. 6.17 and 6.21) were carried out on all types of sand (see tab. 7.1) at various loads. The specific control of the RC/TS device consists in setting the load amplitude with the electric voltage applied to the stator coils. Each load path begins with a 100 second downtime to stabilize reading control from the sensors followed by loading of the sample. The adopted load and recording times result from preliminary studies using prototypes of displacement sensors (strain gauges and Hall sensors – modifications 1 and 2, fig. 6.12 and 6.13). The modernization of the TS research supervision system enables experiments to be carried out in conditions of freely shaped load paths, which are programmed in the MATLAB software environment. This work presents two author's suggestions for such paths, which are codenamed CS20 and SQ. For each soil, tests were carried out with the following load paths.

The CS20 load path (fig. 7.6) was designed to observe the soil deformation that occur under cyclic torsional harmonic loading. The load can simulate the operating conditions of the subsoil, which is repeatedly loaded and unloaded. This applies, for example, to offshore wind farms subjected to cyclical loads from sea waves (Srokosz et al. 2018a). The path consists of 20 cycles with an electrical voltage amplitude of 1 V inside a harmonic excitation with an amplitude of 4 V. The period of loading the sample lasts 2,100 seconds and after unloading the strain recording is continued and lasts 18,000 seconds.

After unloading the sample and completing the deformation recording with standard proximity transducers (original equipment of the apparatus), i.e. after 2,200 seconds, the measurement with new Hall sensors was continued for 18,129 seconds (over 5 hours). The results carried out on the P1, P2, P3, P4 and P5 soils are presented below.

The results of the torsional shear test using the designed CS20 load path indicate the accumulation of permanent deformation of the soil sample and the increase of shear strain in each subsequent load cycle. Despite the constant amplitude of the CS20 load path, there are differences between the first and last value of the maximum strain $\Delta\gamma_{max}$ (see fig. 7.7). The soil becomes plastic during the test, as evidenced by the values of shear strain in the residual phase γ_{res} and non-closing hysteresis loops. Within the hysteresis loops shown in figure 7.8, each successive cycle characterizes a narrower range of γ values.

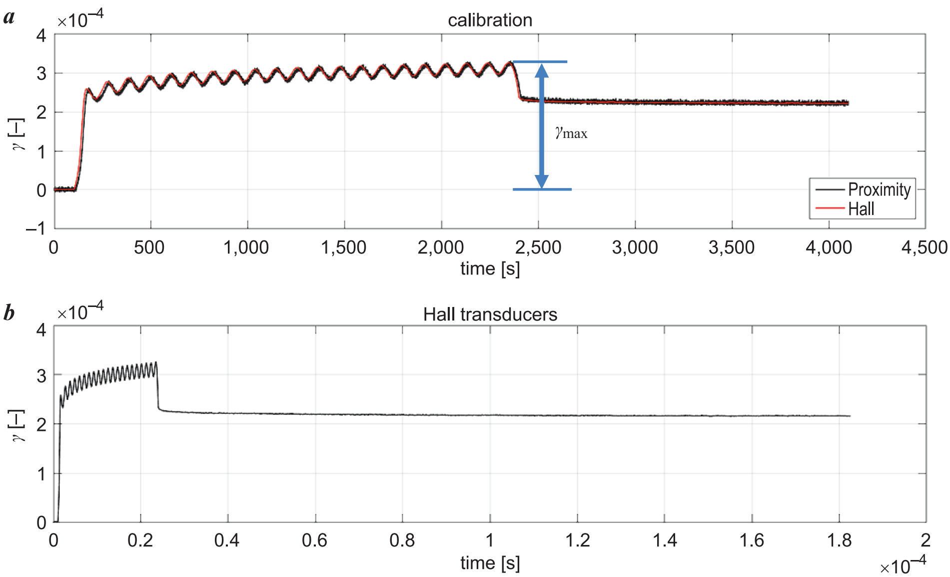

Fig. 7.7. P1 soil TS test results, *a* – calibration of proximity and Hall sensors, *b* – measurement of shear strain with Hall sensors, with extended recording time after unloading the sample – CS20 path

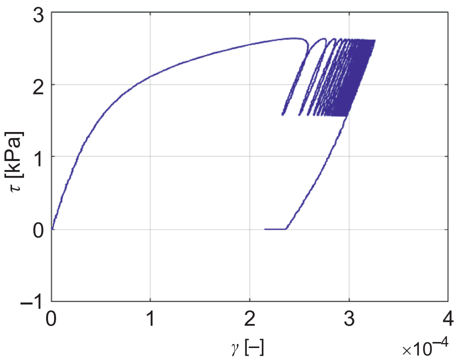

Fig. 7.8. P1 soil TS test results, hysteresis loop – CS20 path

P1 soil

Among all the results of the tests carried out using the CS20 load path, the highest value of maximum strain γ_{max}=3.3·10^{-4} was recorded during TS tests on a P1 soil sample (fig. 7.7, 7.8).

P2 soil

During the TS tests on the soil sample P2 (fig. 7.9, 7.10), the highest value of permanent shear strain was recorded in the residual phase of the CS20 load path γ_{res}=0.45·10^{-4} .

P3 soil

Particular attention should be paid to the significant noise level of standard proximity transducers, which is close to the level of permanent deformation γ_{res}, recorded during the same test (fig. 7.11 and 7.12). This is the effect of scaling the values in the graphs and analyzing test results, where lower values of the maximum shear strain γ_{max} were obtained. This is particularly visible analyzing the results of P4 soil tests (compare fig. 7.13 or 7.15 with fig. 7.7 and 7.14 with fig. 7.8). This is related to a relatively high measurement inaccuracy, which justifies the parallel use of hall sensors (modification 3 – fig. 6.17).

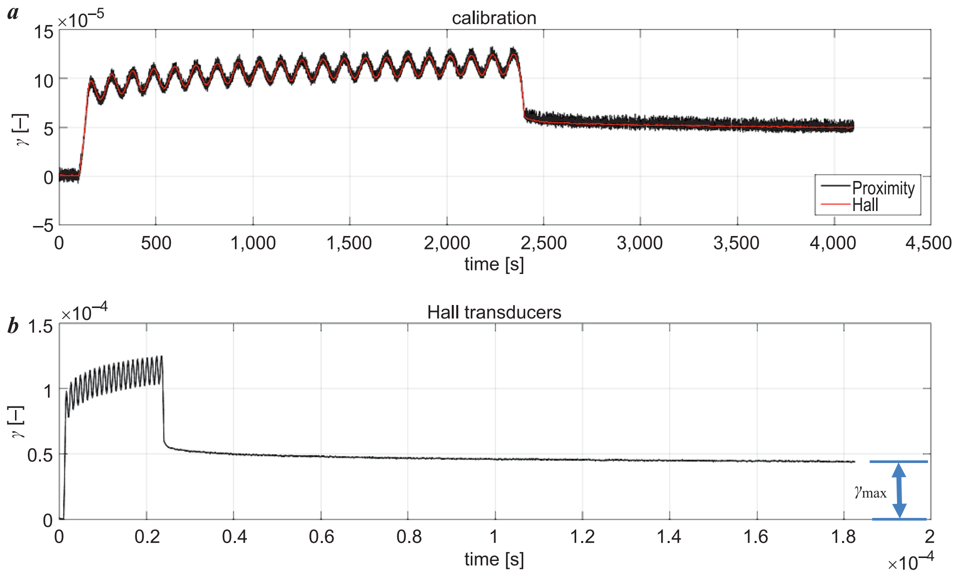

Fig. 7.9. P2 soil TS test results, *a* – calibration of proximity and Hall sensors, *b* – measurement of shear strain with Hall sensors, with extended recording time after unloading the sample – CS20 path

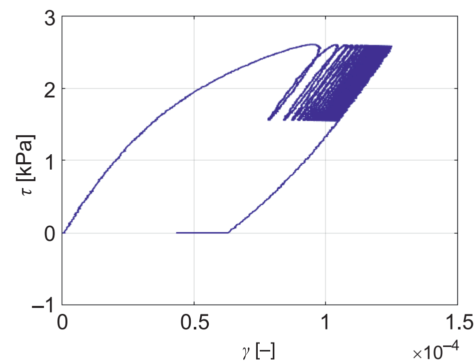

Fig. 7.10. P2 soil TS test results, hysteresis loop – CS20 path

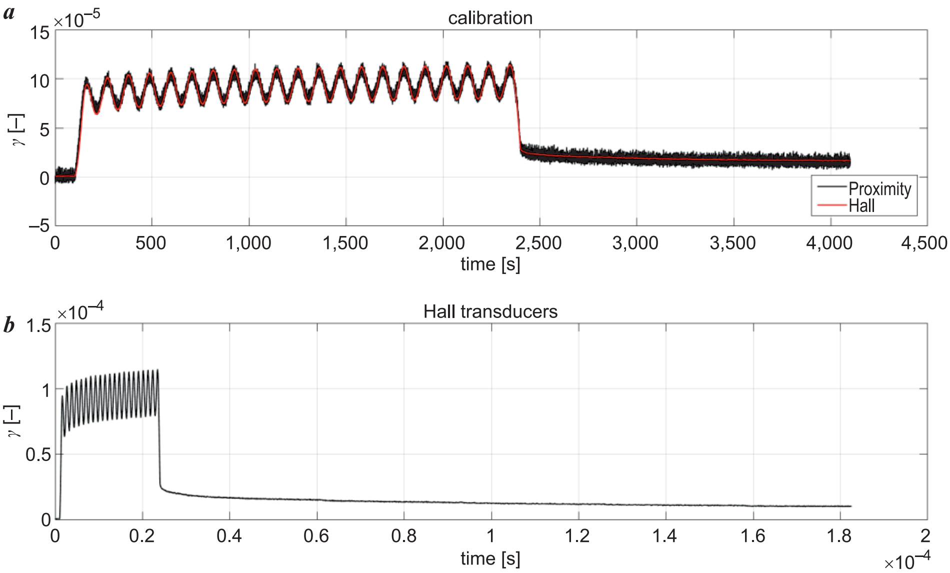

Fig. 7.11. P3 soil TS test results, *a* – calibration of proximity and Hall sensors, *b* – measurement of shear strain with Hall sensors, with extended recording time after unloading the sample – CS20 path

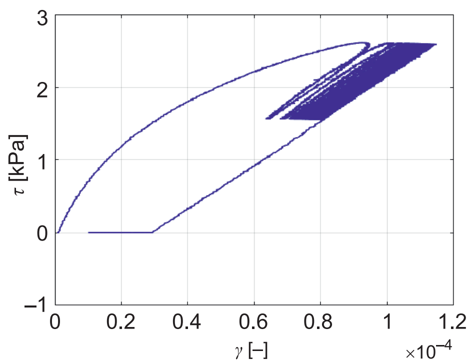

Fig. 7.12. P3 soil TS test results, hysteresis loop – CS20 path

P4 soil

Among the tests with the CS20 load path, the smallest values of maximum shear strain γ_{max}≈0,69·10^{-4} were recorded during tests of the P4 soil (fig. 7.13, 7.14).

This example shows how noticeable might be disproportion in the level of the recorded strain values in comparison with parameters of the the custom load path. The ratio of the recorded strain amplitude values of 20 internal cycles to the recorded values of first cycle is significantly bigger from the corresponding proportion in the designed CS20 load path.

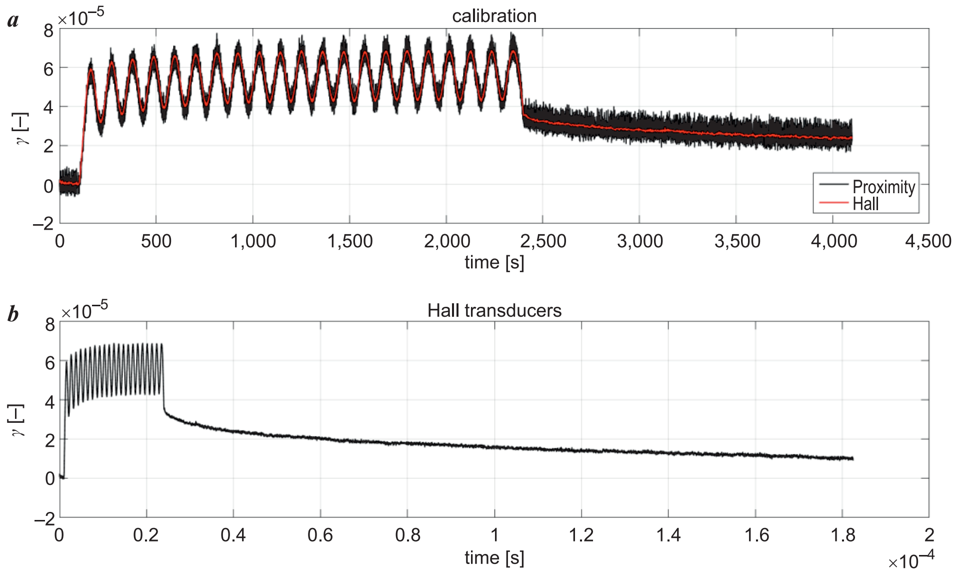

Fig. 7.13. P4 soil TS test results, *a* – calibration of proximity and Hall sensors, *b* – measurement of shear strain with Hall sensors, with extended recording time after unloading the sample – CS20 path

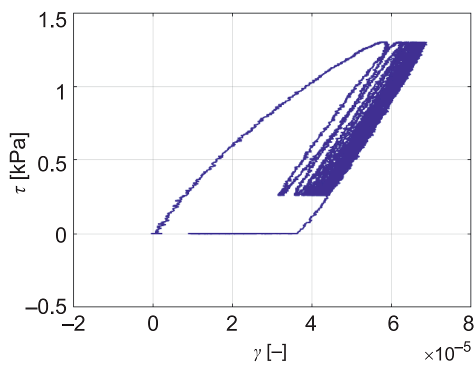

Fig. 7.14. P4 soil TS test results, hysteresis loop – CS20 path

P5 soil

The tests carried out on the P5 soil show that the stabilization time T’ of the residual strain values γ_{res} may be different depending on the applied load path.

After unloading the sample with a load in accordance with the CS20 path, non-zero values of shear strain were recorded (fig. 7.15). The strain measurement was continued for 4.5 hours. After this time, the residual strain value decreased by $\Delta\gamma_{res}=0.5\cdot10^{-5}$ to the value of $\gamma_{res}=1.2\cdot10^{-5}$.

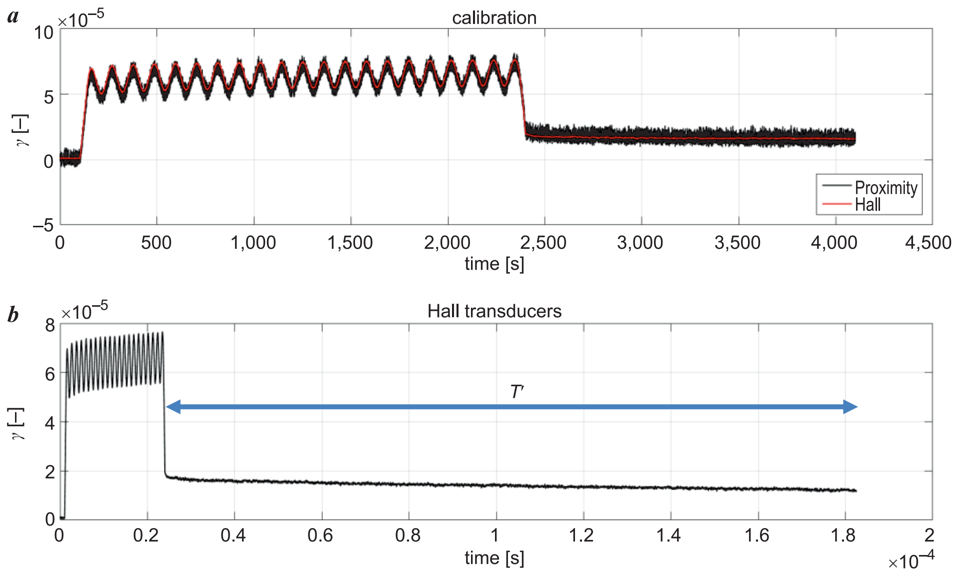

Fig. 7.15. P5 soil TS test results, *a* – calibration of proximity and Hall sensors, *b* – measurement of shear strain with Hall sensors, with extended recording time after unloading the sample – path CS20

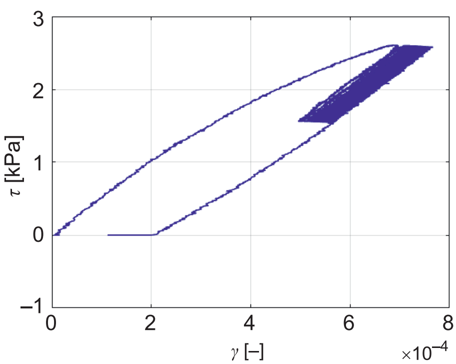

Fig. 7.16. P5 soil TS test results, hysteresis loop – CS20 path

In case of testing using the SQ path (fig. 7.16), after 3 hours and 50 minutes, the value of residual strain reached a stable value $\gamma_{res}=0.30\cdot10^{-5}$. The measurement of deformation was continued for 40 minutes, but no further change in the value of shear strain was noted.

7.2.2. SQ load path

The SQ load path (fig. 7.17) was designed to record shear deformations during an unusual, single cycle of torsional loading and unloading at an extended time of maximum load. It should be noted that, in accordance with the designed path, the load is not cyclical. This means that the modernization of the device's control system enables simulating the subsoil load condtitions in any form. The SQ path is characterized by stabilizing the amplitude of the torsional load at the level of 5 V for a period of 2,000 seconds. A full cycle of sample loading lasts 2,100 seconds and after unloading, the deformation recording is continued and lasts 18,000 seconds.

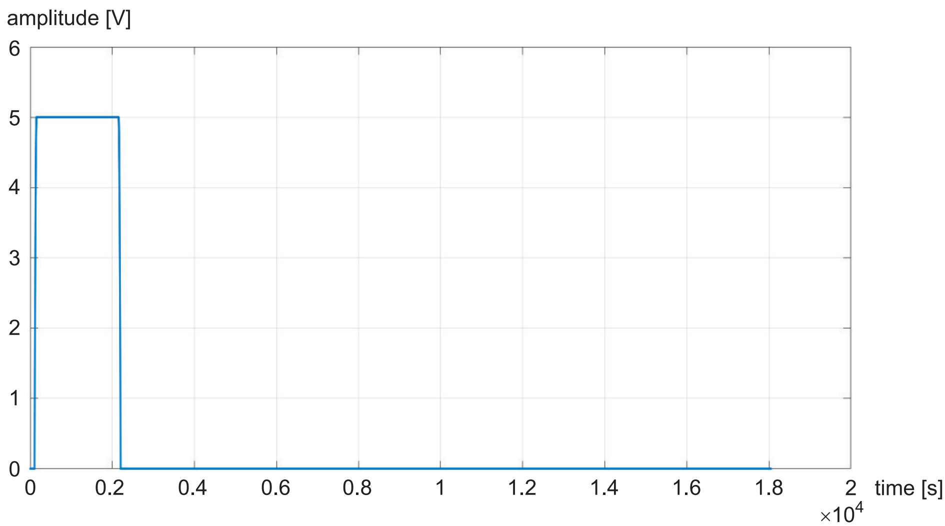

Fig. 7.17. Designed SQ load path

The results of the TS tests using the SQ load path are presented below. According to SQ load path, amplitude of load is constant. In spite of this fact, the measurement results indicate successively increasing values of shear strain. Hence, as in the case of the CS20 path, there are visible differences between the first and last values of the maximum strains $\Delta\gamma_{max}$ (fig. 7.18). The modified test supervision method allowed to record the phenomenon of soil plasticization during the test. Again, this is evidenced by the measured difference in shear strain in the residual phase γ_{res} and the unclosed form of the hysteresis loop (fig. 7.19).

P1 soil

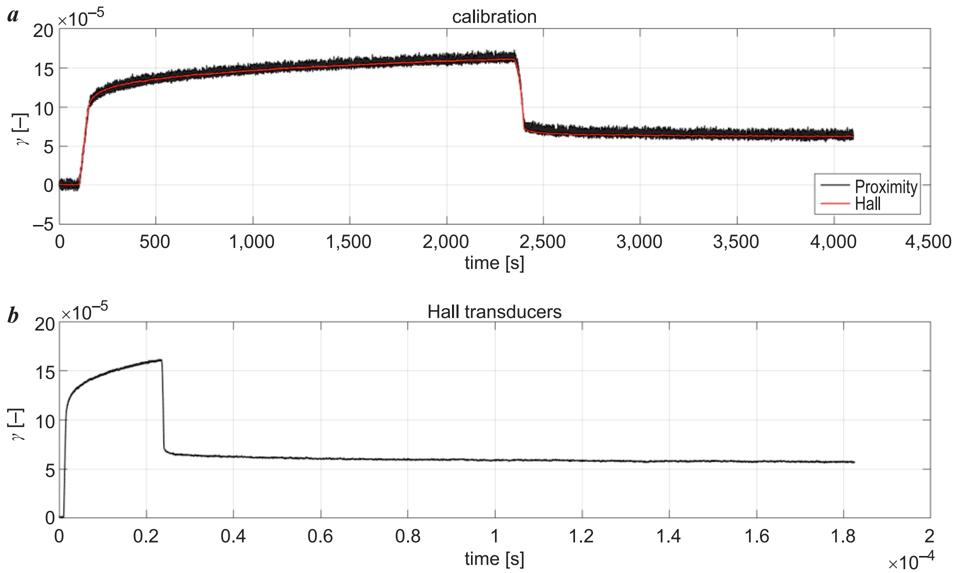

Fig. 7.18. P1 soil TS test results, *a* – calibration of proximity and Hall sensors, *b* – measurement of shear strain with Hall sensors, with extended recording time after unloading the sample – path SQ

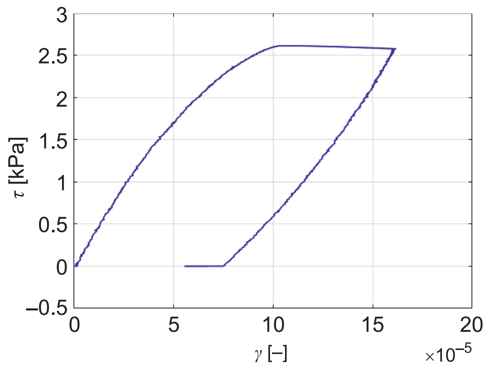

Fig. 7.19. P1 soil TS test results, hysteresis loop – SQ path

P2 soil

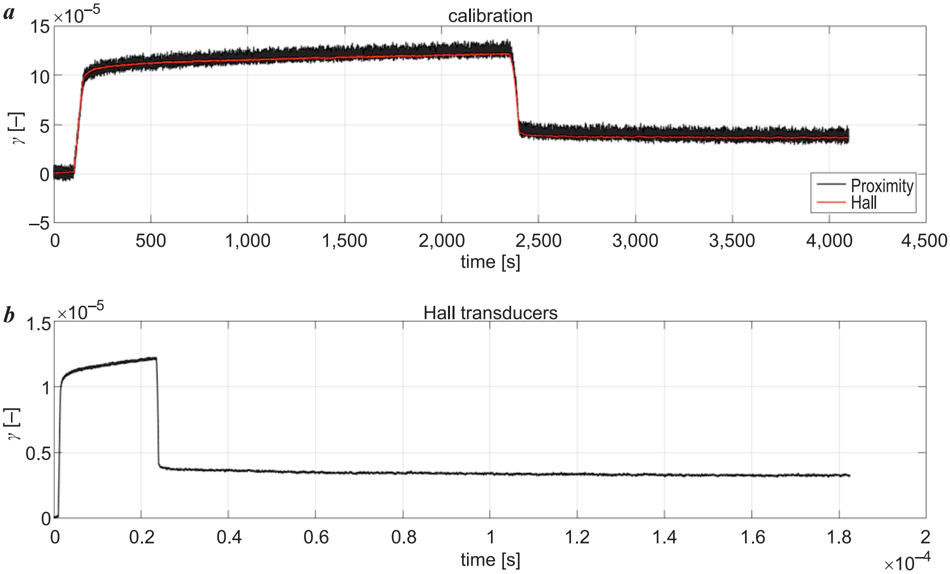

Fig. 7.20. P2 soil TS test results: *a* – calibration of proximity and Hall sensors, *b* – measurement of shear strain with Hall sensors, with extended recording time after unloading the sample – path SQ

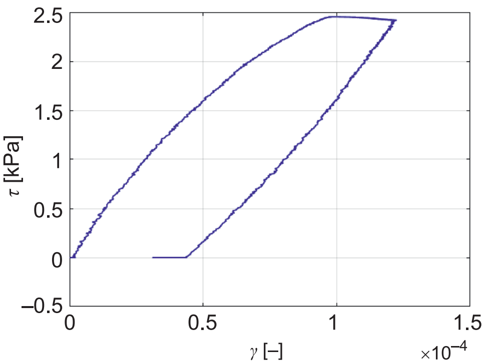

Fig. 7.21. P2 soil TS test results, hysteresis loop – SQ path

P3 soil

The highest recorded value of maximum strain occurred during the tests of soil sample P3 and reached γ_{max}=2.7·10^{-4} (fig. 7.22, 7.23). At the same time, it is a test during which the highest value of residual strain was recorded γ_{res}=0.70·10^{-4}, of all studies using both custom load paths.

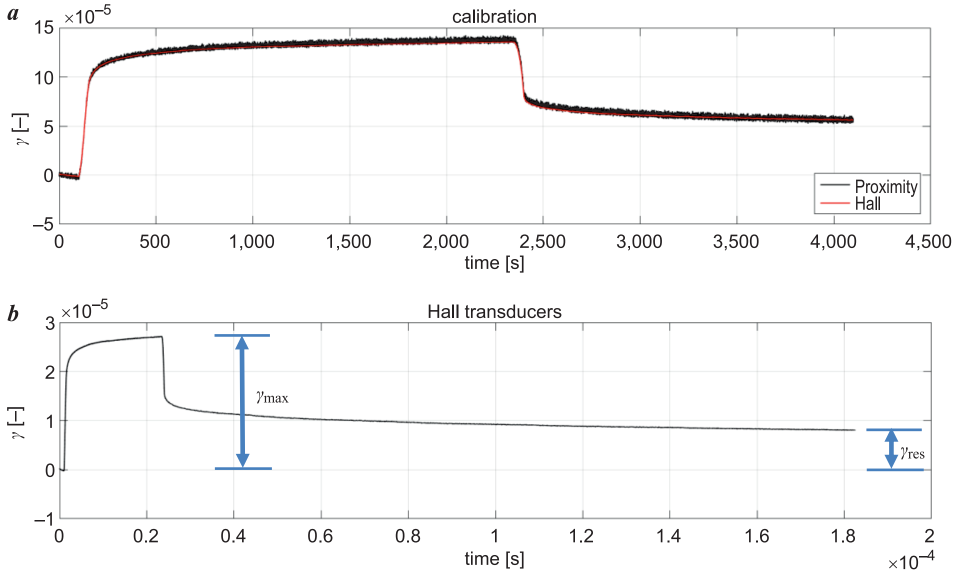

Fig. 7.22. P3 soil TS test results, *a* – calibration of proximity and Hall sensors, *b* – measurement of shear strain with Hall sensors, with extended recording time after unloading the sample – path SQ

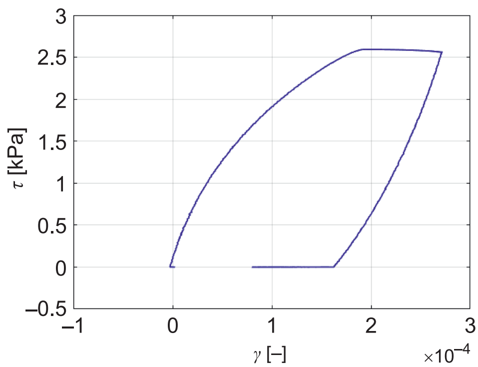

Fig. 7.23. P3 soil TS test results, hysteresis loop – SQ path

P4 soil

The P4 soil test (fig. 7.24, 7.25) is characterized by the smallest recorded (for SQ) value of maximum shear strain γ_{max}=1.1·10^{-4}, hence a noticeable is the relatively high noise level of standard proximity sensors.

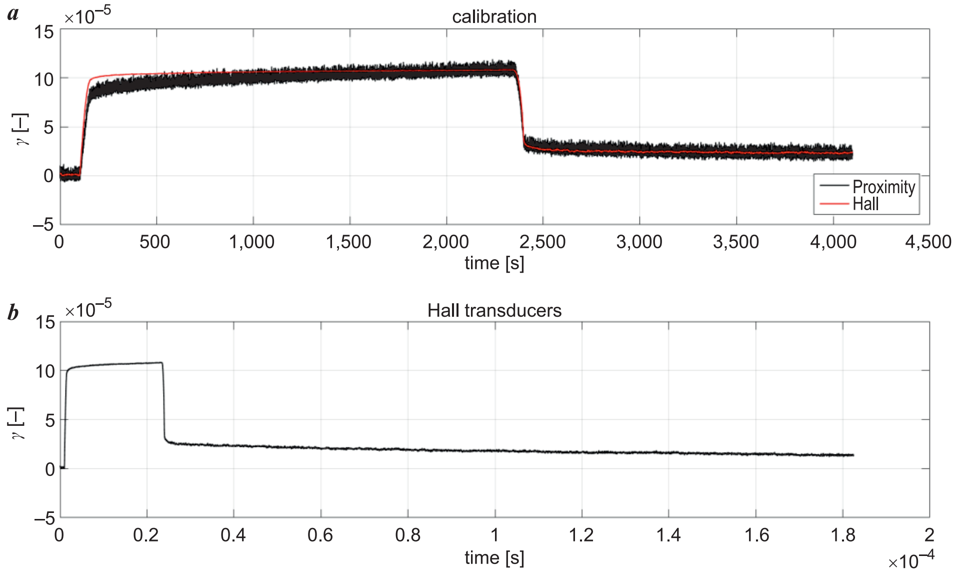

Fig. 7.24. P4 soil TS test results, *a* – calibration of proximity and Hall sensors, *b* – measurement of shear strain with Hall sensors, with extended recording time after unloading the sample – path SQ

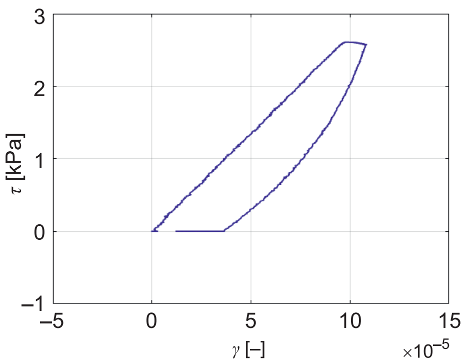

Fig. 7.25. P4 soil TS test results, hysteresis loop – SQ path

P5 soil

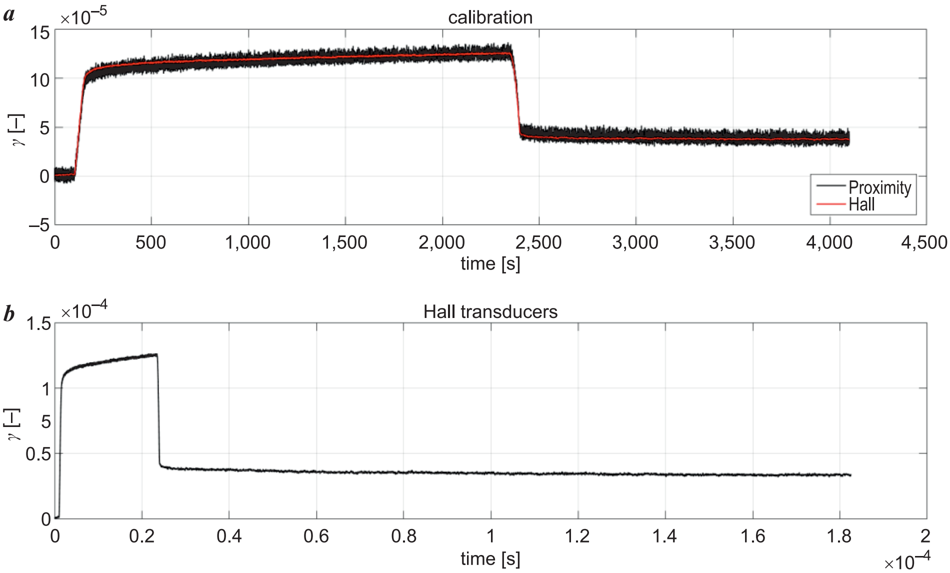

Fig. 7.26. P5 soil TS test results, *a* – calibration of proximity and Hall sensors, *b* – easurement of shear strain with Hall sensors, with extended recording time after unloading the sample – path SQ

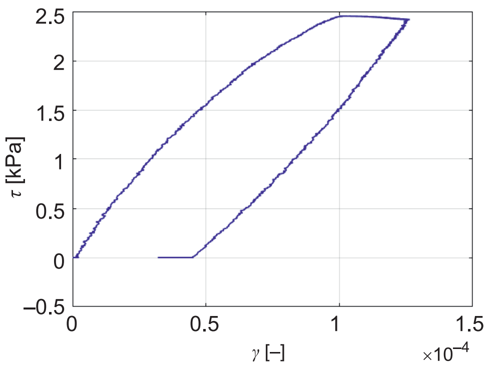

Fig. 7.27. P5 soil TS test results, hysteresis loop – SQ path

7.3. Summary

In each tested case, after unloading the soil, no stabilization of the residual strain value (γ_{res}) was recorded at the initial level of strain, i.e. recorded before the load was applied. The studies also measured the noise level of standard proximity sensors ($\Delta\gamma_{\text{noise,prox}}$). The repeatedly obtained $\Delta\gamma_{\text{noise}}$ values were close to γ_{res} from the same study, which justifies the parallel use of Hall sensors with higher accuracy (modification 3 – fig. 6.17). The noise level recorded by Hall sensors is imperceptible ($\Delta\gamma_{\text{noise,hall}}$). Despite the constant load amplitude of the designed paths, an increase in the recorded strain level was also noted in subsequent load cycles. This proves that the tested soil was plasticizing during the TS test.

No relation between the recorded values of permanent strain γ_{res} was observed with the values of the soil uniformity coefficient corresponding to the samples (C_U – tab. 7.2).

The differences between the first and last values of the maximum strain $\Delta\gamma_{\text{max}}$ were measured and, together with γ_{res} and $\Delta\gamma_{\text{noise}}$, are summarized in table 7.2.

Tab. 7.2. Summary of shear strain results from torsional shear tests carried out on sand samples

Path codename		CS20					SQ				
Sand		P1	P2	P3	P4	P5	P1	P2	P3	P4	P5
$\Delta\gamma_{\text{noise,prox}}$	10^{-4}	0.10	0.10	0.20	0.15	0.20	0.20	0.30	0.20	0.20	0.20
$\Delta\gamma_{\text{noise,hall}}$		0	0	0	0	0	0	0	0	0	0
γ_{max}		3.25	1.25	1.15	0.69	0.77	1.6	1.2	2.7	1.1	1.3
$\Delta\gamma_{\text{max}}$		0.55	0.20	0.30	0.10	0.60	0.40	0.10	0.30	0.20	0.15
$\boldsymbol{\gamma_{\text{res}}}$		**2.2**	**0.45**	**0.20**	**0.10**	**0.12**	**0.55**	**0.30**	**0.70**	**0.20**	**0.30**
C_U		1.6	3.0	4.0	2.0	4.0	1.6	3.0	4.0	2.0	4.0

Chapter 8

Optical method

8.1. Use of luminescent markers

As mentioned earlier, the standard interpretation of RC/TS test results is based on the assumption that the soil responds to load as a continuous viscoelastic material. This assumption results from the use of a measurement technique based on the twist angle Θ record in the only one plane of the sample cross-section – at its upper end. However, standard methodology of interpretation RC/TS test results provides no evidence that the sample always deforms proportionally along the entire height during the test (fig. 8.1). The correctness of this assumption was verified by author applying optical flow method for optical registration of sample surface deformation occurring during the torsional shear test. Author published first results in (Srokosz et al. 2021). Then a preliminary, simplified deformation mechanism of non-cohesive soil samples during torsion was proposed with introduction the concept of *active height* of the soil sample.

This chapter presents continuation of this research program with application of the optical flow method. Carrying out TS measurements, applying non-standard load paths (CS20 and SQ) with analyzing displacements of the sample (observed on its side surface) – was used in the further part of the work as a supplementary tool for the detection of permanent deformation in the residual phase of the test.

The prototype of the author's optical registration method of a sample side surface deformation is a technique based on the luminescent markers observation in time parallax. The method was developed to perform a qualitative analysis of the behavior of a soil sample during a torsional shear test. The research results were published (Bujko et al. 2017). In the publication, for the first time, a research hypothesis was put forward that in the TS torsional shear test, the torque can generate a material response only in a certain active part of the sample height (fig. 8.1*a*).

In order to verify the hypothesis, a qualitative analysis was carried out, based on the observation of displacements of self-made markers. The markers relate to selected points of the sample and the device rotor. This allows tracking of displacements during cyclic twisting of the system. A digital single-lens reflex camera was used to record the displacements.

The main difficulty that had to be faced was to develop the right concept for the installation of markers. The opacity of the latex membrane covering the sample made it impossible to observe the markers placed directly on the sample surface. On the other hand, the placement of markers on the membrane was also problematic due to the stiffness and continuity of its material. Installing markers on the membrane would prevent permanent contact of the marked points with the corresponding points on the surface of the tested sample. In addition, it should be noted that the observer and the sample are separated by two cylinders made of transparent material, which additionally hinders the registration of marker displacements.

The applied solution to this problem was the use of a photoluminescent material (exactly: strontium aluminate, europium and dysprosium doped) in the form of a crystalline powder. The markers used were placed under the membrane, directly on the sample and rotor (fig. 8.1*b*). Despite the

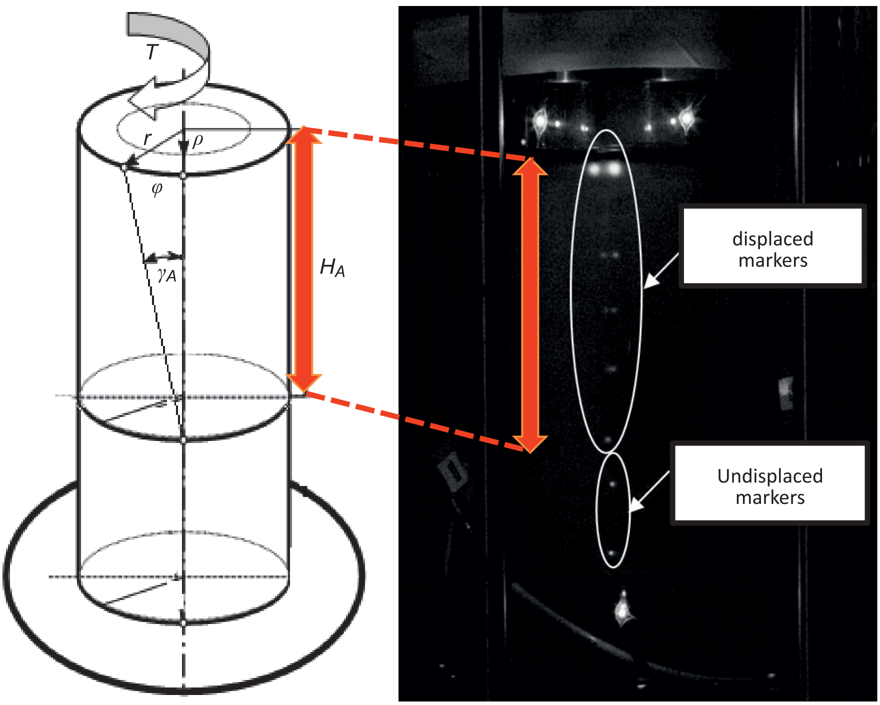

Fig. 8.1. Assumed mechanism of deformation of a sample loaded with a torque (*a*), optical measurement results using luminescent markers (*b*)
Source: after Bujko et al. (2017).

opacity of the rubber membrane, the markers, after irradiation with UV light, underwent the phenomenon of long-term luminescence (more precisely: phosphorescence), which allowed the observation of displacements of selected points of the deformed system. High quality of displacement registration of small marker points was ensured by a long exposure time and exposure in a specially darkened laboratory room. The effect of light refraction was reduced by the perpendicular orientation of the camera axis to the surface of the transparent cylinders.

The experimental results showed that during the torsional shear test on the RC/TS WF8500 apparatus, the luminescent markers located in the upper part of the sample move horizontally, while the markers in the part adjacent to the stationary base of the apparatus remain stationary. The experiment showed that only the part of the sample adjacent to the rotor of the apparatus reacted to the torque. This means that the actual shear strain generated in the sample could be much larger than the strain determined with the standard assumptions implemented into procedures of original software of the device (fig. 2.8 and 8.1*a*).

Due to the ratio of the size of the markers used (crystals with a diameter of $d \approx 1$ mm) to the size of the displacements obtained, the method remains ineffective for accurate quantitative analysis in the range of small strain ($\gamma < 10^{-3}$). For this purpose, it was justified to use the Optical Flow Method to determine the distribution of the sample displacement values along the height.

8.2. Fundamentals of optical flow methods

Laboratory research on soil deformation is carried out using contact and non-contact measurement methods. Among the non-contact methods, the most commonly used are techniques using wireless chemiluminescent sensors (Kuang 2018), fiber optic Bragg grating sensors (Xu 2017), PIV method and photogrammetry (White et al. 2003, Gill, Lehane 2001, Iskander 2010, Kong et al. 2018). In this work, the use of Optical Flow Method for laboratory research on soil deformation during torsional shear testing of soils was also proposed.

Originally, the concept of optical flow was introduced by the American psychologist James J. Gibson to describe the process of experiencing visual stimuli of moving animals (Gibson 1950, Barrows et al. 2003, Guletkin, Saranli 2013). Optical flow is defined as the distribution of the apparent velocities of change of the brightness distribution in the image. Optical flow can arise from the relative motion of objects and the observer. Therefore, it can provide important information on the spatial arrangement of the observed objects and the rate of changes in this arrangement (HORN, SCHUNCK 1981, HARTMANN et al. 2018).

The basic aspect in image sequence processing is the measurement of the optical flow (i.e. the velocity of image change). The goal is to approximate a projection of three-dimensional (3D) direction of surface points on two-dimensional (2D) image plane. It leads to obtaining a two-dimensional plane of motion (from spatio-temporal patterns of image feature intensity) (BARRON et al. 1994). Each point on the 3D surface is moving along a 3D $\vec{x}(t)$ path. Each point projected onto the image plane creates a 2D path trace:

$$\vec{x}(t) \equiv \Big(x(t), \big(y(t)\big)\Big)^T \tag{8.1}$$

from which the 2D velocity is calculated:

$$d\vec{x}(t)/dt \tag{8.2}$$

Formulas (8.1 and 8.2) have been used in practical problems of determining the maps of displacement using the recognition of spatial-temporal patterns of brightness intensity (FLEET, WEISS 2006) and flow techniques based on the analysis of color changes (KELSON et al. 2008, ANDREWS, LOVELL 2003).

Optical flow method based on the analysis of changes in brightness

A common starting point for optical flow estimation is to use a method based on gradient analysis, assuming that pixel intensities are transferred from one frame to another, satisfying the brightness conservation equation (ANDREWS, LOVELL 2003, FLEET, WEISS 2006):

$$I(\vec{x}, t) = I(\vec{x} + \vec{u}, t + 1) \tag{8.3}$$

where:

$I(\vec{x}, t)$ – the image intensity as a function of space $\vec{x} = (x, y)^T$ and time t,
$\vec{u} = (u_1, u_2)^T$ is the 2D velocity (FLEET, WEISS 2006).

The displacement (translation) d of the linear signal (image) is calculated as the difference in the values of the signals of the observed, displaced image point, and then by dividing this difference by the derivative value of the initial signal (8.4):

$$d = \frac{f_1(x) - f_2(x)}{f_1'(x)} \tag{8.4}$$

where:

$f_2(x)$ is the processed image $f_1(x)$ and d is the translation, where:

$$f_2(x) = f_1(x - d) \tag{8.5}$$

The derivative of the value of the initial signal has the following form:

$$F_1' = df_1(x)/dx \tag{8.6}$$

Using the formula (8.4) to calculate the displacements of non-linear signals, approximate value of the displacement is obtained (8.7) (see fig. 8.2). It is possible to introduce a 2D velocity estimator into the calculations.

$$\hat{d} = \frac{f_1(x) - f_2(x)}{f_1'(x)} \tag{8.7}$$

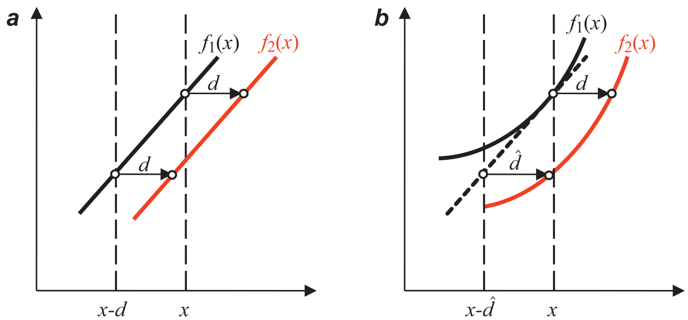

Fig. 8.2. Translation d of a linear signal (a) and approximation of translation of a non-linear signal (b)
Source: after Fleet and Weiss (2006).

The optical flow method based on brightness analysis takes into account the gradient constraint equation (8.8), which relates the velocity of image displacement to the space-time derivatives of the image in one place of the image:

$$\nabla I(\vec{x}, t) \cdot \vec{u} + I(\vec{x}, t) = 0 \tag{8.8}$$

where $\nabla I \equiv \left(I_x, I_y\right)$.

The assumption that must be met is that the observed brightness (intensity on the image plane) of any point of the object is constant in time. It means, that the following conditions should be met when observing and recording images:

- the glossiness of the surface remains constant from frame to frame of the image;
- no rotation of objects;
- no appearing, additional lighting;
- object of observation isn't distant.

The main disadvantage of the gradient estimation method is its sensitivity to conditions often found in real images. Densely textured areas, motion and image depth discontinuity constraints can be problematic. Even if the areas characterized by these conditions are small and localized (Kearney, Thompson 1986), additional constraints must be defined to obtain an unambiguous and stable solution to the problem (i.e. global optimization, known as the Horn-Schunck method or constant flow in the local region, known as the Lucas-Kanade Method; Lucas, Kanade 1981).

In addition to the brightness gradient, many optical flow estimation methods used for estimating the area of motion are based on the intensity of the image changing over time, including correlation, block matching, feature tracking, and energy methods. Despite the differences between optical flow techniques, many can be conceptually viewed in terms of three processing steps (Barron et al. 1994):

- reducing signal noises applying smoothing filters;
- extraction of basic measurements or local correlation surfaces;
- integration of extracted measurements to produce a two-dimensional flow map.

Optical flow method based on the analysis of changes in color

The optical flow method based on time parallax color analysis is characterized by three aspects:

- color can be treated in the same way as shades of grey;
- color components can carry additional information about the position of the analyzed points in the compared images;
- color components can be processed independently of each other.

Probably the first mention of optical flow based on color analysis was presented in the work of Ohta (1989) and the first proposal of the analysis technique can be found in Golland and Bruckstein (1997) (see: Andrews, Lovell 2003). Considering the aspect of possible color-based optical flow analyses, each color component represented in a particular color space forms an individual differential equation analogous to (8.9), satisfying the color conservation assumption:

$$\nabla I(\vec{x},t)_C \cdot \vec{u} + I(\vec{x},t)_C = 0 \qquad (8.9)$$

where the subscript C denotes the analyzed color component in the adopted color representation space. Andrews and Lovell (2003) proposed two methods for finding a solution to a poorly posed problem: reducing the number of equations by omitting a selected color component or using optimization techniques (i.e. least squares). Possibilities of using different color spaces are unlimited, the most commonly used spaces are: RGB, HSV, YUV, HSL, CMYK, CIEXYZ, CIELab, CIELUV, etc.

8.3. Scale Invariant Feature Transform method

The method of scale-invariant transformation of features was originally developed by David G. Lowe and as defined by the author: SIFT is a local descriptor (identifier) characterizing local gradient information (Lowe 1999). SIFT is used to measure velocities, displacements and strain based on the analysis of local features of images recorded in time parallax. The method consists in finding similarities in the analyzed images on the basis of distinctive features, most often structures created by groups of pixels. This approach transforms the image into a large collection of local feature vectors called SIFT keys, each of which is invariant for image translation, scaling, 3D projection (fig. 8.3).

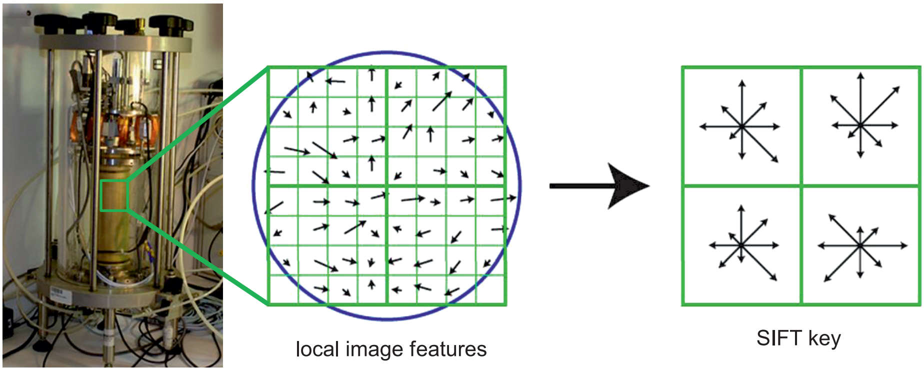

Fig. 8.3. Transformation of image features into a collection of SIFT keys

According to the paper (Lowe 1999) the method is also less sensitive to projection distortions and illumination changes, which has a significant advantage over other optical flow methods.

The scale-invariant features are efficiently identified by the stage filtering method. The first step identifies key points in the scale space. Each point is used to generate a feature vector that describes a local region of the image relative to its space-scale coordinates.

The method consists in the successive search for all possible displacement variants of the analyzed pixel structure. Ce Liu in 2009 introduced application of a coarse-to-fine matching scheme. This simplifying algorithm looks for larger structures (coarse) and similarities corresponding to these structures. Then it discretizes the search aiming at identifying details (fine). Algorithm doesn't analyze in detail all the possibilities of movement which significantly reduces the necessary computation time.

Figure 8.4*a* illustrates the process of identifying predefined image features (e.g. the brightness of a selected pixel along with its eight neighbors; see fig. 8.4*b*) in images $s^{(1)}$, $s^{(2)}$ $s^{(3)}$. The yellow rectangle indicates the search area for point p (the area is denoted by c_1, c_2, c_3 in the individual images). Symbols: p_1, p_2, p_3 – are points with x and y coordinates; $w(p_1)$, $w(p_2)$, $w(p_3)$ – are displacement vectors of point p with u and v coordinates.

To visualize the SIFT images, Liu obtained a 128-dimensional vector as the SIFT representation to track the pixel (SIFT key) and computed the three main components of the SIFT descriptor from the image set. Then these main elements of the SIFT descriptor were mapped into the main elements of the RGB space. Despite the apparent blurring of the SIFT visualization, in reality the image has a very high spatial resolution.

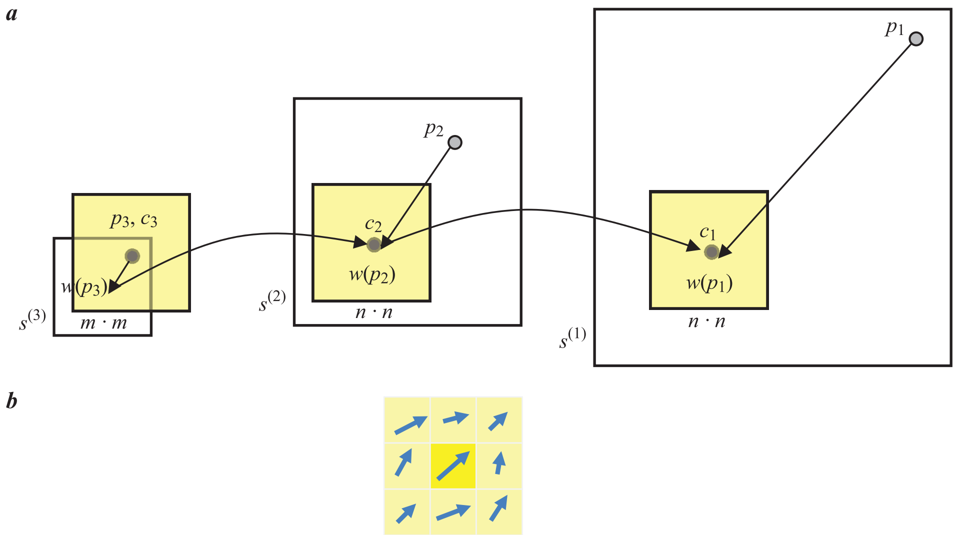

Fig. 8.4. The process of identifying previously defined image features (*a*), characteristics of the selected pixel along with its surroundings (*b*)
Source: after Liu (2009).

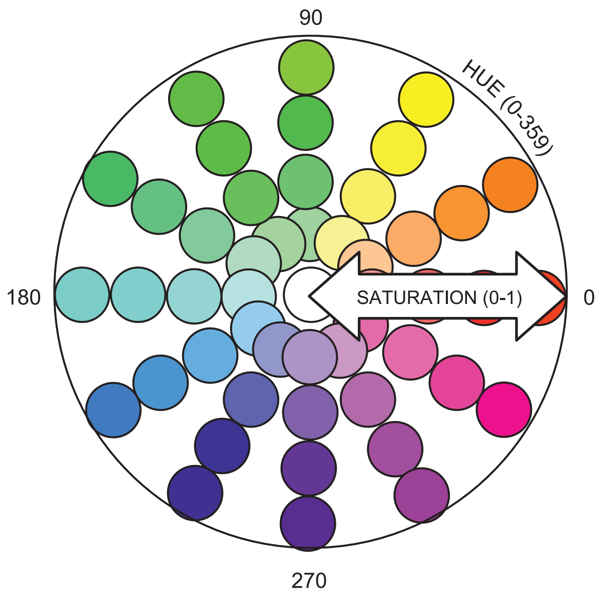

Fig. 8.5. HSV color space used to handle occlusion (for $V = 1$, Saturation $(0 \div 1)$, Hue $(0 \div 359)$)
Source: after Erdogan and Yilmaz (2014).

The method allows the user to dynamically change the observer's distance from the observed object (object depth). This distance is automatically interpolated using the smoothing function. The depth of the object is determined by the use of the HSV color space (fig. 8.5) (Erdogan, Yilmaz 2014). By setting the maximum values of the S (saturation) and V (value) parameters, the H (hue) parameter reflects the depth value of the object. Color deviation towards red indicates a lower depth value (objects are closer to the camera), while a color deviation towards blue indicates a greater depth value (objects are farther away from the camera).

8.4. TS research methodology using SIFT analysis

Author used optical flow functions, developed in the Matlab sofware by Liu (2009). For all displacement analyses both reference bases displacements were known (fixed bottom and twisting upper) and taken for correlation. Before applying the optical flow procedures, the image of the twisted sample had to be cropped to the observation area (fig. 8.6). In case of this application, this action not only significantly shorten computation time required for the analysis but also reduce image noises coming from background area.

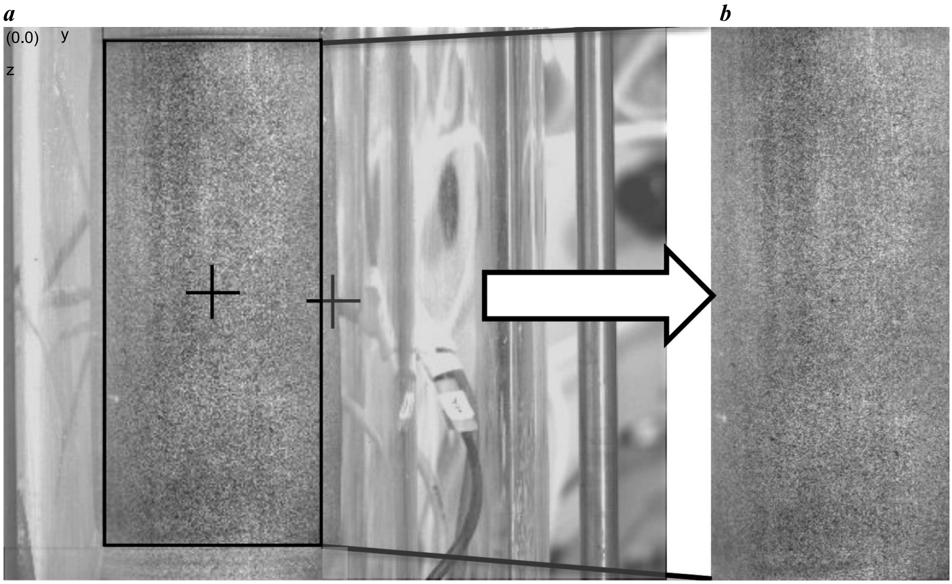

Fig. 8.6. Extraction of the observation area from the photo: a – the original image, b – extracted image
Source: after Srokosz et al. (2021).

Default parameters of the optical flow algorithm were suggested (Liu 2009). As a result of optimization through many preliminary calculations, author suggest to apply different values for this case of method implementation (tab. 8.1). Naturally, settings of optical flow alghorithm depend on application and object of observation, thus should be set and tested individually.

Tab. 8.1. Optical flow algorithm parameters

Values	Default	Applied
Regularization weight	1	0.02
Downsampling ratio	0.5	0.75
Range (width) of the coarsest cluster	40	20
Number of outer fixed point iterations	3	10
Number of inner fixed point iterations	1	3
Number of successive over-relaxation iterations	20	40

In publication (Srokosz et al. 2021) author highlighted significant measurement uncertainties of this method application. It is curvature of the sample and observation through transparent obstacles in the form

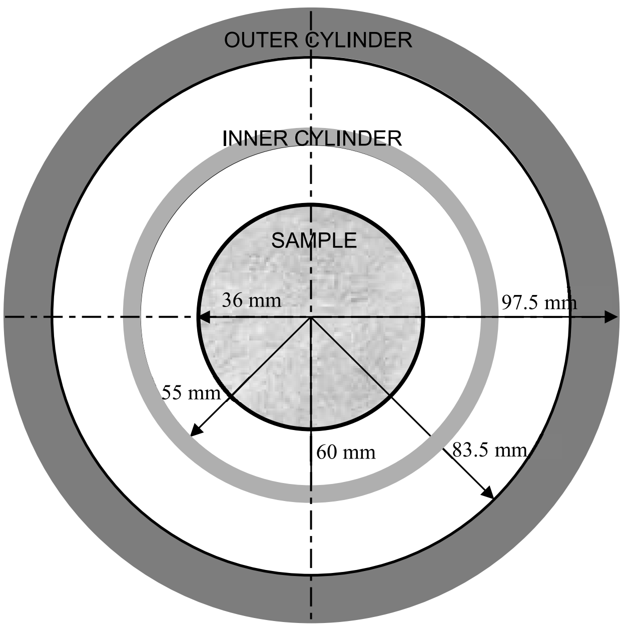

Fig. 8.7. Geometric data for the refraction correction
Source: after Srokosz et al. (2021).

of polycarbonate cylinders (fig 8.7). Due to the refraction of the light beam, necessary image corrections was proposed in form of application Snell's Law for ray tracing (fig 8.7).

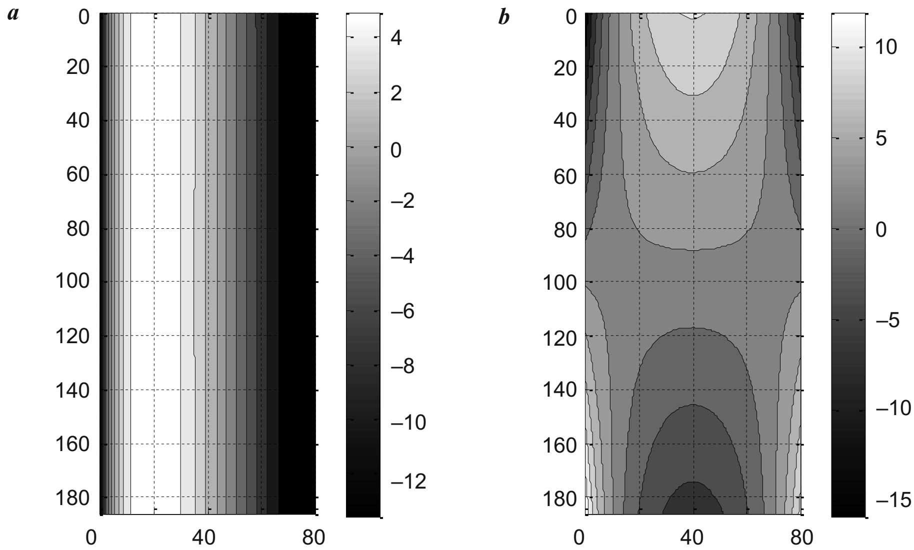

Fig. 8.8. Correction maps for the photo shown in figure 8.6: *a* – width correction d_y [mm], *b* – height correction d_z [mm]
Source: after Srokosz et al. (2021).

8.5. Research stand

For the purposes of displacement analyses and optical flow method application, author recreated setup of research stand and presented in the paper (Srokosz et al. 2021). This is depicted in figure 8.9 and consisted of:

– RC/TS WF8500 apparatus;
– 5-megapixel digital camera of the ARAMIS 5M measurement system;
– 1 kW halogen lighting.

Crucial issue was the optimal illumination of the side surface of the sample. Therefore, it was achieved by illumination with light reflected from the white ceiling of the laboratory and short-time sample illumination by LED lamp to focus ARAMIS lenses. Whole stand was covered behind by thick white curtains to provide constant ilumination conditions and eliminate influence of external sources of light. The photos were taken at intervals of 1 s.

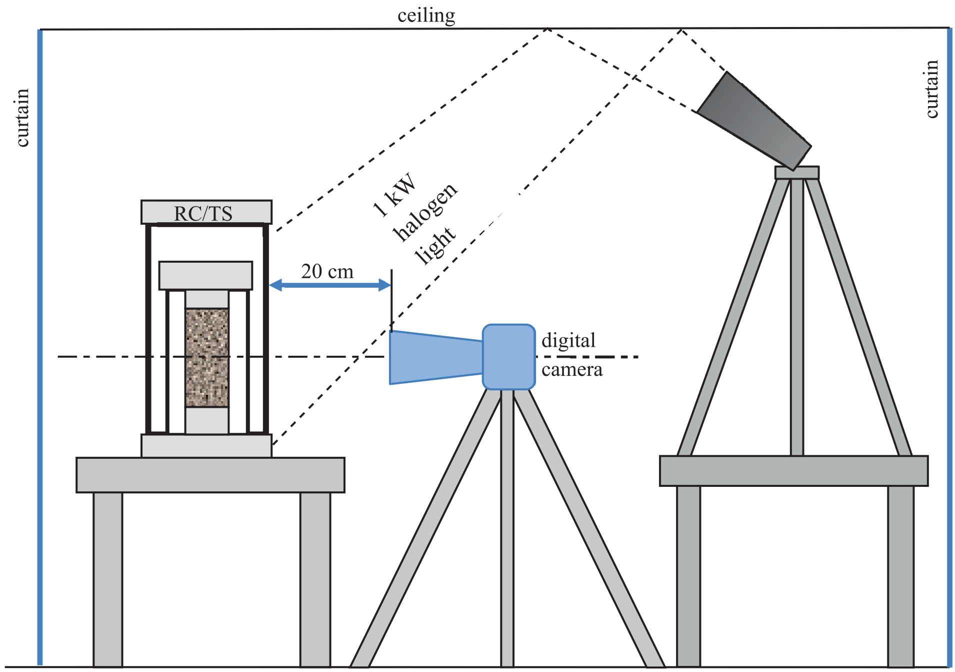

Fig. 8.9. Research stand
Source: after SROKOSZ et al. (2021).

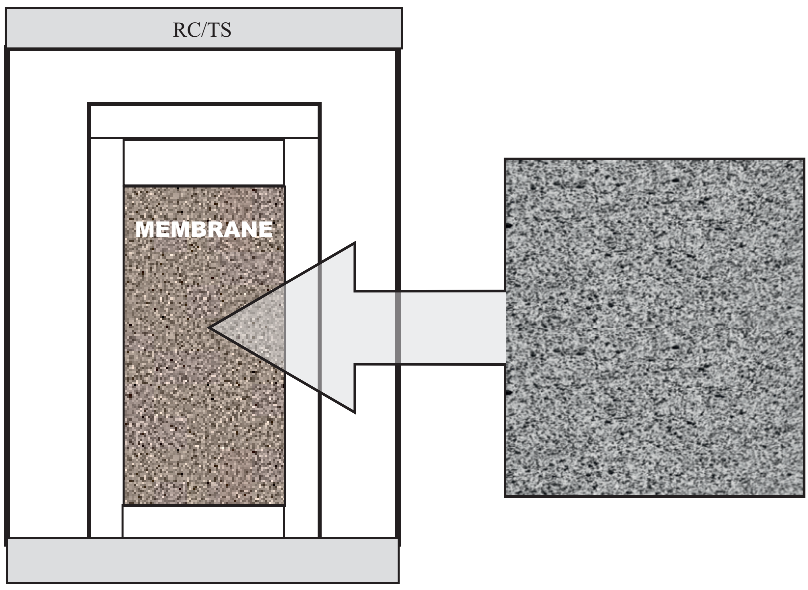

Fig. 8.10. View of a soil sample in a latex membrane covered with a fine reference pattern
Source: after SROKOSZ et al. (2021).

Reference pattern consisting of light and dark spots on the surface of the sample is necessary for optical registration of displacements. Therefore, reference pattern was applied to the surface of the latex membrane, inside which the sample is placed. The pattern was created by spraying a thin layer of acrylic white and black paint, creating contrasting dots (fig. 8.10).

Non-cohesive soils described in section 7.1 were selected for testing. For the purposes of the optical flow SIFT analysis, in section 8.6.1 were used the results of TS tests carried out on samples with the P2 and P4 grain size distribution curves. In section 8.6.2 , the TS test results for sample with P1 grain size distribution curves were used.

8.6. Results of displacement analysis

8.6.1. Non-standard load paths

Author carried out torsional shear tests, with a modified recording procedure, applying both non-standard load paths (CS20 and SQ – see section 7.2). Parallel to the TS tests, an analysis of displacements was carried out using the SIFT Optical Flow Method. The test program included the use of soils with grain size curves P1, P2, P3, P4 and P5 (see section 7.1). Section shows the maps of displacement at the key moments of the TS test: the states of maximum and minimum twist amplitude and the residual state, respectively. Then, for the presented maps of displacement, displacement graphs were made using the range (average width) of 200 pixels of the analyzed band.

This section presents the results of analyses of two selected cases: for P2 soil under load with CS20 path and P4 soil under load with SQ path. In the conclusions section (see table 7.1, Chapter 7.3) the amplitudes Δd of horizontal and vertical displacements changing with the height of the sample are listed.

Due to the significant influence on the determination of the shear modulus, the key aspect for the analysis is the distribution of horizontal displacements along the height of the sample. For vertical displacement results, negative values indicate reduction the height of the sample, and positive values – an increase. However, in all the cases of test results presented in the work, the influence of vertical displacements on the evaluation of the shear modulus is negligible.

CS20 path – P2 soil

In case of testing P2 soil with CS20, visible low contrast in optical flow maps is the result of loading the soil sample with a very small load, which generates soil response in the range of very small strain. Despite application optical flow algorithm was used to register extremely small changes in a series of images, postprocessing the resulting maps allowed to obtain visible distribution of displacements along the height of the soil sample. Figure 8.11 shows map of displacement the state of maximum twist amplitude during the TS test

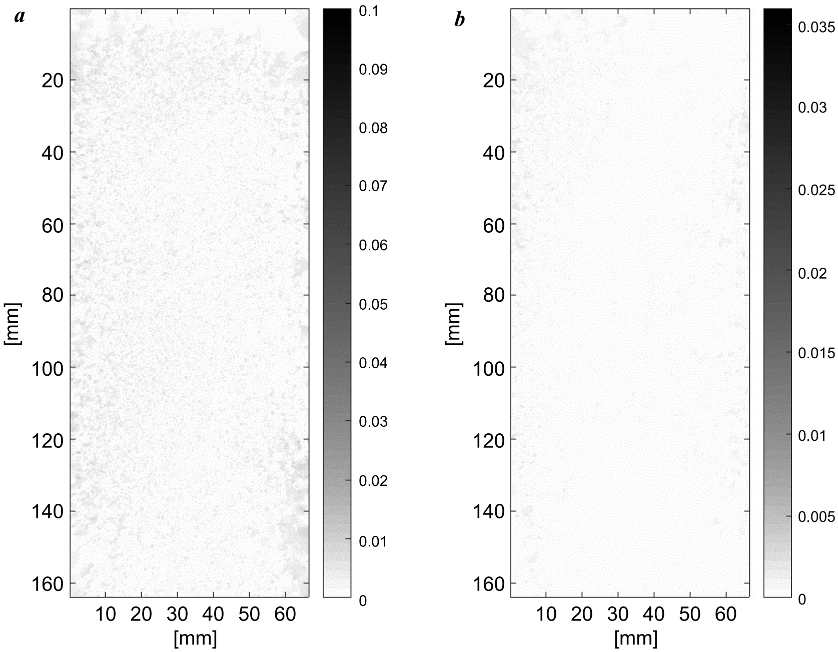

Fig. 8.11. Results of optical flow analysis in full resolution (P2 soil, 762×1852 grid): *a* – horizontal displacements [mm] at **maximum** twist angle, *b* – corresponding vertical displacements

It should be highlighted that, in case of soil response in the range of very small strain, this distribution is almost linear in each phase of the test (example in fig. 8.12). This stands in a contrast to the results of analyses based on the TS tests performed with a standard load path. Figure 8.13 shows map of displacement the state of minimum twist amplitude during the TS test. Figure 8.15 shows map of displacement at the residual state of the TS test.

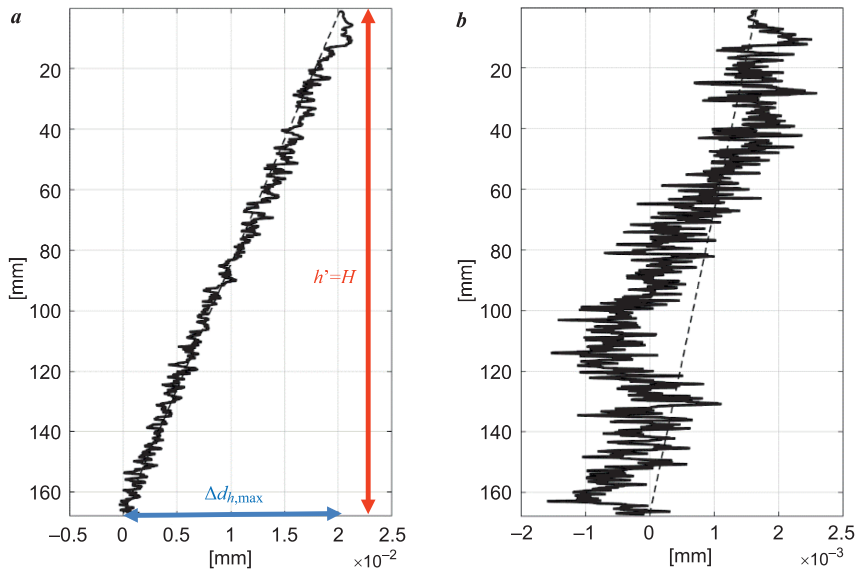

Fig. 8.12. Results of optical flow analysis (P2 soil, average width: 200 pixels): *a* – horizontal displacements [mm] along the height of the specimen in the phase of maximum twist angle, *b* – corresponding vertical displacements [mm]; dashed line – assumed linear relationship between displacement and sample height

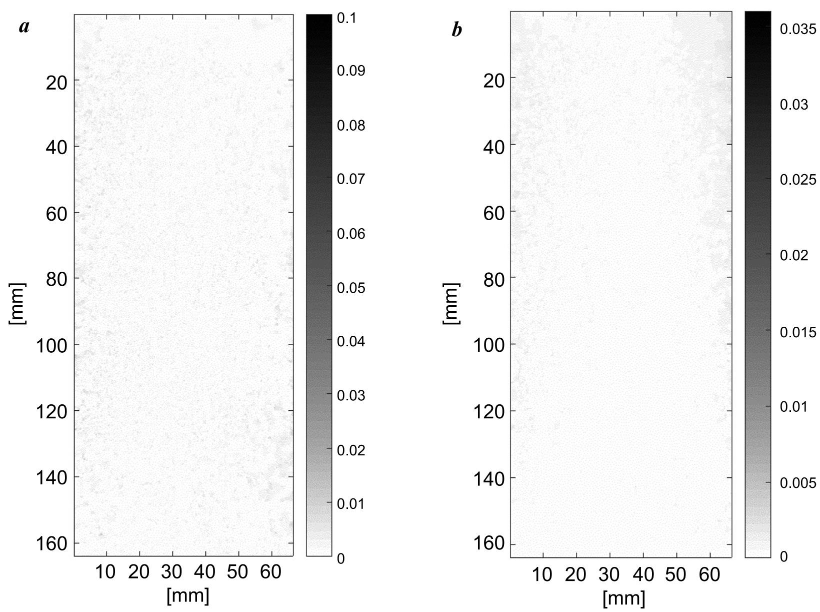

Fig. 8.13. Results of optical flow analysis in full resolution (P2 soil, 762×1852 grid): *a* – horizontal displacements [mm] at **minimum** twist angle, *b* – corresponding vertical displacements

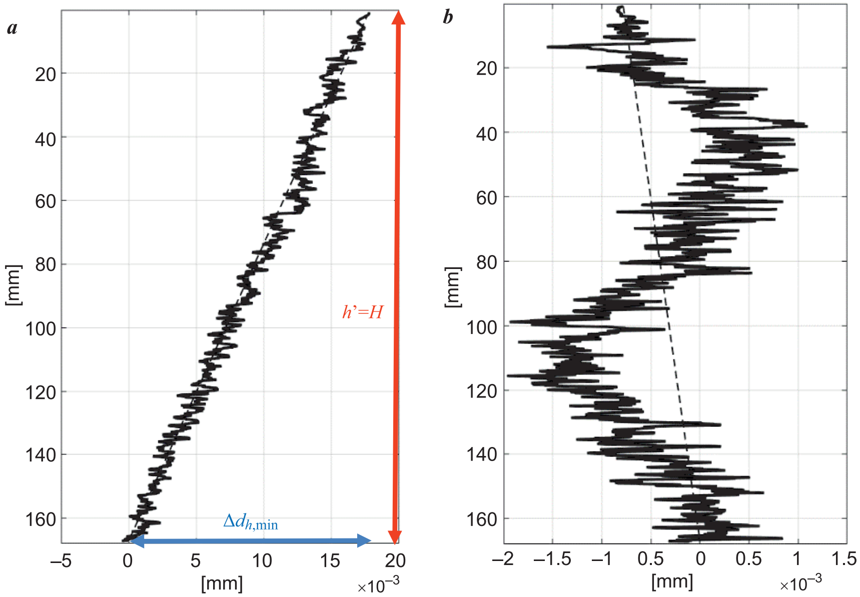

Fig. 8.14. Results of optical flow analysis (P2 soil, average width: 200 pixels):
a – horizontal displacements [mm] along the height of the specimen in the phase of minimum twist angle, *b* – corresponding vertical displacements [mm]

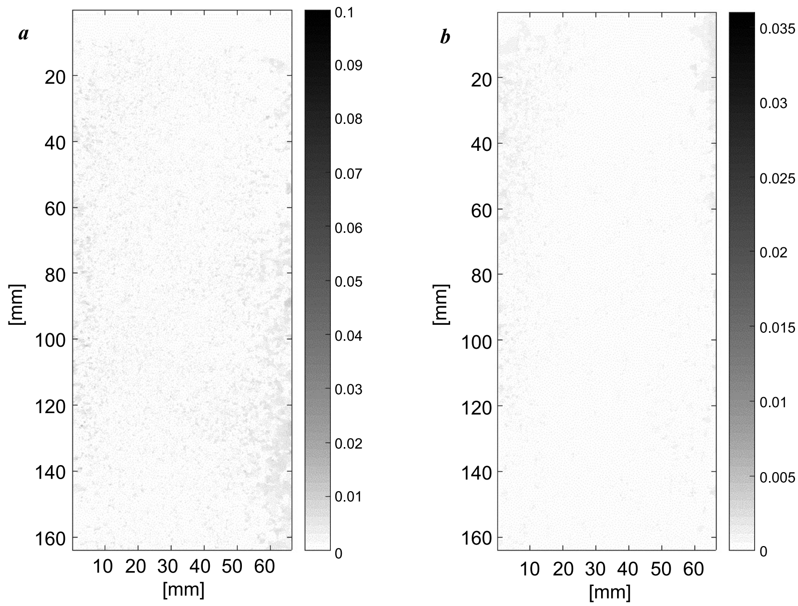

Fig. 8.15. Results of optical flow analysis in full resolution (P2 soil, 762×1852 grid):
a – horizontal displacements [mm] at **residual** state,
b – corresponding vertical displacements [mm]

The most important outcome of this analysis is the evidence for permanent deformation in residual state of this test. In spite of the soil response in the range of very small strain, upper part of sample remained displaced $\Delta d_{h,\text{res}}$ long after the test (fig. 8.16).

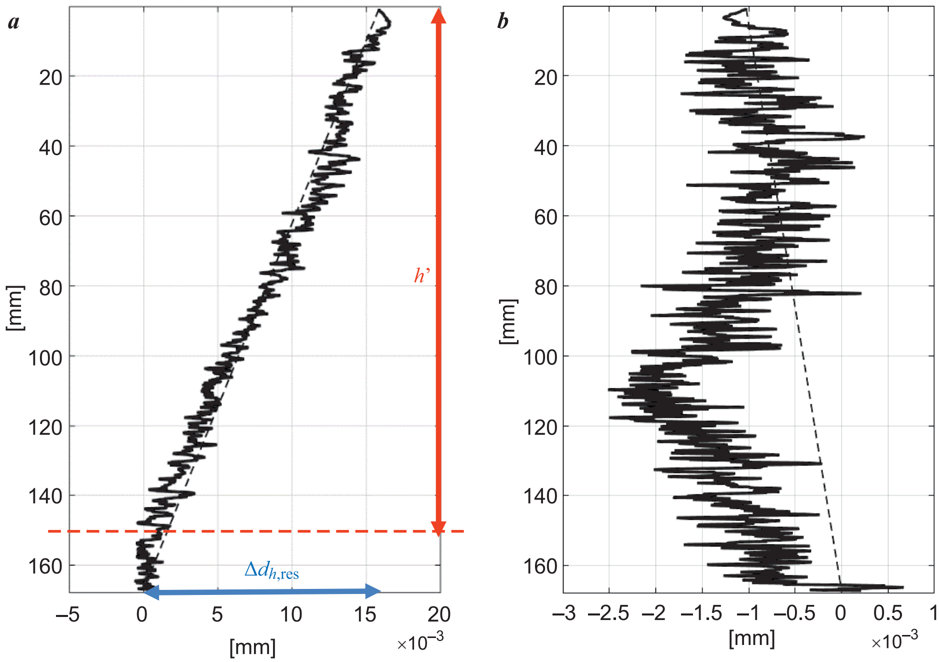

Fig. 8.16. Results of optical flow analysis (P2 soil, average width: 200 pixels):
a – horizontal displacements [mm] along the height of the specimen in the residual phase,
b – corresponding vertical displacements [mm]

SQ path – P4 soil

The example below illustrates how different might be the deviation of the distribution of horizontal displacements from the assumed linear relationship between the displacement and the height of the sample. Figure 8.17 shows map of displacement the state of maximum twist amplitude during the TS test. In figure 8.18, the sign of the deviation reverses twice: near the upper and bottom bases ($h_{f,u}$, $h_{f,b}$). Figure 8.19. shows map of displacement the state of minimum twist amplitude during the TS test.

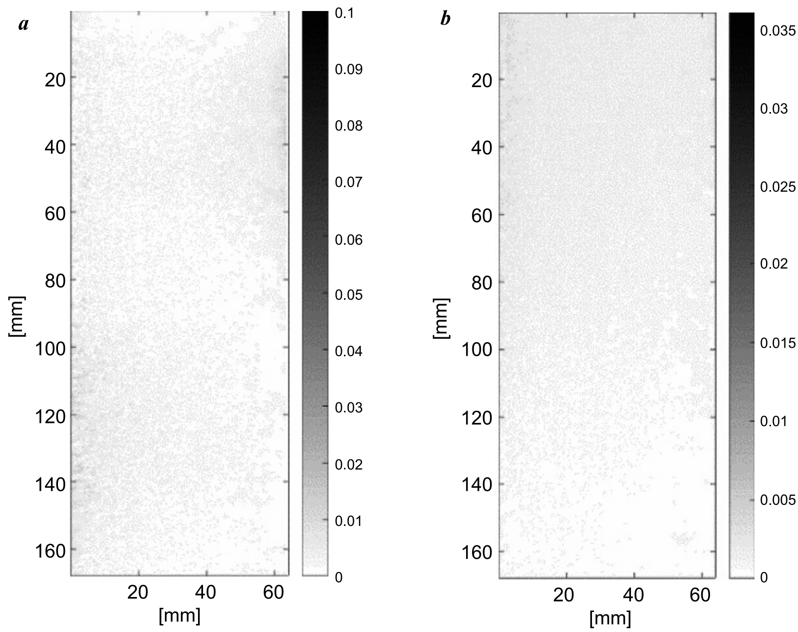

Fig. 8.17. Results of optical flow analysis in full resolution (P4 soil, 659×1757 grid):
a – horizontal displacements (mm) at maximum twist angle,
b – corresponding vertical displacements [mm]

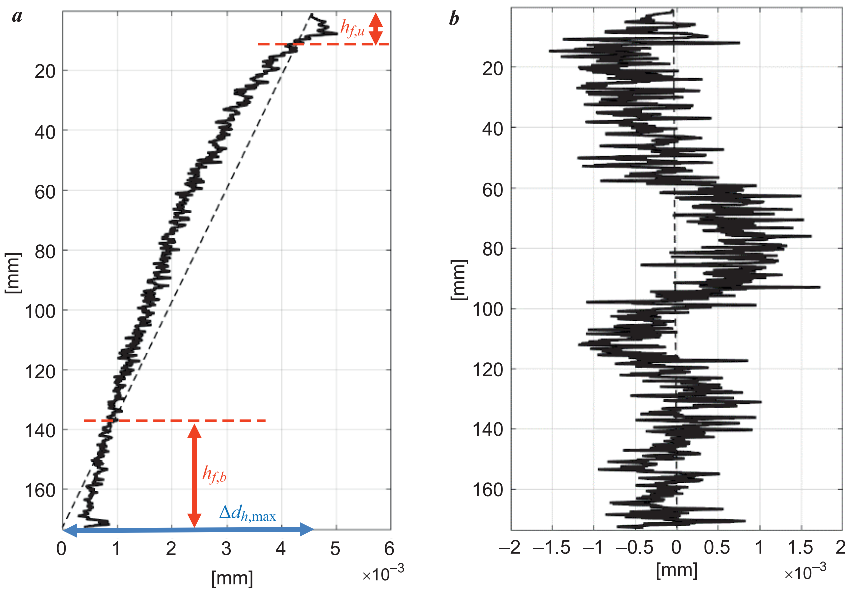

Fig. 8.18. Results of optical flow analysis (P4 soil, average width: 200 pixels):
a – horizontal displacements [mm] along the height of the specimen in the phase of maximum twist angle, *b* – corresponding vertical displacements [mm];
dashed line – assumed linear relationship between displacement and sample height

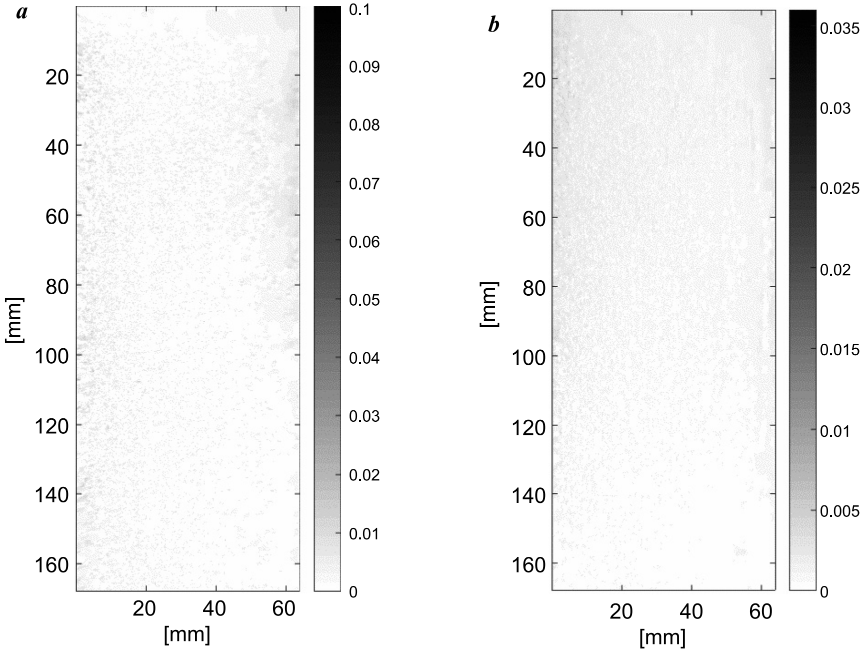

Fig. 8.19. Results of optical flow analysis in full resolution (P4 soil, 659×1757 grid):
a – horizontal displacements [mm] at minimum twist angle,
b – corresponding vertical displacements [mm]

According to result shown in figure 8.20, reversing sign of deviation may manifest problems with providing friction of the bases to the sample during operation of the device. This anomaly would have gone unnoticed if the optical method was not applied to record the displacements of the side surface of the sample. Figure 8.21 shows map of displacement at the residual state of the TS test. Value of amplitude of horizontal displacement in the residual phase of this tests proves the soil material remained deformed after the test (fig. 8.22).

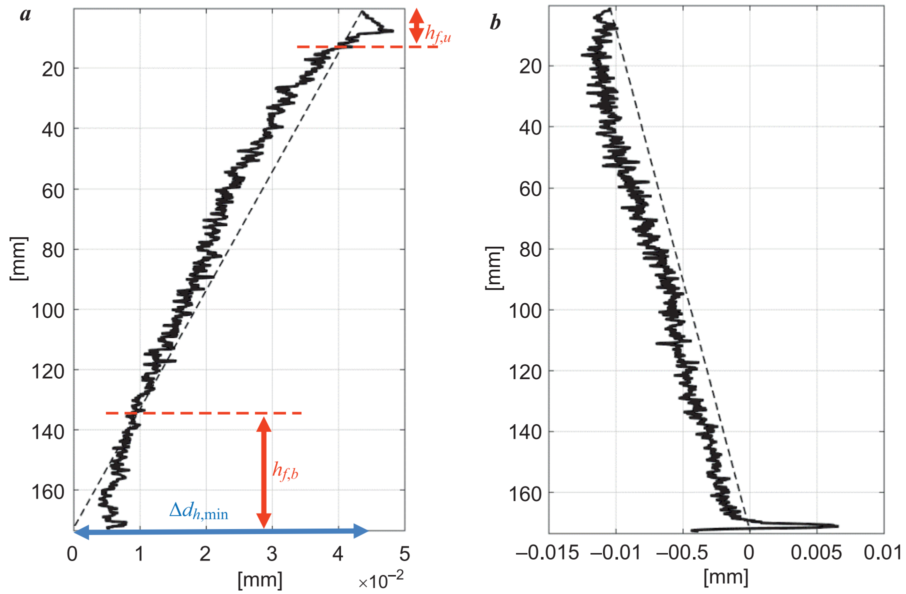

Fig. 8.20. Results of optical flow analysis (P4 soil, average width: 200 pixels): *a* – horizontal displacements [mm] along the height of the specimen in the phase of minimum twist angle, *b* – corresponding vertical displacements [mm]

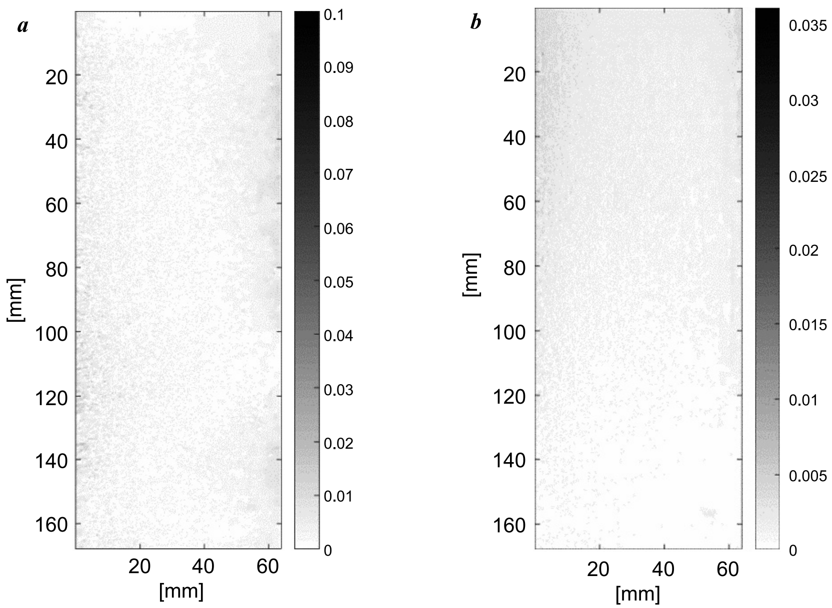

Fig. 8.21. Results of optical flow analysis in full resolution (P4 soil, 659×1757 grid): *a* – horizontal displacements [mm] at **residual** state, *b* – corresponding vertical displacements [mm]

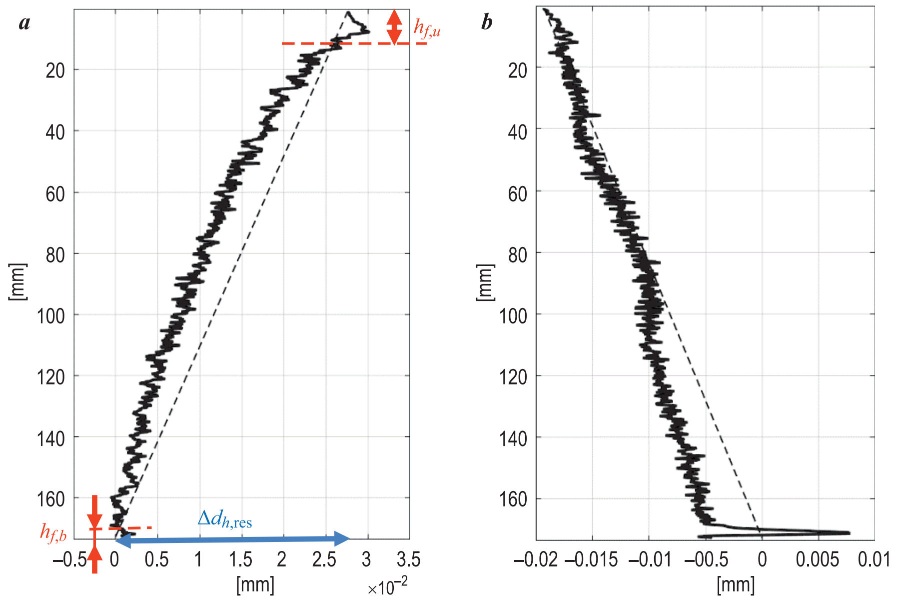

Fig. 8.22. Results of optical flow analysis (P4 soil, average width: 200 pixels): *a* – horizontal displacements (mm) along the height of the specimen in the residual phase, *b* – corresponding vertical displacements [mm]; dashed line – assumed linear relationship between displacement and sample height

8.6.2. Standard load path

Horizontal displacements might not change linearly along the sample's height and the relation of horizontal displacements to the height of the sample might take a different form depending on the phase of the test. Author highlighted this phenomenom in the paper (Srokosz et al. 2021) and performed cyclic torsional shear test using standard load path with the following parameters:

Tab. 8.1. Cyclic TS test parameters

Soil	Load path	p [kPa]	A [V]	f [Hz]	Cycles [-]	Observation time after the test [s]
Sand P1	standard	0.2	1.0	0.01	3	16,000

The results recorded as standard by the WF8500 are shown in figure 8.23. As indicated in the figure 8.23, the resulting hysteresis loop is not closed, thus material didn't return to its original state before loading at the end of the

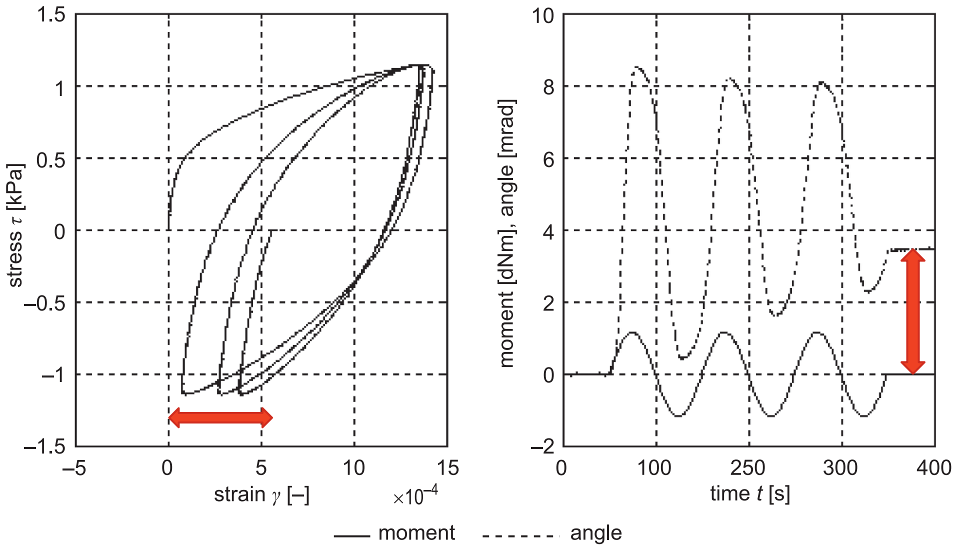

Fig. 8.23. TS test results (standard load path, soil P1)
Source: after Srokosz et al. (2021).

standard test. Optical Flow method was applied for displacement analysis with extension the observation time after the test up to 16,000 seconds (almost 4.5 hours) to confirm the occurence of this phenomenom.

Formation of the non-linear distribution of displacements is apparent in each phase of the test (example in fig. 8.24). Author interprets this fact as an effect of the lack of homogeneity of the soil material. Height of the sample interacting with the load – *the active height* (fig. 8.25) is variable and depends on many factors, of course, including the internal structure of the tested material. Distribution of horizontal displacements in the residual phase indicates irreversible deformation of soil sample 4.5 hours after the test (fig. 8.26).

Due to the presence of a active height h', the actual shear strain γ can be much larger than the shear strain calculated taking into account the value of total height of the sample according to the model formula (8.10):

$$\gamma(\theta) = \frac{\rho\theta}{H} \tag{8.10}$$

where:

ρ – bulk density,
Θ – twist angle,
H – sample height.

Maps of displacement at the key phases of the TS test: phase of the maximum and minimum twist angle and phase of the residual state are presented below.

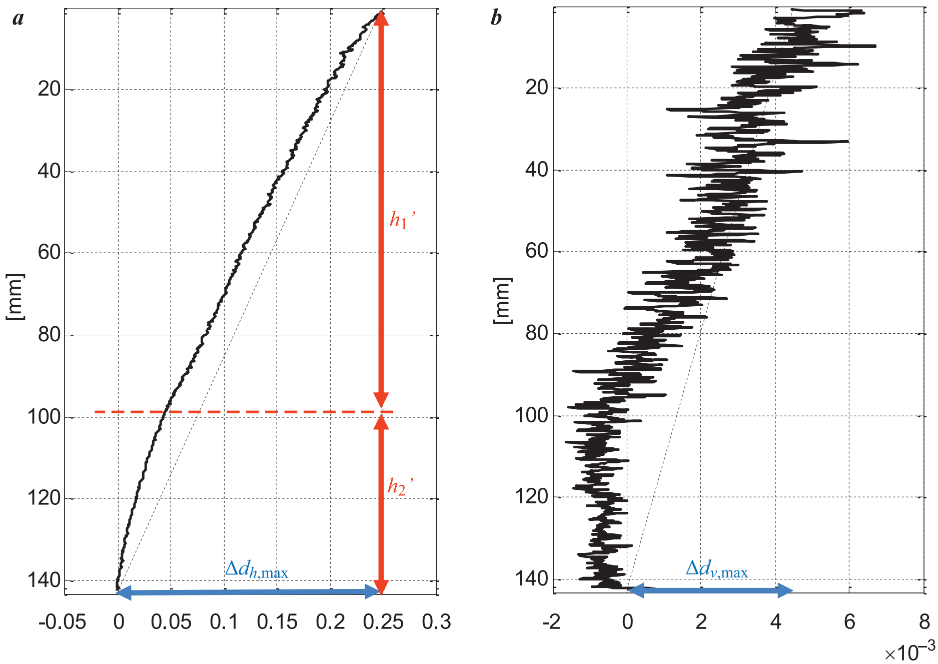

Fig. 8.24. Results of optical flow analysis (P1 soil, average width: 200 pixels):
a – horizontal displacements [mm] along the height of the sample at maximum twist angle,
b – corresponding vertical displacements [mm]; dashed line – assumed linear relationship between the displacement and the height of the sample
Source: after SROKOSZ et al. (2021).

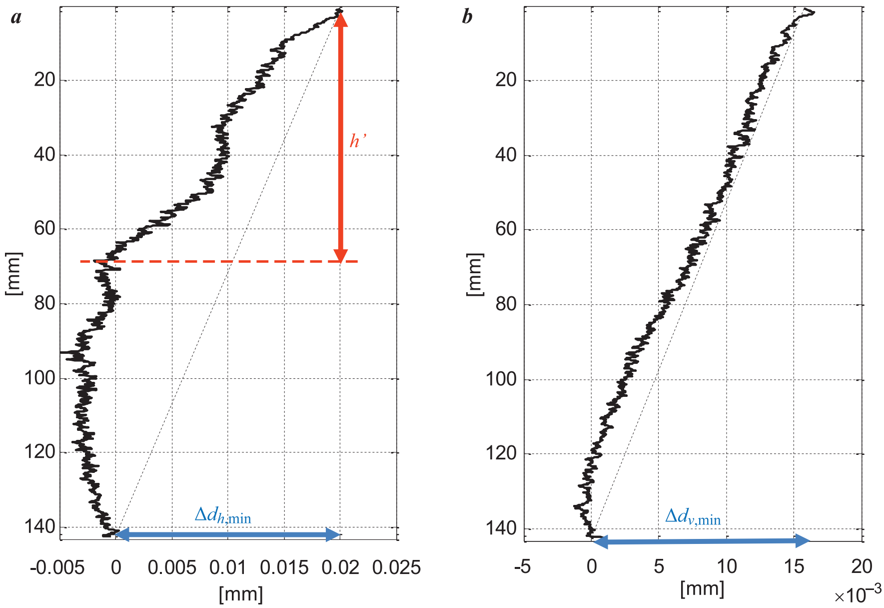

Fig. 8.25. Results of optical flow analysis (P1 soil, average width: 200 pixels): *a* – horizontal displacements [mm] at minimum twist angle, *b* – vertical displacements [mm]
Source: after Srokosz et al. (2021).

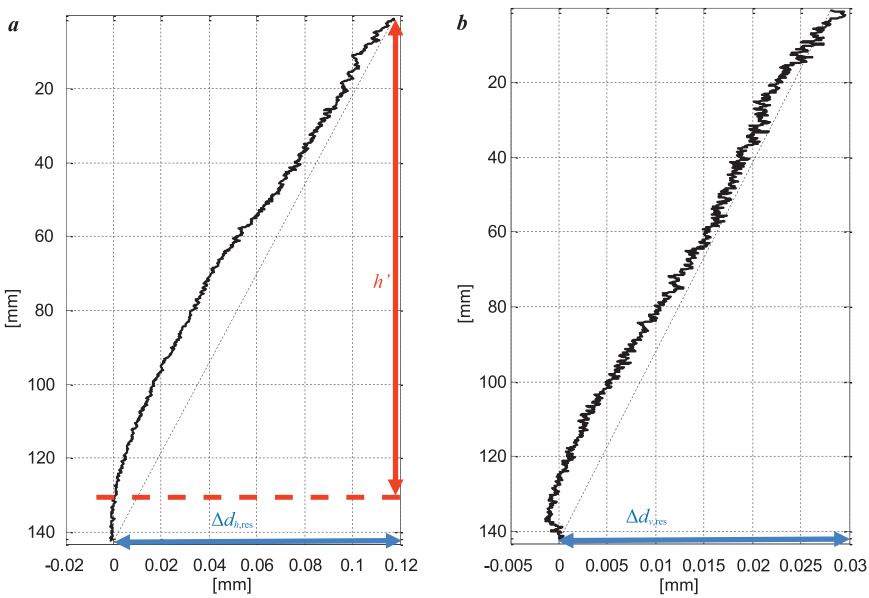

Fig. 8.26. Results of optical flow analysis (P1 soil, average width: 200 pixels):
a – horizontal displacements [mm] along the height of the sample at residual state,
b – corresponding vertical displacements [mm]
Source: after Srokosz et al. (2021).

8.7. Summary

Optical flow postprocessing allowed to obtain displacement distribution along the height of soil sample. Displacement distribution can take different forms depending on the phase of the same test. With the decreasing level of shear strain, the distribution of horizontal displacements approaches linearity. However, the condition for the proper assessment of displacements is to ensure appropriate friction conditions of the sample against the rigid lower base and the torsion upper base. The author interprets the formation of the non-linear distribution of displacements as an effect of the lack of homogeneity of the soil material, regardless of the method of forming the samples.

In each tested case non-zero values of horizontal displacement amplitudes in the residual phase $\Delta d_{h,\mathrm{res}}$ were obtained. It indicates the material does not return to its original state of deformation, but it is characterized by a new deformation state, state of plastic deformation. As a consequence, the soil subjected to torsional load acts as a viscoelastoplastic material.

The amplitudes Δd of horizontal and vertical displacements are listed below and vertical ones. Table 8.2 summarizes the results of the TS tests carried out on both non-standard load paths (P2 and P4 soil, see chapter 8.7.1) in comparison with results related to standard path (P1 soil, see chapter 8.7.2).

Tab. 8.2. Displacement amplitudes *Δd* based on the results of the assumed linear relationship between the displacement and the height of the sample P1(standard load path), P2 (CS20) and P4(SQ)

Displacement amplitude	P2 (CS20 load path)	P4 (SQ load path)	P1 (standard load path) (Srokosz et al. 2021)
Phase at maximum twist angle			
Horizontal [mm]	0.02	0.045	0.25
Vertical [mm]	0.0016	0.001	0.0045
Phase at minimum twist angle			
Horizontal [mm]	0.0175	0.043	0.2
Vertical [mm]	-0.0003	-0.011	0.016
Residual phase			
Horizontal [mm]	**0.016**	**0.027**	**0.12**
Vertical [mm]	-0.001	-0.019	0.028

Chapter 9

Conclusions

On the basis of the presented test results, it can be concluded that the proposed modernization of the torsional shear test methodology allows to extend the use of the RC/TS device to a wider range of applications for soil material observations. As a consequence, it enables the identification of aspects related to the behavior of the soil material subjected to torsion loading, which were unavailable with the standard use of the RC/TS apparatus.

The proposed TS test methodology in terms of: generating loads, testing supervision and recording results allows for generation of freely designed load paths, reducing inaccuracies of sensor indications and extension the duration of shear strain measurement after unloading the sample with a torque. The use of non-standard, custom load paths potentially extends the practical scope of the device's use in engineering practice – it allows for the measurement of soil shear strain, recreating a model of subsoil behavior in specific load conditions, not only cyclical.

The device has been modified in terms of hardware and software. Consequently, it allowed to measure values of residual shear strain γ_{res} in the range of small strain that indicate that after unloading, the material does not return to its original state of deformation, but it is characterized by a new deformation state, the state of plastic deformation.

The research results contained in the work indicate that, the use of the SIFT algorithm, belonging to the group of optical flow methods, can be a useful supplementary tool to carry out a detailed analysis of the displacements of the lateral surface of the soil sample. A significant limitation of the method is its sensitivity to lighting conditions, which poses a challenge in the form of precise adjustment of the test stand. However, this method provides the opportunity to obtain detailed information on the behavior of the soil material during its loading. An example is the observed singularity, which may be related to the problems of ensuring the friction of the sample material to the device both bases. The fact of detecting the existence of the phenomenon of active sample height is of particular importance because the actual strains of the sample may consequently be much greater than indicated by the standard software of the device. In addition, this method allows you to track changes in the reaction range of the sample material (the value of the active sample height) in any selected phase of the test. Finally, the optical flow method was used as a supplementary tool to confirm the research thesis about the irreversibility of shear strains in the range of small strains during the twisting of the sample in the torsional shear apparatus.

In the context of the conducted research, the influence of viscosity is manifested, among other things, by an increase in the values of volumetric strains in subsequent loading cycles. An example of this is depicted in Chapter Seven, according to TS test results using the loading path CS20, where non-zero values of differences in maximum strains were recorded $\Delta\gamma_{max}$ between the first and last loading cycles. However, the author acknowledges that directly from the presented research results, it is not possible to conduct a quantitative analysis regarding the individual influence of this phenomenon, as it occurs simultaneously with the successive plasticization of the soil. The author has shown that cyclically lost energy is not completely regenerated in the system by the external work of the device, and the sample undergoes irreversible deformation, which, according to the author, is the cumulative effect of viscoelasticplastic material behavior.

The author performed a total of 310 TS tests at various values amplitudes and pressures. The tests presented in the work is part of research program and are used to verify the research thesis. The author decided to acquaint the reader with the complete history of author's research on elasto-plastic phenomena, which ultimately led him to the verification of the thesis regarding the occurrence of plastic deformation within the range of small strains. Although the author focused his research on testing non-cohesive soils, some preliminary tests conducted on cohesive soils are also presented in the work (for purposes such as back analysis and initial sensor calibration). Below, in table 9.1, author included a tabular summary of all TS tests that results were presented in the work.

The author limited the research to test non-cohesive soils of 3-4% moisture content. Preliminary tests on cohesive soils were carried out under conditions with drainage and without consolidation. Possible extension of the research program with tests on cohesive soils in controlled conditions of saturation and consolidation requires, further, significant modification of the device structure.

Tab. 9.1. TS tests presented in the work

Test No.	Soil	Isotroptic Pressure	Load Path	Amplitude	Frequency	Test Description
1	sand	48.6	standard	±6	0.01	standard TS tests, FEM application for back analysis
2	sand	28.6	standard	±4	0.01	
3	silt	49.2	standard	±8	0.01	
4	silty clay	49.2	standard	±7	0.01	standard TS tests, genetic algorithms for back analysis (after Srokosz et al. 2017)
5	silty clay	49.2	standard	±1	0.01	
6	silty clay	0,2	standard	±5	0.01	standard TS test, strain gauge sensor
7	sand P1	30	standard	±1	0.01	standard TS test, optical flow method (after Srokosz et al. 2021)
8	sand P1	30	CS20	±3 to ±5	0.01	modified TS test, custom load paths, Hall sensors and optical flow method
9	sand P1	30	SQ	±5	-	
10	sand P2	30	CS20	±3 to ±5	0.01	
11	sand P2	30	SQ	±5	-	
12	sand P3	30	CS20	±3 to ±5	0.01	
13	sand P3	30	SQ	±5	-	
14	sand P4	30	CS20	±3 to ±5	0.01	
15	sand P4	30	SQ	±5	-	
16	sand P5	30	CS20	±3 to ±5	0.01	
17	sand P5	30	SQ	±5	-	

The main limitation of presented, fixed-free RC/TS apparatus is the method of controlling the pore pressure and thus the saturation and consolidation of the sample. Both the measurement of the pore pressure and the backpressure are performed at the same level of the bottom base surface of the sample. Both saturation and consolidation are impossible to achieve with such device design. Tests carried out so far raise doubts whether the measured pore pressure refers to the material of the soil sample and not to the pore stone itself. In order to carry out the process of saturation of soil samples, the author plans to modify the design of the rotor in terms of the installation of a pipe supplying liquid from the equalizing pressure control system.

Bibliography

Allen J., Stokoe K.H. 1982. *Development of Resonant Column Apparatus with Anisotropic Loading*. Geotechnical Engineering Report GR82-28, Geotechnical Engineering Center, The University of Texas, Austin.

Alpan I. 1970. *The Geotechnical Properties of Soils*. Earth Science Reviews, 6, 5-49.

Andrews R.J., Lovell B.C. 2003. *Color Optical Flow*. Proceedings of the 2003 APRS Workshop on Digital Image Computing, Brisbane, 1, 129-133.

Arany L., Bhattacharya S., Macdonald J., Hogan S.J. 2017. *Design of Monopiles for Offshore wind Turbines in 10 steps*. Soil Dynamics and Earthquake Engineering, 92, 126-152.

Atkinson J.H., Sallfors G. 1991. *Experimental determination of soil properties.* General Report to Session 1. Proceedings of the 10th ECSMFE, Florence, 1991, 915-956.

Atkinson J.H. 2000. *Non-Linear Soil Stiffness in Routine Design*. Geotechnique, 50(5), 487-508.

Bae Y.-S., Bay J.A. 2009. *Modifications of Resonant Column and Torsional Shear Device for the Large Strain*. Computers and Geotechnics, 36(6), 944-952,

Barron J.L., Fleet D.J., Beauchemin S.S. 1994. *Performance of Optical flow Techniques*. International Journal of Computer Vision, 12(1), 43-77.

Barrows G.L., Chahl J.S., Srinivasan M.V. 2003. *Biologically Inspired Visual Sensing and Flight Control*. Aeronautical Journal, 107(1069), 159–268.

Benz T. 2007. *Small Strain Stiffness of Soils and Its Numerical Consequences*. PhD thesis, Universitat Sttutgart.

Biarez J., Hicher P.-Y. 1994. *Elementary Mechanics of Soil Behaviour*. Saturated Remoulded Soils. A.A. Balkema, Rotterdam.

Birch F., Bancroft D. 1938. *Elasticity and Internal Friction in a Long Column of Granite*. Bulletin of the Seismological Society of America, 28, 243-254.

Burland J.B. 1979. *Contribution to Discussion on Session 4*. In: *The Measurement, Selection, and Use of Design Parameters in Geotechnical Engineering*. Proceedings of the Seventh European Conference on Soil Mechanics and Foundation Engineering, Brighton, England, September 1979, 4, 137. British Geotechnical Society, London.

Burland J.B., Cole K.W. 1972. *Observation of Retaining Wall Movements Associated with a Large Excavation*. Proceedings of 5th ECSMFE, Madrid, 1, 445-453.

Bujko M. 2018. *Identification of Elastoplastic Phenomena in Soils in the Range of Small Strains*. IOP Conference Series Materials Science and Engineering, 471, 042013.

Bujko M., Srokosz P.E., Dyka I. 2017. *Use of Optical Method for Improvement of Soil Dynamic Tests in Torsional Shear Apparatus*. 2017 Baltic Geodetic Congress (BGC Geomatics), 1, 404-408.

Burland J.B. 1989. *9-th Lauritis Bjerrum Memorial Lecture: Small is Beautiful. The Stiffness of Soils at Small Strains*. Canadian Geotechnical Journal, 26(4), 499-516.

Cabalar A.F. 2010. *Applications of the Oedometer, Triaxial and Resonant Column Tests to the Study of Micaceous Sands*. Engineering Geology, 112(1-4), 21-28.

Liu C. 2009. *Beyond Pixels: Exploring New Representations and Applications for Motion Analysis*. PhD thesis. Massachusetts Institute of Technology, Cambridge.

Chen W.-F. 1975. *Limit Analysis and Soil Plasticity*. Developments in Geotechnical Engineering, 7.

Chen W.-F., Saleeb A.F. 1994. *Constitutive Equations for Engineering Materials*. Vol. 1. *Plasticity and Modeling*. Studies in Applied Mechanics, 37A. Elsevier, Amsterdam--London-New York-Tokyo.

Chen W.-F., Liu X.-L. 1990. *Limit Analysis in Soil Mechanics*. Developments in Geotechnical Engineering, 52.

Chen X.-L., Xing J., Tao X.-X. 2008. *Comparisons of 5 Types of Soil Dynamic Nonlinear Constitutive Models in Seismic Response of Site*. The 14th World Conference on Earthquake Engineering, Beijing.

Chong S.-H., Kim J.-Y. 2017. *Nonlinear Vibration Analysis of the Resonant Column Test of Granular Materials*. Journal of Sound and Vibration, 393, 216-228.

Cudny M., Niemunis A. 2018. *Discussion on "Dynamic Soil-Structure Interaction: A Three--Dimensional Numerical Approach and Its Application to the Lotung Case Study". Poor Performance of the HSS Model*. Computers and Geotechnics, 98, 243-245.

Cudny M. 2013. *Some Aspects of the Constitutive Modelling of Natural Fine Grained Soils*. IMOGEOR, Gdańsk.

Cudny M., Partyka E. 2015. *Wpływ anizotropii w modelowaniu odkształcenia podłoża wywołanego drążeniem tunelu*. Inżynieria Morska i Geotechnika, 5, 705-715.

Cudny M., Truty A. 2020. *Refinement of the Hardening Soil Model within the Small Strain Range*. Acta Geotechnica, 15, 2031–2051.

Diaz-Rodriguez J.A., Lopez-Molina J.A. 2008. *Strain thresholds in soil dynamics*. The 14-th World Conference on Earthquake Engineering, October 12-17, 2008, Beijing, China.

Drnevich V.P., Hall J.R., Richard F.E. 1967. *Effects of Amplitude of Vibration on the Shear Modulus of Sand*. Proc., Int. Symp. on Wave Propagation and Dynamic Properties of Earth Mat., Albuquerque, N.M., 1, 189-199.

Drnevich V.P. 1978. *Resonant-Column Testing: Problems and Solutions*. Dynamic Geotechnical Testing, ASTM STP 654, American Society for Testing and Materials, 384-398.

Drnevich V.P., Hardin B.O., Shippy D. 1978. *Modulus and Damping of Soils by the Resonant-Column Method*. Dynamic Geotechnical Testing, ASTM STP 654, American Society for Testing and Materials, 91-125.

Duncan J.M., Chang C.Y. 1970. *Non-Linear Analysis of Stress and Strain in Soils*. Journal of Geotechnical Engineering (ASCE), 96(5), 1629-1653.

Dyka I. 2009. *W sprawie obliczania osiadania pali w grupie*. Inżynieria i Budownictwo, 12, 669-673.

Dyka I., Srokosz P. 2012. *Badania gruntu w aparacie skrętnego ścinania RC/TS*. Część 1. Inżynieria Morska i Geotechnika, 6, 700-707.

Dyka I., Srokosz P. 2014. *Badania gruntu w aparacie skrętnego ścinania RC/TS*. Część 2. Inżynieria Morska i Geotechnika, 2, 118-129.

Dyka I., Srokosz P.E., Bujko M. 2017. *Influence of Grain Size Distribution on Dynamic Shear Modulus of Sands*. Open Engineering, 7(1), 317-329.

Erdogan K., Yilmaz N. 2014. *Shifting Colors to Overcome not Realizing Objects Problem due to Color Vision Deficiency*. Proceedings of the 2nd International Conference on Advances in Computing, Electronics and Electrical Technology – CEET, Kuala Lumpur, Malaysia, 1, 11-14.

Fahey M. 1998. *Deformation and in Situ Stress Measurement*. Proceedings International Conference on Site Characterization, ICS '98, 1, Atlanta, GA, 1, 49-68.

Fares R., Santisi d'Avila M.P., Deschamps A. 2019. *Soil-Structure Interaction Analysis using a 1DT-3C Wave Propagation Model*. Soil Dynamics and Earthquake Engineering, 120, 200-213.

Fleet D.J., Weiss Y. 2006. *Optical Flow Estimation*. Handbook of Mathematical Models in Computer Vision, 237-257.

Gibson J.J. 1950. *The Perception of the Visual World*. Houghton Mifflin Company, Boston.

Gill D., Lehane B. 2001. *An Optical Technique for Investigating Soil Displacement Patterns*. Geotechnical Testing Journal, 24(3), 324-329.

Golland P., Bruckstein A.M. 1997. *Motion from Color*. Computer Vision and Image Understanding, 68, 346-362.

Gultekin G.K., Saranli A. 2013. *An FPGA Based High Performance Optical Flow Hardware Design for Computer Vision Applications*. Microprocessors and Microsystems, 37(3), 270-286.

Hardin B.O., Black W.L. 1966. *Sand Stiffness Under Various Triaxial Stresses*. Journal of the Soil Mechanics and Foundations Division, 92, 27-42.

Hardin B.O., Drnevich V.P. 1972. *Shear Modulus and Damping in Soils: Measurement and Parameter Effects*. Proc. ASCE: Journal of the Soil Mechanics and Foundations Division, 98, 603-624.

Hardin B.O., Drnevich V.P. 1972. *Shear Modulus and Damping in Soils: Measurement and Parameter Effects*. Proc. ASCE: Journal of the Soil Mechanics and Foundations Division, 98, 667-692.

Hartmann, C., Wang, J., Opristescu, D., Volk, W. 2018. *Implementation and Evaluation of Optical Flow Methods for Two-Dimensional Deformation Measurement in Comparison to Digital Image Correlation*. Optics and Lasers in Engineering, 107, 127-141.

Horn B.K.P., Schunck B.G. 1981. *Determining Optical Flow*. Artificial Intelligence, 17(1-3), 185-203.

Hoyos L.R., Suescún-Florez E.A., Puppala A.J. 2015. *Stiffness of Intermediate Unsaturated Soil from Simultaneous Suction-Controlled Resonant Column and Bender Element Testing*. Engineering Geology, 188, 10-28.

Ishimoto M., Iida K. 1936. *Determination of Elastic Constants by Means of Vibratio Methods*. Part 1. *Young's Modulus*. Bulletin of Earthquake Research Institute, 14, 632-657.

Iskander M. 2010. *Optical Techniques in Geotechnical Engineering*. *Modelling with Transparent Soils*. Springer Series in Geomechanics and Geoengineering. Berlin.

Jardine R.J., Potts D.M., Fourie A.B., Burland J.B. 1986. *Studies of the Influence of Nonlinear Stress-Strain Characteristics in Soil-Structure Interaction*. Geotechnique, 36(3), 377-396.

Jardine R.J., Symes M.J. 1995. *One Perspective of the Pre-Failure Deformation Characteristics of Some Geomaterials*. Pre-Failure Deformation of Geomaterials, Balkema, Rotterdam.

Jardine R.J., Symes M.J., Burland J.B. 1984. *The Measurement of Soil Stiffness in the Triaxial Apparatus*. Géotechnique, 34(3), 323–340.

Kearney J.K., Thompson W.B. 1986. *Bounding Constraint Propagation for Optical Flow Estimation*. In: *Motion understanding*. Ed. W.N. Martin, J.K. Aggarwal. Kluwer Academic Publishers, Dordrecht.

Kelson R.T.A., Santana A.M., Medeiros A.A.D. 2008. *Optical Flow Using Color Information*. Proceedings of the 2008 ACM Symposium on Applied Computing (SAC), Fortaleza, Ceara, Brazil, March 16-20.

Khan Z., El Naggar M. H., Cascante G. 2011. *Frequency Dependent Dynamic Properties from Resonant Column and Cyclic Triaxial Tests*. Journal of the Franklin Institute, 348(7), 1363-1376.

Kim D.S., Stokoe K.H. 1995. *Deformational Characteristics of Soils at Small to Medium Strains*. Earthquake Geotechnical Engineering, Tokyo.

Kisiel I. 1967. *Reologia w budownictwie*. Arkady, Warszawa.

Kong L., Sayem H.M., Tian H. 2018. *Influence of Drying – Wetting Cycles on Soil-Water Characteristic Curve of Undisturbed Granite Residual Soils and Microstructure Mechanism by Nuclear Magnetic Resonance (NMR) Spin-Spin Relaxation Time (T2) Relaxometry*. Canadian Geotechnical Journal, 55(2), 208-216.

Król M. 2013. *Problemy związane z posadowieniem elektrowni wiatrowych*. Geoinżynieria. Drogi Mosty Tunele, 44(3), 44-46.

Kuang K.S.C. 2018. *Wireless Chemiluminescence – Based Sensor for Soil Deformation Detection*, Sensors and Actuators, 269, 70-78.

Lade P.V. 1977. *Elasto-Plastic Stress-Strain Theory for Cohesionless Soil with Curved Yield Surfaces*. International Journal of Solids and Structures, 13(11), 1019-1035.

Lipiński M.J. 2000. G_{max} *as an Indicator of Undrained Response of Sand to Cyclic Loading*. Annals of Warsaw Agricultural University, Land Reclamation, 29, 31-40.

Lipiński M.J. 2012. *Wybrane kryteria określania parametrów gruntów naturalnych*. Inżynieria Morska i Geotechnika, 4, 267–277.

Lipiński M.J., Wdowska M.K. 2015. *Capability and Limitations in Laboratory Determination of Stiffness Parameters of Soils*. Annals of Warsaw University of Life Sciences – SGGW Land Reclamation, 47(2), 139-151.

Look B.G. 2007. *Handbook of Geotechnical Investigation and Design Tables*. Taylor & Francis, London.

Lombardi D., Bhattacharya S., Muir Wood D. 2013. *Dynamic Soil–Structure Interaction of Monopile Supported Wind Turbines in Cohesive Soil*. Soil Dynynamic Earthquake Engineering, 49, 165-180.

Lowe D.G. 1999. *Object Recognition from Local Scale-Invariant Features*. Proceedings of IEEE International Conference on Computer Vision (ICCV), Kerkyra.

Lucas B., Kanade T. 1988. *An Iterative Image Restoration Technique with an Application to Stereo Vision*. Proceedings of the DARPA IU Workshop, 121-130.

Madhusudhan B.N., Senetakis K. 2016. *Evaluating Use of Resonant Column in Flexural Mode for Ddynamic Characterization of Bangalore Sand*. Soils and Foundations, 56(3), 574-580.

Mair R.J. 1993. *Developments in Geotechnical Engineering Research: Applications to Tunnels and Deep Excavations*. Proceedings of the Institution of Civil Engineers – Civil Engineering, 3, 27-41.

Massarsch K.R. 2004. *Deformation Properties of Fine-Grained Soils from Seismic Tests.* Proc. of International Conference on Site Characterization, ICS'2, Porto, Portugal, 19-22.

Mayne P.W., Coop M.R., Springman S.M., Huang A-B., Zornberg J.G. 2009. *Geomaterial Behavior and Testing*. Proceedings of 17th International Conference on Soil Mechanics and Geotechnical Engineering, Alexandria, Egypt, 5-9 October 2009, p. 2777-2872.

Nelder J.A., Mead R. 1965. *A Simplex Method for Function Minimization*. Computer Journal, 7(4), 308-313.

Ni S.H. 1987. *Dynamic Properties of Sand under True Triaxial Test States from Resonant Column/Torsional Shear Test*. PhD thesis. The University of Texas, Austin.

Niemunis A., Cudny M. 2000. *O teorii sprężystości w modelowaniu gruntów spoistych*. Proceedings of "Geotechnika w Budownictwie i Inżynierii Środowiska", Politechnika Gdańska, p. 49-60.

Nogami Y., Murono Y., Morikawa H. 2012. *Nonlinear Hysteresis Model Taking into Account S-Shaped Hysteresis Loop and Its Standard Parameters*. Proceedings of the 15th World Conference on Earthquake Engineering, Lisboa, Portugal.

Ohta N. 1989. *Optical Flow Detection by Color Images*. Proceedings of IEEE International Conference on Image Processing, 801-805.

Potts D.M., Zdravkovič L. 1999. *Finite Element Analysis in Geotechnical Engineering. Theory*. Thomas Telford, London.

Puzrin A.M. 2012. *Constitutive Modelling in Geomechanics*. Springer, Berlin.

Puzrin A.M., Burland J.B. 1998. *Non-Linear Model of Small-Strain Behaviour of Soils*. Geotechnique, 48(2), 217-233.

Sawangsuriya A. 2012. *Wave Propagation Methods for Determining Stiffness of Geomaterials*. Wave Processes in Classical and New Solids, InTech.

Schanz T. 1998. *Zur Modellierung des mechanischen Verhaltens von Reinbungsmateria-lien*. Mitt. Inst. für Geotechnik 45, Universitat Stuttgart.

Senetakis K., Anastasiadis A., Pitilakis K. 2015. *A Comparison of Material Damping Measurements in Resonant Column Using the Steady-State and Free-Vibration Decay Methods*. Soil Dynamics and Earthquake Engineering, 74, 10-13.

Senetakis K., Payan M. 2018. *Small Strain Damping Ratio of Sands and Silty Sands Subjected to Flexural and Torsional Resonant Column Excitation*. Soil Dynamics and Earthquake Engineering, 114, 448-459.

Skels P., Bondars K. 2016. *Applicability of Small Strain Stiffness Parameters for Pile Settlement Calculation*. Procedia Engineering, 172, 999-1006.

Srokosz P.E, Dyka I., Bujko M. 2017. *Badania sztywności gruntu w kolumnie rezonansowej*. Wydawnictwo Uniwersytetu Warmińsko-Mazurskiego, Olsztyn.

Srokosz P.E, Dyka I., Bujko M. 2018a. *Determination of Shear Modulus of Soil in the RC/TS Apparatus for Designing Offshore Wind Power Plant Foundations*. Polish Maritime Research, 25(3), 69-83.

Srokosz P.E., Dyka I., Bujko M. 2018b. *Interpretation of Shear Modulus Degradation Tests*. Studia Geotechnica et Mechanica, 40(2), 125-132.

Srokosz P.E., Bagińska M. 2020. *Application of adaptive neuro-fuzzy inference system for numerical interpretation of soil torsional shear test results*. Advances in Engineering Software, 143, 102793

Srokosz P.E., Bujko M., Bocheńska M., Ossowski R. 2021. *Optical Flow Method for Measuring Deformation of Soil Specimen Subjected to Torsional Shearing*. Measurement, 174.

Scholey G.K., Frost J.D., Lo Presti D.C.F., Jamiolkowski M. 1995. *A Review of Instrumentation for Measuring Small Strains During Triaxial Testing of Soil Specimens*. Geotechnical Testing Journal, 18(2), 137-156.

Shin B. 2018. *Laboratory Investigation of the Stiffness and Damping Properties of Binary and Gap-Graded Mixtures of Granular Soils*. PhD thesis, University of Texas, Austin.

Stokoe K., Parra D., Reyes A., Ayala R., Keene A., Jaffal H., Mohtar C. 2016. *On the Dynamic Properties of Leached Ore and Mine Waste*. Proceedings of Heap Leach Mining Solutions, InfoMine, University of Texas, Austin.

Świdziński W., Mierczyński J. 2010. *Badania reakcji sprężystej gruntów niespoistych za pomocą pomiaru prędkości fali sejsmicznej*. Czasopismo Techniczne, 16(1), 63-82.

Tatsuoka F., Shibuya S., Kuwano R. 2001. *Recent Advances in Stress Strain Testing of Geomaterials in the Laboratory Background and History of TC-29 for 1994-2001*. Advanced Laboratory Stress and Strain Testing of Geomaterials, Swets&Zeitlinger Publishers, Lisse, Netherlands.

Tatsuoka F., Di Benedetto H., Enomoto T., Kawabe S., Kongkitkul W. 2008. *Various Viscosity Types of Geomaterials in Shear and Their Mathematical Expression*. Soils and Foundations, 48(1), 41-60.

Timoshenko S.P., Goodier J.N. 1962. *Theory of Elasticity*. McGraw Hill Book Company, New York-Toronto.

Truty A. 2008. *Sztywność gruntów w zakresie małych odkształceń. Aspekty modelowania numerycznego*. Czasopismo Techniczne, 3, 107-126.

Tyrologou P., Dudeney A.W.L., Grattoni C.A. 2005. *Evolution of Porosity in Geotechnical Composites*. Magnetic Resonance Imaging, 23(6), 765-768.

Uliniarz R. 2017. *Calibration of Selected Small Strain Soil Constitutive Models with Use of Laboratory and In-Situ Tests*. Proceedings of 6th International Workshop, In Situ and Laboratory Characterisation of OC Subsoil, Poznań, p. 110.

Vermeer P.A. 1985. *A Five-Constant Model Unifying Well-Established Concepts*. Proceedings International Workshop on Constitutive Relations for Soils, Balkema, p. 175–197.

Wdowska M.K., Wudzka A. 2006. *Czynniki warunkujące zmienność modułu odkształcenia gruntów spoistych*. Przegląd Naukowy Wydziału Inżynierii i Kształtowania Środowiska SGGW, Rocznik XV, 1(33), 64-74.

White D.J., Take W.A., Bolton M.D. 2003. *Soil Deformation Measurement Using Particle Image Velocimetry (PIV) and Photogrammetry*. Geotechnique, 53(7), 619-631.

Wichtmann T. 2016. *Soil Behaviour Under Cyclic Loading – Experimental Observations, Constitutive Dscription and Applications*. Habilitation thesis. Karlsruhe Institute of Technology, Karlsruhe, Baden-Wuerttemberg, Germany.

Wichtmann T., Kimmig I.M., Triantafyllidis T. 2017. *On Correlations Between "Dynamic" (Small-Sstrain) and "Static" (Large-Strain) Stiffness Moduli – An Experimental Investigation on 19 Sands and Gravels*. Soil Dynamics and Earthquake Engineering, 98, 72-83.

Witowski M. 2021. *Ocena sztywności wybranych gruntów w zakresie małych odkształceń*. PhD thesis, Instytut Techniki Budowlanej, Warszawa.

White D.J., Take W.A., Bolton M.D. 2003. *Soil Deformation Measurement Using Particle Image Velocimetry (PIV) and Photogrammetry*. Geotechnique, 53(7), 619-631.

Xu D.-S. 2017. *A New Measurement Aapproach for Small Deformations of Soil Specimens Using Fiber Bragg Grating Sensors*. Sensors, 17(5), 1016.

Yu L.-Q., Wang L.-Z., Guo Z. 2015. *Long-Term Dynamic Behaviour of Monopole Supported Offshore Wind Turbines in Sand*. Theretical and Applied Mechanics Letters, 5(2), 80-84.

Zaremba A. 2013. *Modyfikacja podłoża gruntowego w świetle posadowienia turbin wiatrowych* (cz. I). Geoinżynieria. Drogi Mosty Tunele, 45(4), 42-48.

STANDARDS AND REGULATIONS

Deutsche Gesellschaft für Geotechnik: Empfehlungen des Arbeitskreises 1.4 Baugrunddynamik der Deutschen Gesellschaft für Geotechnik e.V. 2002. DGGT.

Rozporządzenie Ministra transportu, budownictwa i gospodarki morskiej z dnia 25 kwietnia 2012 r. w sprawie ustalania geotechnicznych warunków posadowienia obiektów budowlanych, Dz.U. z 2012 r., poz. 463.

PN-81/B-03020:1981, Grunty budowlane – Posadowienie bezpośrednie budowli – Obliczenia statyczne i projektowanie.

PN-EN 1997-1, Eurokod 7 – Projektowanie geotechniczne – Część 1: Zasady ogólne.